A NONLINEAR ROTORDYNAMICS MODEL FOR AUTOMOTIVE

TURBOCHARGERS COUPLED TO A PHYSICAL MODEL FOR (SEMI)

FLOATING RING BEARING SYSTEM

A Dissertation

by

WONBAE JUNG

Submitted to the Graduate and Professional School of
Texas A&M University
in partial fulfillment of the requirements for the degree of

DOCTOR OF PHILOSOPHY

Chair of Committee,	Luis San Andrés
Committee Members,	Adolfo Delgado
	Timothy Jacobs
	Chao Ma
Head of Department,	Andreas A. Polycarpou

August 2021

Major Subject: Mechanical Engineering

ABSTRACT[*]

Automotive turbochargers (TCs) rely on engine oil lubricated floating ring bearing systems to produce acceptable performance as per the engine volumetric efficiency, and along with proven reliability. However, these TCs produce rotordynamic responses that are rich in subsynchronous whirl motions through reaching stable limit cycles.

This dissertation describes the integration of a finite length (semi) floating ring bearing (SFRB) model into a rotor and ring structural model for prediction of both the linear and nonlinear rotor responses and their characterization in terms of motion amplitudes and whirl frequencies. The SFRB model includes a thermal energy transport network for the inner and outer radial films and the thrust bearings on each side of the ring. The floating ring show significant thermal gradients along the radial direction due to the large temperature difference, from a *hot* shaft to a *cold* housing, and exacerbated by the heat generated from drag power losses in the inner films adjacent to the rotor. The thermal gradients affect the operating clearances and oil viscosity in each lubricated element, radial and axial.

The time-step numerical integration of the rotor equations of motion accounts for (nonlinear) fluid film bearing forces. The predictive process starts from a static equilibrium position of the TC rotor-bearing system, if existing. Analysis of the transient response of a commercial TC for operation at increasing shaft speeds, from 500 Hz (30

---

[*] Content reproduced with permission from Jung, W., San Andrés, L., 2021, "A Nonlinear Rotordynamics Models for Automotive Turbochargers Coupled to a Physical Model for (Semi) Floating Ring Bearing System," Final Technical Report to KeyYang Precision Co., Ltd., TEES Project 408670 0001.

krpm) to 4,000 Hz (240 krpm), and for particular mass imbalance conditions, shows dominant subsynchronous whirl motions with frequencies ranging from approximately ¼ to ~½ of shaft speed. The analysis also investigates the influence of bearing parameters and rotor mass imbalance distribution on the onset, persistence and severity of subsynchronous rotor whirl motions. From comparisons to one set of measurements, the model produces accurate predictions of the nonlinear behavior hence aiding to identify physical parameters that could delay the onset and severity of multi-frequency whirl motions.

Predictions of linear and nonlinear rotordynamic responses for a commercial TC-SFRB system are obtained with nominal operating parameters: bearing inner film clearance $c_i^* = 7.5$ μm at 20 ºC, inner film length $L_i^* = 4.3$ mm, shaft diameter $D_i^* = 6$ mm, and lubricant viscosity $\mu^* = 6.39$ c-Poise at 120 ºC. The predictions show the rotor subsynchronous motion amplitudes decrease when the SFRB is supplied with a lubricant of large viscosity ($\mu = 1.8 \, \mu^*$), and is constructed to have a small inner film clearance ($c_i = 0.8 \, c_i^*$), a long bearing inner film length ($L_i = 1.3 \, L_i^*$) and a shaft with a thick diameter ($D_i = 1.3 \, D_i^*$). However, the recommended TC-SFRB system will aggravate the TC thermal performance as the modified system demands less lubricant flow and increases the viscous drag power loss and the heat in the film.

Integration of a physically accurate model for the lubricated bearings is required for the TC rotor structural model to reproduce actual measurements and field behavior. The predictive model enables an assessment of the lubricated bearings' system static and dynamic performance as well as both the rotor linear and nonlinear time responses. The

predictive tool can save substantial resources (time and cost) in TC production

development and prototype testing.

DEDICATION

This page is dedicated to my family.

ACKNOWLEDGEMENTS

I thank Dr. Luis San Andrés, committee chair and advisor, for accepting me into the Tribology Group at Texas A&M University Turbomachinery Laboratory. I am truly grateful for his guidance and support, as well as for his prompt response and numerous revisions of my graduate work output (reports and dissertation). Thanks also to my advisory committee members for their support and insight along the way.

I acknowledge KeyYang Precision Company, who is my employer, for their financial support and engineering expertise on this work. Without their advice and encouragement, I could not have gone this far. Special thanks to Mr. Byung-Kee Chung, CEO of KeyYang, for giving me an opportunity of a lifetime, with incomparable support and encouragement throughout the course of this research.

Further, I would like to thank Dr. Brian Murphy for his support and guidance on the rotordynamics software throughout this work.

Thanks to the staff of the Turbomachinery Laboratory for their technical assistance and advice. I also thank my colleagues at the Turbomachinery Laboratory, in particular Dr. Bonjin Koo, Dr. Seunghwa Jeung, Dr. Travis Cable, Dr. Xulieng Lu, Dr. Tingcheng Wu, Dr. Rasool Koosha, Dr. Jing Yang, Scott Tran, Bryan Rodriguez and Andy Alcantara for their encouragement, advice and friendship.

Finally yet importantly, I extend my deepest thanks to my wife, Dr. Hyunkyung Kwon, for her unconditional love and support.

CONTRIBUTORS AND FUNDING SOURCES

Contributors

This work was supervised by a dissertation committee consisting of Dr. Luis San Andrés [advisor], Dr. Adolfo Delgado and Dr. Timothy Jacobs of the Department of Mechanical Engineering, and Dr. Chao Ma of the Department of Engineering Technology and Industrial Distribution.

All other work conducted for the dissertation was completed by the student independently.

NOMENCLATURE

c_i, c_o	Radial clearance for inner and outer films [m]
C_p	Specific heat of ring material [J/(kg K)]
D_C, D_S	Casing inner diameter and shaft outer diameter [m]
e_{JX}, e_{JY}	Journal center eccentricities relative to ring center [m]
e_{lim}	Acceptable balance radius [m]
e_{RX}, e_{RY}	Ring center eccentricities relative to casing center [m]
E_i, E_o	Heat advected by the inner and outer films [W]
H	Heat convection coefficients [W/(m² K)]
h_i, h_o	Film thickness of inner and outer films [m]
f	Natural frequency [Hz]
L_i, L_o	Axial length of inner and outer films [m]
L	Axial length of floating ring [m]
P_A, P_{SUP}	Ambient pressure, lubricant supply pressure [Pa]
Q	Heat flow [W]
R_i, R_o	Inner and outer radii of ring [m]
R_S, R_C	Shaft and bearing casing radii [m]
T_i, T_o, T_{th}	Temperature of inner, outer, and thrust films [ºC]
T_R	Ring temperature [ºC]
T_S, T_C	Temperature of shaft and casing [ºC]
T_{SUP}	Lubricant supply temperature [ºC]
U_{lim}	Total permissible residual unbalance [gram-mm]
$U_{lim,adjusted}$	Adjusted permissible residual unbalance [gram-mm]
W	Static load [N]
α	Thermal expansion coefficient [1/ºC]
ζ	Damping ratio

μ	Lubricant viscosity [Pa.s]
$\rho,\ \kappa$	Lubricant density [kg/m^3] and thermal conductivity [W/m^{o}C]
$\rho_R,\ \kappa_R$	Ring density [kg/m^3], thermal conductivity [W/m^{o}C]
Φ	Mechanical dissipated power/unit area [W/m^2]
$\wp_i, \wp_o$	Total mechanical power converted into heat [W]
Ω	Rotor speed [rad/s]
Ω_R	Ring speed [rad/s]

Abbreviations

CB	Compressor bearing
FWM	Forward whirl mode
MB	Main body
RBS	Rotor bearing system
SFRB	Semi floating ring bearing
TB	Turbine bearing
TC	Turbocharger

TABLE OF CONTENTS

LIST OF FIGURES

xiv

LIST OF TABLES

CHAPTER I

INTRODUCTION

Used in internal combustion engines, automotive turbochargers (TCs) aid to increase engine power and efficiency by recovering the internal energy contained in the exhaust gases. In recent years, the automotive industry increasingly focuses on system downsizing and improved performance while satisfying low emission standards for passenger vehicles (PVs) [1,2]. Among the engine oil lubricated bearing technologies developed by manufactures, semi-floating ring bearing (SFRB) systems offer larger thermal and mechanical efficiencies and proven reliability, while enabling a significant reduction in size with lesser number of parts, weight and cost [3].

The TC comprises a (hot) turbine driving an (air) compressor through a slender shaft supported on a bearing system. Figure 1 shows a cross section of a TC implementing a SFRB system that integrates in a single ring both radial and thrust bearings, engine oil lubricated, to support the spinning rotor with low viscous drag power losses. The non-spinning ring that separates the shaft from the TC center housing makes the films for the radial bearing system: (a) an inner film between the outer surface of the shaft and the inner side of the ring, and (b) an outer film between the outer surface of the ring and the inner side of the housing. The thrust bearings are etched at the ring ends, as shown in Figure 2. Typically a loose pin or button constrains ring rotation; hence, the outer film works as a squeeze film damper. After lubricating the inner film of the radial bearing, the oil flows through the thrust bearing, and then it is ejected to a drain in the casing. Piston rings seal

the shaft and center housing and keep oil from leaking into the compressor and turbine

housings.
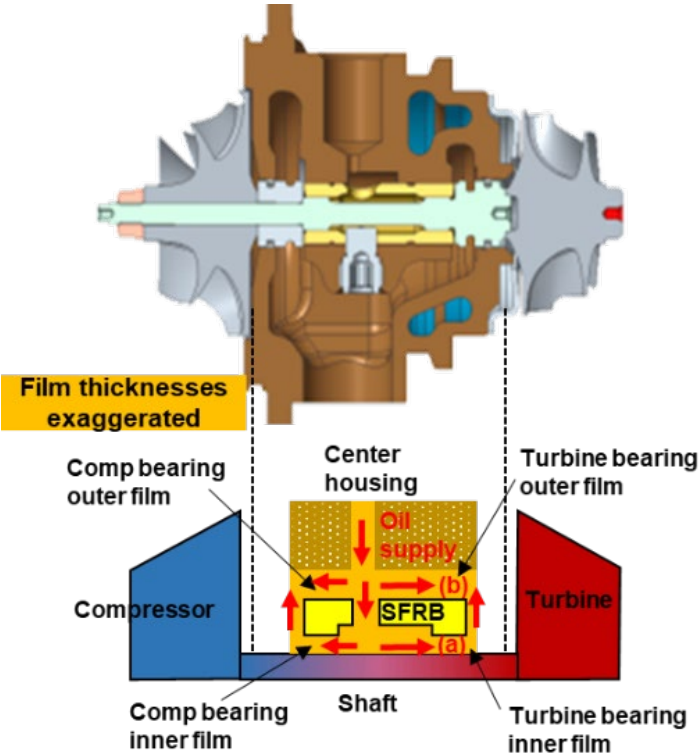
Figure 1. Description of a semi-floating ring bearing system in a TC. Lubricant flow paths shown through both turbine side and compressor side bearings [4].
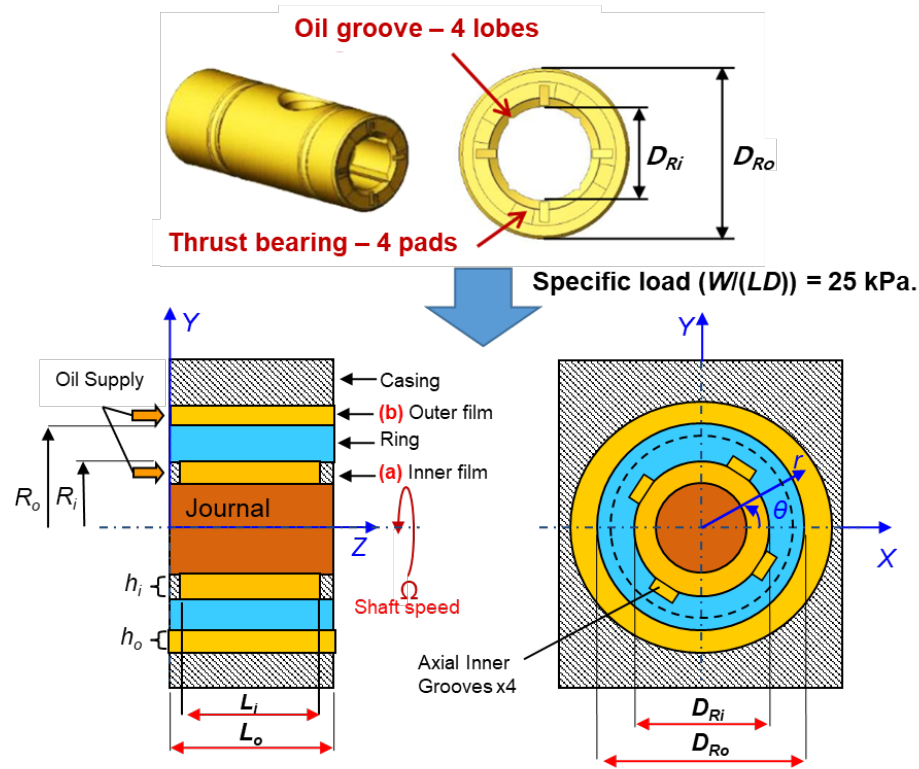
Figure 2. Schematic view of a semi-floating ring bearing in a TC and nomenclature.

Typical oil-lubricated TCs operate at high temperatures, well above ambient, and must withstand large temperature gradients, leading to severe thermo-mechanical stresses. Thus, an insight into the thermal energy flows and an effective thermal management are paramount to ensure reliable TC operation. Past research mainly focuses on evaluation of TCs performance and their matching with engines. There are only handful of efforts for estimation of the thermal energy transport in TCs bearing system, yet most ignore the axial temperature gradient along the ring [6-15].

The main objective of this research is to integrate both radial bearings (turbine and compressor sides) and the thrust bearings to produce a complete thermal analysis predictive tool. The research investigates the effect of thermal energy transport on the

performance of oil lubricated SFRBs for automotive TCs. Lubrication equations and the thermal energy transport equations govern the fluid film flows and temperature fields, inner and outer films, respectively. The finite difference method solves 3-D heat conduction equation for the SFRB. Implementation of the finite element method and the control volume method gives the solution of the Reynolds equations and the thermal energy transport equations, respectively. An efficient algorithm couples the solution of the Reynolds equations and the thermal energy transport equations, and updates the temperature-dependent viscosity and film clearances during the iterative process.

In addition, the rotordynamic force coefficients obtained from the SFRB analysis are coupled to a linear rotordynamics model to perform a linear stability analysis and obtain the damped natural frequencies and mode shapes of the system. Estimated mass imbalances and their distribution are used to calculate the TC rotor synchronous response. Lastly, SFRB operating clearance and lubricant viscosity for the inner and outer films are the main input for predicting bearing forces to conduct a nonlinear time transient response analysis which could yield rotor responses with a rich content in subsynchronous frequencies and amplitudes for specific operating conditions.

Literature review

Background

A TC enables an automotive engine of a specific size to produce more power. One of the most important factors affecting TC performance is the heat transfer between the TC components and also between the TC and ambient. Many researchers and engineers have

made efforts to develop proper (yet simple) heat transfer models to quantify the thermal energy transport. They found simple models based on empirical formulas [4-7], experimental models with heat transfer coefficients obtained from test results [8-11], and advanced conjugate heat transfer models that couple the interaction between the solids and the various fluid flows [12-15]. These models enable engineers to estimate the thermal energy transport flows and balance in TC and to improve the engine simulation tools coupled with the TC model, in particular at low shaft speeds where the total amount of heat transfer from the turbine to the ring is on the same order of magnitude as the turbine extracted mechanical power [5].

Heat transfer flows in automotive turbochargers

Using empirical formulas, Bohn et al. (2003) [6] and Cormerais et al. (2006) [7] verify experimentally the effect of the turbine inlet temperature on a TC compressor performance. Ref. [6] presents experimental results obtained with a turbocharger test bench and evaluating the heat flux between the turbine and the compressor of an automotive TC. The authors perform a parametric study varying the turbine inlet temperature and mass flow rate, to build a relationship with the Reynolds number at the compressor inlet and the heat flux from the turbine to the compressor. The experimental results show that the turbine inlet temperature dominantly influences the total heat flux from turbine to compressor. An increase in mass flow rate leads to a higher pressure ratio in the compressor which increases the temperature of compressor casing. Ref. [7] emphasizes on an influence of the heat transfer on the compressor performance in a

turbocharger. The authors suggest methods to improve the calculation of performance by considering heat transfer. The authors estimate the heat transfer and the isentropic power to define an isentropic efficiency, and obtain the compressor mechanical power and outlet temperature. The last method used considers additional equations, uses the performance map to obtain the isentropic power, the compressor mechanical power and heat transfer. The authors note that the three methods are almost similar though the last one is more easily applicable.

Other researchers use experimentally based methods to obtain correlations for heat transfer coefficients to determine the TC non-adiabatic efficiency and the mechanical power loss. They investigate further the paths of thermal energy flows by performing extensive experiments on ad-hoc test rigs. Baines et at. (2010) [8] present an investigation on the temperature field in a commercial turbocharger installed with thermocouples on all accessible external and internal surfaces. The model for the heat transfer network of the turbocharger is one-dimensional (lumped parameters). The temperature measurements enable to calculate the internal heat flux from the turbine gas to the turbocharger structure and from there to the lubricating oil and to the compressor, and the external heat flux to the environment. The simulation enables to find the heat transfer coefficients required to solve the heat conduction equation. On the compressor side, the internal heat transfer is more than 10 times greater than the external heat transfer for most of conditions with different exhaust inlet temperatures and ventilation rates. On the other hand, on the turbine side, the internal heat transfer is nearly twice the external heat transfer. The turbine external heat transfer is almost four times that in the compressor. The analysis of the heat

transfer in a TC shows the cooling effect of the lubricating oil is important in maintaining an efficient operation of the whole system. Incidentally, Romagnoli et al. (2012) [9] present an investigation on heat transfer in turbochargers operating with engine speeds, from 1000 to 3000 rpm, at steps of 500 rpm, and under an applied load. A 1-D numerical model of the turbocharger is developed and validated against the experimental data. The validation against test data shows that the trend of the heat transferred through the turbine casing is well captured. The test results reveal that the internal combustion engine has a large impact on surface temperature of the turbine and compressor casing, and also that the surface temperatures of both the turbine and the compressor vary linearly with the temperature of the exhaust gases.

Researchers also use various methods to get accurate results for calculating the power loss due to oil shearing effects. Lamquin et al. (2009) [10] investigate both experimentally and analytically the drag power losses of a bearing system in turbocharger. Using the laminar Couette flow assumption, a model calculates the power loss in a radial bearing and integration of the 2-D Reynolds equation delivers the power loss in an axial bearing. The additional power loss between both a slender shaft and the surface of the inner bearing uses a turbulent Couette flow model. The power loss due to the seals is not taken into account. In a steady-state condition, two bearing designs with axial grooves are tested. The influence of oil viscosity on the bearing loss is identified by testing at two oil inlet temperatures (30 °C and 100 °C) and two oil inlet pressures (2 bar and 4 bar). The measurement and prediction of power losses are in good agreement. Later, Deligant et al. (2011) [11] estimate drag power losses in a turbocharger by using a 3D CFD model. The

model calculates various oil inlet temperatures and shaft rotational speeds. The authors note that bearing cooling mostly occurs by conduction throughout the bearing (solid ring) and convection toward the outer clearance. The authors also note that the drag torque is not a linear function of speed, and the slope of drag torque versus speed may decrease with an increase in speed for operation at a low oil temperature (high viscosity).

The conventional methods to calculate the thermal energy flows decouple the fluid mechanics problem from the heat transfer problem between the fluid and the structure. Since the temperature of the bearing structures relies on those of the adjacent fluid films, and the fluid flow mechanics in turn depends on the thermal boundary conditions to the adjacent bearing structures, the fluid films and the bounding solid (ring) influence each other through the thermal boundary interfaces. The conventional method strongly depends on the heat convection transfer coefficients that must be prescribed at the fluid-solid interfaces. In contrast, the Conjugate Heat Transfer (CHT) method takes into account the simultaneous interaction of the heat transfer between the fluid flow and solids. The ability to provide accurate temperature information at any position of the turbine/compressor wheel makes the CHT method the preferred method over a conventional method.

San Andrés et al. (2004) [12] present advancements in both linear and non-linear rotordynamic analyses with a thermal flow analysis to predict the steady state and transient response of an automotive TC supported on FRBs. The model includes a lumped-parameter thermal energy balance to estimate an effective lubricant viscosity and changes in film clearance due to the combined thermal growth of the journal, ring and bearing. The authors compare ring rotational speed, power loss, and shaft motion predictions against

test data measured on a test TC. The results show the predicted ring speed ratio decreases as the shaft speed increases mainly due to a thermal effect affecting the operating film clearances and oil viscosity. Note that the authors assume the lubricant temperature is constant for both the inner and outer flow domains.

San Andrés et al. (2012) [13] extend the earlier lumped-parameter thermal energy transport model to consider a steady-state thermal energy transport in the films, inner and outer, and through the floating ring. The authors conduct an analysis for the prediction of the thermohydrodynamic pressure and temperature fields in a SFRB system for an automotive TC. The predictions reveal that the heat flow from the shaft into the inner film is overwhelming, especially at the inlet lubricant plane where the temperature difference with the inlet cold oil is largest. The inner film temperature increases quickly as soon as the cold lubricant enters the film, due to the large amount of energy generated by shear drag and the heat transfer from the shaft. The results also prove that a floating ring develops a significant radial temperature gradient.

As a result of the development in fast computers and better numerical methods, the CHT method is routinely applied to fluid-solid interaction problems. The physical domain is divided into different blocks for the fluid flow paths and the solid body regions, so that no boundary conditions at the interior walls but at the exterior boundaries are required. Bohn et al. (2005) [14] provide an example of applying the CHT method to investigate the heat transfer in a TC. The authors introduce a CHT analysis model containing the compressor, the oil-lubricated center housing, and the turbine. The authors develop 3D TC energy transfer models with boundary conditions obtained from experiments [6]. The

authors include the thermal boundary condition on the temperature distribution on the surface of the casing and also the boundary conditions for gas at the inlet and outlet of both compressor and turbine. One part of the energy from the exhaust (hot) gas in the turbine becomes the mechanical power that drives the compressor. One other part of the remaining energy, a kinetic energy, leaves as the gas exits the turbine. Another portion leaves the system as heat that equals to the heat loss to ambient and the casing due to natural convection and thermal radiation, as well as the heat taken away by the lubricating oil. Note also that drag power losses in the films also generate heat. The CHT helps the authors to quantify the thermal flows between adjacent regions. The results show that the total heat flux from the turbine to the compressor is mainly influenced by the turbine inlet temperature. Some of the heat entering the compressor does not pass away to the surrounding area, but heats up the compressor gas at some operating points. Unfortunately, the authors ignore that fluid films can also act as a source of power loss while also taking away heat energy flowing from a hot turbine through the shaft.

With the CHT method, Heuer et al. (2006) [15] conduct the analysis on heat transfer for turbine wheels. Ref. [15] presents a feasible optimization method for stress reduction on a turbine wheel of automotive turbocharger. The model shows one part of the wheel surface absorbs heat from the hot gas, while the other part could deliver heat into the gas flowing through the turbine due to the great different temperature levels and the high thermal conductivity of the solid. The heat transfer coefficients obtained at full load serve as a boundary condition for a subsequent transient solid body thermal stress calculation. The authors find the intensification of flow turbulence improves the heat transfer near the

waste gate area. The analysis can determine the location of the potential mechanical fatigue and unmask design deficiencies. However, the authors provide no details on the thermal energy carried away by the lubricant and ignore the fact that the fluid films can also act as a source of mechanical drag power.

Fluid film bearing analyses

Recent research focuses on advancing earlier models by extending the dimension of the analysis for a floating ring and by developing an enhanced lubricant cavitation model. Liang et al. (2017) [16] present an experimental and numerical analysis on the performance of a semi floating ring bearing system in an automotive turbocharger. The rotor and the semi floating ring bearing consider a 3-D thermohydrodynamic model with the thermal viscosity and non-Newtonian effects of lubricant oil. The test results with three different oil supply conditions validates the numerical results. The predicted and experimental results coincide well. The authors note that the heat conduction in the rotor and ring has the same magnitude with the oil film heat flow, and the heat transfer between the two rings is considerable. Thermal expansion of the rotor and ring significantly affects the film clearance especially for the inner film. The authors also note that the distribution of oil film temperature and viscosity along the film thickness are not negligible.

In addition, San Andrés et al. (2018) [17] further extend the earlier model in Ref. [13] to develop the thermal energy transport analysis and predictions for a SFRB system based on the assumption that the ring temperature varies along the radial direction only. The authors develop an updated heat transfer model in a SFRB to consider heat conduction in

both the radial and circumferential directions. The inner film temperature varies around the ring circumference due to the shear drag induced by journal rotation. The ring and casing temperature also show a significant circumferential variation. The heat transfer from the inner film into the ring inner surface occurs in fully wetted (by lubricant) regions. In lubricant cavitation regions play a role of an insulation boundary. The earlier model [13] is not able to predict aforementioned results that also affects the thermal growth of the inner film clearance. However, the advanced model still does not consider the heat flow from thrust bearing side that is not negligible.

Recently, Nitzschke et al. (2018) [18] introduce an advanced liquid cavitation model for a floating ring bearing in an automotive turbocharger. The model adopts the Elrod algorithm, which assumes density and viscosity in the fluid film to be a mixture between the pure fluid and the appropriate gas properties, whereas the latter are negligible. The finite volume method solves the discretized Reynolds equation. The time domain solution uses a common semi-implicit integration scheme. In each time step, the gap function including transient tilting and its time derivative are determined for all fluid films, which serve as input for the solution of pressure distribution. From the resulting pressure distributions, the bearing forces and moments are calculated, which are then applied to shaft and floating rings.

Other researchers perform further parametric studies with various TC operation conditions. Sandoval et al. (2018) [19] present a correlation of injection temperatures and lubricating oil pressure of an automotive TC to shaft vibration amplitude. The test bearing is a SFRB with a shaft diameter of 16 mm. The TC is accelerated to 80 krpm and three

different supply pressures, 3, 3.5 and 4 bar, and oil inlet temperatures, 70, 80, and 90 ºC. The test results show the shaft synchronous amplitudes decrease with an increase in the SFRB TC oil working temperature. The test results also show that the supply pressure variations do not provoke considerably different result.

Zhang et al. (2019) [20] present experimental and numerical investigations on the performance of a full floating ring bearing system with operating parameters representative of an automotive turbocharger. The full floating ring bearing has a circumferential oil groove on its outer surface to increase flow rate. The numerical model solves the thermal energy balance and the Reynolds equation to analyze temperature distribution, mechanical power loss, and ring speed ratio for various oil supply conditions. The authors conduct an extensive experimentation on a cold gas turbocharger test bench to validate the numerical model. The results show that oil supply conditions render different degrees of influence on the operating parameters of the test bearings. An increase in supply pressure increases flow rate both along the inner and outer film regions and thus reduces their temperatures. On the other hand, the drag power loss increases due to an increase in average oil viscosity. An increase in oil inlet temperature yields a dramatic decrease in power loss both at low and high shaft speeds, which indicates that high oil supply temperature improves the efficiency of a TC. The predicted heat flow demonstrates the convective heat flow (lubricant carries heat away) in the inner film is limited and most of the heat is conducted through the floating ring into the outer film. Thus, a proper selection of ring material and its thickness is required to ensure an adequate heat flow path to maintain system integrity.

For a TC application, it is important to manage appropriately the heat flow from the thrust bearing as it is not negligible. Yu et al. (2002) [21] investigate thermal effects on the performance of a thrust bearing with radial grooves. The analysis model solves the Reynolds equation and a thermal energy balance equation for the lubricant pressure and temperature fields. The model also solves the temperature of the thrust bearing with the heat conduction equation assuming the physical domain of the solids is uniform. The results show that thermal effects do not only reduce the load carrying capacity of the thrust bearing and the drag torque but also increase the flow rate significantly due to the reduction in lubricant viscosity. The numerical model also predicts that the thermal effect has greater influence on the load support when the groove depth or the number of groove increases.

Lee et al. (2018) [22] present an investigation on the axial thrust load for an automotive TC. The authors first measure deformation of a thrust bearing along the axial direction and its temperature during TC operation. Then the authors subtract the deformation due to the thermal effect from the measured one, to obtain the thrust load in a model with desired operating conditions. The predictions based on a finite element analysis show a good agreement with the test data. The authors note that the bearing must be designed carefully to withstand the thrust load and to balance the axial movement of the rotor, as the axial thrust load affects the friction loss that reduces the performance of the turbocharger.

Recently, Peixoto et al. (2021) [23] present a thermo-hydrodynamic bearing model for a TC supported on FRBs to predict nonlinear rotordynamic shaft motions considering both radial and axial vibrations during rotor speed run up/down (20 krpm ~ 140 krpm). The

model includes the thermal energy transport in the oil films and produces temperature increases for both radial and thrust bearings. The thrust bearing model considers the heat conduction and heat convection along the radial, circumferential, and axial directions, whereas the radial bearing energy transport model simplifies to a lumped parameter thermal model. Both the radial bearings and the thrust bearings nonlinear reaction forces are coupled to the equations of motion for the TC rotor. The authors perform numerical predictions and obtain measurements that show rotor synchronous motion amplitude along the axial direction due to excitations from the compressor outlet airflow. The authors note that their predictions agree well with the measurements, in particular for operation at a high rotor speed (~140 krpm).

Summarizing past research, Table 1 lists the publications most relevant to the present work. The literature reviewed on heat transfer flows with a (S)FRB system in automotive TCs includes Bohn and Heuer [6,14,15], Romagnoli et al. [9], San Andrés et al. [12,13,17], Liang et al. [16], Zhang et al. [20], and Peixoto et al. [23]. The last column includes the features of the current work which focuses on advancing a model for prediction of a SFRB considering heat flow from the thrust bearing.

Table 1. Relevant past literature on heat transfer flows in a (S)FRB system for automotive TCs.

	Bohn and Heuer [6,14,15] 2003~2006	Romagnoli et al. [9] 2012	San Andrés et al. [12,13,17] 2004~2018	Liang et al. [16] 2017	Zhang et al. [20] 2019	Peixoto et al. [23] 2021	Current research
Application	Automotive TC						
Analysis	Experimental and numerical						
Bearing type	FRB	FRB	FRB, SFRB	SFRB	FRB	FRB	SFRB
Heat transfer model	Empirical formula, CHT	Experimental based	Empirical formula, CHT	Empirical formula, CHT	Empirical formula	Empirical formula, CHT	Empirical formula, CHT
Ring model	1-D (Radial)	1-D (Radial)	1-D (Radial), 2-D (Radial, circumferential)	3-D (Radial, circumferential and axial)	1-D (Radial)	3-D (Radial, circumferential and axial)	3-D (Radial, circumferential and axial)
Heat from thrust bearing	Not considered	Not considered	Not considered	Not considered	Not considered	Considered	Considered
Focus on	CB, TB	CB, TB	TB	CB, TB	CB, TB	CB, TB	CB, TB
Bearing material	Brass	Brass	Brass	Brass	Brass	-	Brass
D (mm)	-	-	7.92	7	-	8	6.01±2
L/D	-	0.26~0.53	0.77	0.57~0.74	0.83	0.55	0.70
Radial clearance (μm)	-	-	7.5	12	22	8.75~12.75	7.5±1.5
Load $W/(LD)$ (kPa)	-	-	25	18	-	-	36
Speed (krpm)	-	90~170	30~240	10~180	35~75	20~140	30~240

Turbocharger rotordynamics

Nguyen-Schäfer (2012) [24] introduces linear and nonlinear rotordynamics of automotive TCs. The author shows the dynamic response of rotating machines at very high rotor speeds, and procedures to balance a TC rotor, and the thermodynamics and turbo matching to compute operating conditions of TCs. In addition, the author further details structural dynamics to compute the bearing reaction loads at various operating conditions, and to design the hydrodynamic oil film bearings.

An assessment for a TC rotordynamic performance requires concerted tests, both costly and time consuming. A proven predictive model thus will enable significant savings in cost and development. Nearly a decade ago, San Andrés et al. [12, 25-28] (2003-2012) already developed advanced predictive models. Holt et al. (2005) [25] introduce a complete nonlinear rotordynamics model and conduct comprehensive measurements of casing acceleration with a high speed TC unit supported on FRBs. The experiments show the effects of increasing lubricant inlet pressure and temperature on the TC complex dynamic response for shaft speeds to 100 krpm. The nonlinear rotor model incorporating the FRB reaction forces in the numerical integration of the rotor equations of motion predicts the limit cycle amplitudes with two fundamental subsynchronous whirl frequencies. The predictions, validated by test data, evidence two subsynchronous vibration whirl motions at approximately one-half ring speed and one-half ring speed plus one-half journal speed. The transient nonlinear responses reveal the importance of rotor imbalance in suppressing subsynchronous whirl motions at high rotor speeds as also observed in the experiments.

San Andrés et al. (2007) [26] present validations against test data for both linear and nonlinear rotordynamic models predicting the dynamic response of TC rotors supported on FRBs. The bearing model considers thermal effects in the flows, thermal expansion of the shaft and bearings, and entrance pressure losses at the oil inlet into the spinning ring due to centrifugal flow effects. The bearing analysis yields linearized rotordynamic force coefficients for the inner and outer lubricant films and is used to predict the rotor synchronous response to imbalance and the system natural frequencies and damping ratios. A nonlinear response model predicts the total shaft motion, and with fast Fourier transforms showing the amplitude of synchronous motion and whirl frequency, and amplitudes of subsynchronous shaft motions for speeds ranging from 10 krpm to 55 krpm (maximum speed 70 krpm), with amplitudes and frequencies that correlate well with the test data.

San Andrés et al. (2010) [27] further extend the earlier work to advance linear and nonlinear rotordynamics models of a SFRB to accurately predict TC rotor nonlinear forced response due to engine-induced center housing excitations. The comparisons of test data against predictions demonstrate that engine vibrations cause a complex low frequency shaft response with significant frequencies at several multiple integers of engine speed. Analysis of measured engine-induced housing accelerations shows that the center housing and compressor housing do not vibrate as a rigid body. The compressor housing deflects nearly twice as much as the center housing. Most importantly, the comparisons of predictions to test data serve to validate this first instance in incorporating engine-induced housing excitations into the rotordynamics model. San Andrés and Vistamehr (2010) [28]

18

also present progress on assessing the effects of oil inlet conditions (pressure and temperature), mass imbalance distribution, and rotor acceleration on the TC rotor-bearing system dynamic forces response. The parametric studies show that a decrease in the oil supply pressure increases the oil inlet temperature, and which brings the whirl frequency jump to occur at a lower threshold rotor speed. Thus, TC operation becomes noisier for operation at high shaft speeds. Operation with the fastest rotor acceleration or deceleration rate produces the strongest hysteresis in TC rotor response. The rotor imbalance distribution greatly affects the location of the threshold of rotor whirl speed and the amplitude of total rotor motion.

Other researchers also focus on quantifying the nonlinear dynamic behavior of TC rotor-bearing system for a high speed application. Gjika and Groves (2006) [29] present a nonlinear dynamic analysis of a TC rotor-bearing system supported on two floating ring bearings. Their numerical model is validated against test data from a TC operating up to 160 krpm. The oil inlet temperature and pressure are 100 °C and 4 bar, respectively. The linear rotordynamics approach is used to obtain the synchronous rotor total motion. The integration of the nonlinear bearing reaction forces enables the time domain prediction of the nonlinear rotor response. The authors note that the subsynchronous motion tends to lower magnitudes at the top speed range of a TC operation, and which can be explained with the increased dynamic loads on the bearings.

Schweizer and Sievert (2009) [30] investigate nonlinear vibrations of an automotive TC supported on FRBs. Frequency spectra of shaft run up speed measurements carried out on a hot gas TC test rig show self-excited vibrations, oil whirl and whip phenomena,

subharmonic and superharmonic motions, and rotor jump phenomenon. The measurement results demonstrate that the system exhibits four main frequencies; the first one is synchronous vibration due to rotor imbalance; the second one is generated by the oil whirl and whip of the inner film which excite a subsynchronous speed conical forward mode; the third one is also due to the oil whirl and whip of the inner film which excite a subsynchronous speed bouncing forward mode; and the fourth one is generated by the oil whirl and whip of the outer film which excite a subsynchronous speed conical forward mode. The authors note that a decrease in the oil supply pressure causes the subsynchronous vibration generated by the oil whirl and whip in the outer fluid films. In addition, an increase in the oil supply temperature (lower viscosity) causes the subsynchronous vibration due to oil whirl and whip in the outer films.

Koutsovasilis et al. (2015) [31] introduce a numerical approach to quantify the subsynchronous vibrations of FRB systems in an automotive turbocharger during shaft run-up speed simulations. The input parameters are the geometries of both rotor and bearings. Linear multivariate regression algorithms and data mining techniques, i.e., correlation coefficients and global sensitivity methods, enable to analyze and quantify the influence of each design parameter on the sub-synchronous formation. The numerical results show the shaft diameter is the most influential design variable for controlling total rotor response. Other parameters include the center of mass distance between the compressor wheel and the compressor side bearing, the distance between the center of masses of the two bearings, and the center of mass distance between the turbine wheel and the turbine side bearing.

Liang et al. (2015) [32] present an analysis on the whirl frequency of a TC supported on a SFRB. The model applies the infinitely short and long cylindrical journal bearing models to estimate the subsynchronous whirl frequency of a SFRB. The finite element method is used to simulate the 2-D transient response for different types of SFRBs. Flexible rotors supported on two distinct SFRBs produce the different subsynchronous shaft motions excited. The whirl frequencies predicted by the numerical model show good agreement with the test results.

Recently, researchers highlight the importance of the rotor-bearing system design and their interaction with each component. Cao et al. (2017) [33] present a nonlinear transient model and design for an automotive TC supported on a SFRB system. For a stability analysis, the linear model for the rotor-bearing system evaluates eigenvalues and eigenvectors with the stiffness and damping coefficients of the oil films obtained from the bearing analysis. The linear stability analysis shows that the SFRB improves rotor stability although the system is still linearly unstable. That is, neither a SFRB without a squeeze film damper nor a SFRB with the damper included are able to stabilize the rotor. The nonlinear transient analysis evaluates the rotor and ring limit cycle orbits, rotordynamics, the forces acting on the rotor and semi-floating ring surfaces, the oil flow through the bearing, the oil temperatures, and the power loss of the oil films. The nonlinear transient analysis shows that the bearing undergoes limit cycle motions of approximately 90% of the bearing clearance for the SFRB without the squeeze film damper, and approximately 80% of the clearance of the radial clearance with the damper included. The maximum pad force from the SFRB with the damper included is only 4% of that from the SFRB without

the squeeze film damper, which results in much higher bearing long term fatigue life. The power loss for the SFRB with the damper included is 73% of the SFRB without the squeeze film damper power loss. However, a higher total oil supply of flow rate is essential for the SFRB as more oil flows out from dampers with larger clearances.

Vengala et al. (2019) [34] present a numerical and experimental evaluation of shaft subsynchronous motion for a SFRB with two different configurations. The numerical model couples multi-body dynamics of the flexible rotor with the housing structures and with the hydrodynamic inner and outer films. The 3-D finite element tool calculates the oil film temperature of the inner and outer films using thermal boundary conditions. The axial length of the bearing for the design A is longer than the one for the design B. As a result, design A has higher inner oil whirl deflection which causes subsynchronous vibration and noise with overall higher shaft deflection, whereas design B shows much lower inner oil whirl deflection and lower overall shaft deflection.

Koutsovasilis (2019) [35] investigate the influence of hydrodynamic thrust bearings on the nonlinear motion and bifurcation of the TC rotor-bearing system in terms of interaction between the thrust and the radial bearings during the TC operation. The analysis focuses on the influence of two major parameters: namely, shaft diameter and thrust bearing position. The influence of the location of the thrust bearing influences on the critical speed which decreases with an increase in the critical frequency up to the first bending, whereas the second bending remains invariant. A slender shaft diameter impacts mostly the natural frequencies at the first and the second bending.

Table 2 summarizes past publications most relevant to the present work. The literature reviewed on TC rotordyanmics supported on a (S)FRB system includes San Andrés et al. [12,25-28], Schweizer et al. [30], Liang et al. [16,32], Koutsovasilis et al. [31,35], and Vengala et al. [34]. The last column features the current work focusing on advancing a model of the rotor-bearing system considering feeding grooves or holes to improve predictions of the TC nonlinear system response to show rotor internal resonances and subsynchronous whirl motions.

Table 2. Relevant past literature on TC rotordynamics supported on a (S)FRB system.

	San Andrés et al. [12,25-28] 2004~2018	Schweizer et al. [30] 2009	Liang et al. [16,32] 2015~2017	Koutsovasilis et al. [31,35] 2015~2019	Vengala et al. [34] 2019	Current research
Application	Automotive TC					
Analysis	Experimental and numerical					
Bearing type	FRB, SFRB	FRB	SFRB	FRB	SFRB	SFRB
Oil type	ISO VG 10, SAE 5W-30	-	SAE 15W-40	-	-	SAE 10W-30
Rotor-bearing model	3-D FEM	3-D FEM	3-D FEM	3-D FEM	3-D FEM	3-D FEM
D (mm)	7.92~11.5	6	7~8	6~6.8	-	6.015
L/D	0.70~0.77	0.6	0.57~0.74	0.53~0.60	0.30~0.48	0.72
P_{SUP} (bar)	1.3~2.7	1.5~3.0	0.5~4.0	-	-	1.8~2.7
T_{SUP} (°C)	26.7~126.1	75~90	50~90	90~150	-	95~120
Speed (krpm)	30~240	0~160	10~180	0~300	100~320	30~240
Bearing performance	Included	Not included	Included	Not included	Included	Included
Linear eigenvalue analysis	Included	Included	Included	Included	Not included	Included
Imbalance synchronous response	Included	Not included	Included	Not included	Not included	Included
Nonlinear rotordynamic response	Included	Included	Included	Included	Included	Included

Statement of work

The current work contemplates integrating a predictive bearing tool [4] into a rotordynamics structure model to produce system dynamic responses from both linear and non-linear bearing models. TC rotors supported on engine oil lubricated bearings produce time-varying responses that are rich in subsynchronous whirl motions, i.e. having one or more subsynchronous frequencies and with large amplitudes of rotor motion at the turbine and compressor ends that could touch (rub) against their housings [25,28]. The nonlinearity arises from the hydrodynamic character of the fluid film bearings supporting the rotor, the flexible nature of the slim rotor and heavy end inertias (turbine and compressor), and the exceedingly large operating speeds of the rotating shaft, many times above the lowest (rigid body) natural frequencies of the rotor-bearing system. TC rotors reach a limit cycle that permits their operation over long times. A linear rotordynamics model can neither predict the amplitude(s) of rotor limit cycle motions nor their frequency content [25,26].

CHAPTER II

A THERMOHYDRODYNAMIC MODEL FOR A SEMI-FLOATING RING

BEARING SYSTEM[*]

Figure 3 depicts a schematic view of a semi-floating ring bearing system comprised of a journal spinning with speed Ω_S, a stationary floating ring ($\Omega_R = 0$), and a bearing casing. The drawing is not to scale. The model divides the ring into three sections, namely the turbine bearing (TB) side, the main body (MB), and the compressor bearing (CB) side. Lubricant supplied with pressure (P_{SUP}) and temperature (T_{SUP}) flows through a supply hole ($z = 0$) into outer film regions with film thickness $h_{TB,o}$ and $h_{CB,o}$ on the TB and the CB sides. A fraction of the lubricant flows axially towards the bearing discharge plane ($z = L_{TB,th}$,-$L_{CB,th}$) with outer film pressure $P_{TB,o}$ and $P_{CB,o}$, and temperature $T_{TB,o}$ and $T_{CB,o}$ in the TB and the CB regions. Another portion of the cold lubricant flows through holes in the ring into the inner film regions with film thickness $h_{TB,i}$ and $h_{CB,i}$ on the TB and the CB sides and generates hydrodynamic pressure fields $P_{TB,i}$ and $P_{CB,i}$ with temperatures $T_{TB,i}$ and $T_{CB,i}$. The lubricant streams at the TB and CB discharge planes ($z = L_{TB,th}$,-$L_{CB,th}$) leave the inner film regions taking away energy flowing from the *hot* shaft and the mechanical power induced by shear drag. A fraction of heat is conducted into the ring which also convects heat flow

---

into the outer film. Remaining fractions of heat flow into the bearing casing and towards the CB side by conduction.

After lubricating the inner film of the radial bearing, the oil enters the thrust bearings at the TB and the CB sides, each with film thickness $h_{TB,th}$ and $h_{CB,th}$, respectively. The film pressure is $P_{TB,th}$ and $P_{CB,th}$ at the thrust bearings, and the temperature is $T_{TB,th}$ and $T_{CB,th}$, respectively. Most of the fluid flow is radially outwards and ejected into a main drain in the casing. Note there is mixing of flow on the inner side of the thrust bearing and an exit side of the inner film, for example.
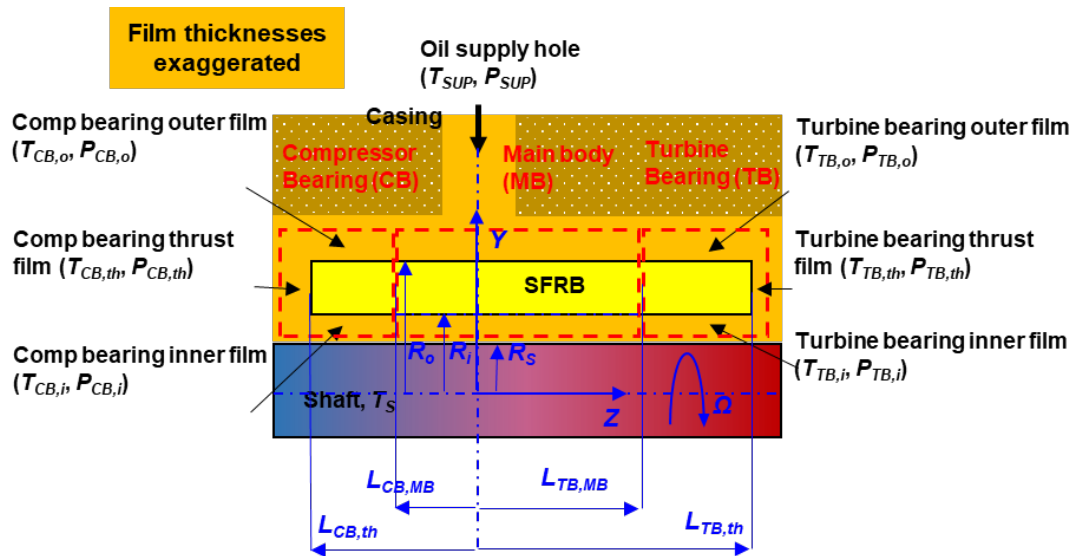
Figure 3. Schematic view of a semi-floating ring bearing system in a turbocharger. Geometry and coordinate systems.

Global form of the heat transport equation in the flow domains

Figure 4 depicts a schematic view of the heat flows and mechanical drag powers in the films of a SFRB system. The flow path through both films must be designed carefully to

ensure the lubricant flow rates cool effectively the bearing components without actually increasing the viscous drag power loss that influences adversely a TC mechanical efficiency. The figure shows the heat flows (Q) across the various components and the heat (E) advected or carried by the lubricant. In general, $Q = (H \text{ x } \Delta T \text{ x Area})$ where H is a heat convection coefficient and ΔT is a temperature difference. Note $\wp$ is a mechanical drag power from fluid flow shear.

Integration of the energy transport equations in the circumferential and axial directions leads to global balances of energy in the inner and outer flow domains, respectively.

Figure 4. Schematic view of heat flows in a SFRB system of a TC.

28

Balance of heat flows in the inner films

Figure 5 shows a schematic view of the transport of energy in the inner film at the TB and CB sections[1]. Other heat flows are not included in the figure for simplicity.
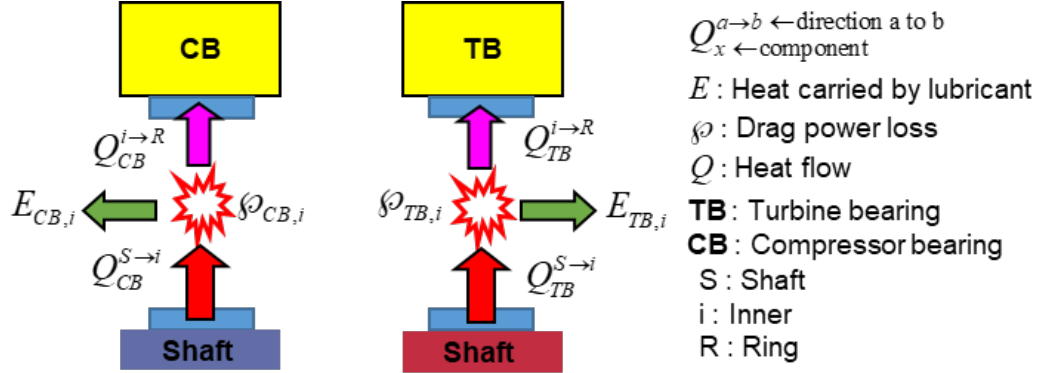
Figure 5. Schematic views of the heat flows in the inner films at the TB and CB sections of a TC SFRB system. See Fig. 4 for the whole SFRB system.

Note that the sum of the heat advected by the inner film and the heat flowing from the inner film into the ring inner surface equals to the sum of the mechanical drag power converted into heat to the inner film and the heat flow from the shaft into the inner film, i.e., $(E_i + Q^{i \to R} = \wp_i + Q^{S \to i})_{TB,CB}$.

The heat convected by either the inner film at the TB or at the CB sections equals

$$E_i = \int_{L_{MB}}^{L_{th}} \int_0^{2\pi} C_v \left[\frac{1}{R_S} \frac{\partial}{\partial \theta} \left(\dot{m}_{\theta_i} T_i \right) + \frac{\partial}{\partial z} \left(\dot{m}_{z_i} T_i \right) \right] R_S \, d\theta \, dz \tag{1}$$

---

[1] Throughout the analysis, sub-indices *i, o, and th* denote the inner and outer films, and thrust films, respectively.

where the first integral term $\int_0^{2\pi} \frac{1}{R_S} \frac{\partial}{\partial \theta}\left(\dot{m}_{\theta_i} T_i\right) d\theta = 0$ because of periodicity, i.e.,

$\left(\dot{m}_{\theta,z}, T\right)_\theta = \left(\dot{m}_{\theta,z}, T\right)_{\theta+2\pi}$.

Above $\left(\dot{m}_{\theta_i}, \dot{m}_{z_i}\right)$ denote the lubricant mass flow rates in the inner film along the circumferential and axial directions,

$$\dot{m}_{\theta_i} = \left(\rho U h\right)_i = -\frac{\rho h_i^3}{12\mu_i} \frac{\partial P_i}{R_S \partial \theta} + \left(\rho h\right)_i U_m \tag{2a}$$

$$\dot{m}_{z_i} = \left(\rho W h\right)_i = -\frac{\rho h_i^3}{12\mu_i} \frac{\partial P_i}{\partial z} \tag{2b}$$

The mechanical drag powers converted into heat at the inner films of the TB and CB sections equal

$$\wp_i = \int_{L_{MB}}^{L_{th}} \int_0^{2\pi} \Phi_i R_S d\theta dz \tag{3}$$

where Φ_i is the shear mechanical energy dissipation function in the inner film.

$$\Phi_i = 12 \frac{\mu_i}{h_i}\left[W_i^2 + \frac{1}{12}\left(U_S - U_R\right)^2 + \left(U_i - U_m\right)^2\right] \tag{4}$$

with $U_S = R_S \Omega_S$, $U_R = R_i \Omega_R$, $U_m = \frac{1}{2}\left(U_S + U_R\right)$. From Eqn. (2), the mean flow velocities in the circumferential and axial direction are,

$$U_i = -\frac{h_i^2}{12\mu_i} \frac{\partial P_i}{R_S \partial \theta} + U_m, \quad W_i = -\frac{h_i^2}{12\mu_i} \frac{\partial P_i}{\partial z_i} \tag{5}$$

30

The heat flows from the inner films into the ring inner surface at the TB and CB sections equal [13]

$$Q^{i \to R} = \int_{L_{MB}}^{L_{th}} \int_0^{2\pi} \left[H_i (T_i - T_{R_i}) \right] R_i d\theta dz \tag{6}$$

where H_i is the heat convection coefficient for the inner film bounding the ring, and

$T_{R_i} = T_{(r=R_i, \theta, z)}$ is the temperature of the ID surface of the ring.

Likewise, the heat flow from the shaft into the inner film at the TB and CB sections is

$$Q^{S \to i} = \int_{L_{MB}}^{L_{th}} \int_0^{2\pi} \left[H_i (T_S - T_i) \right] R_i d\theta dz = -Q^{i \to S} \tag{7}$$

Above T_S is the temperature of the shaft surface.

Balance of heat flows in the outer films

Figure 6 shows a schematic view of the energy transport in the outer film at the TB and CB sections. Note several heat flows are not shown in the figure for simplicity.

Note that the sum of the heat convected by the outer film and the heat flowing from the outer film into the bearing casing equals to the sum of the mechanical drag power converted into heat to the outer film plus the heat flow from the ring outer surface into the outer film, i.e., $(E_o + Q^{o \to C} = \wp_o + Q^{R \to o})_{TB,CB}$.
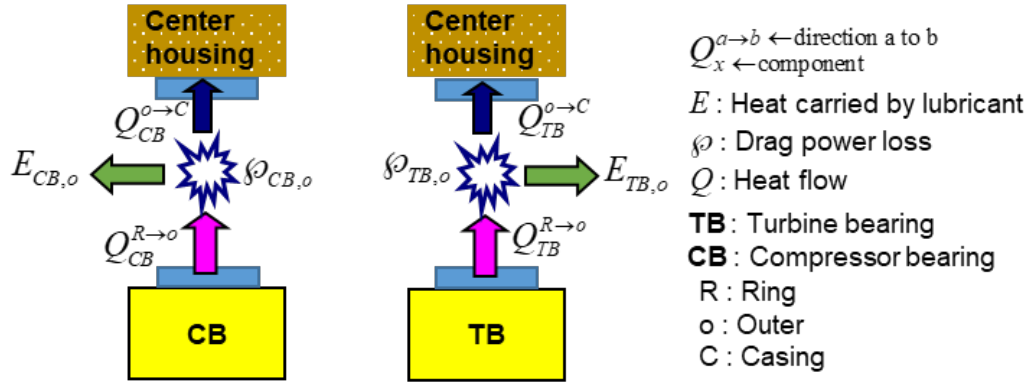
Figure 6. Schematic views of the heat flows in the outer films at the TB and CB sections of a TC SFRB system. See Fig. 4 for the whole SFRB system.

The heat convected by the outer film at the TB and CB sections is

$$E_o = \int_{L_{MB}}^{L_{th}} \int_0^{2\pi} C_v \left[\frac{\partial}{\partial z} \left(\dot{m}_{z_o} T_o \right) \right] R_o d\theta dz \tag{8}$$

where $\dot{m}_{z_o}$ is the lubricant mass flow rate in the outer film along the axial direction (z).

$$\dot{m}_{z_o} = \left(\rho W h \right)_o = -\frac{\rho h_o^3}{12 \mu_o} \frac{\partial P_o}{\partial z} \tag{9}$$

The mechanical drag powers converted into heat at the outer films of the TB and CB sections is

$$\wp_o = \int_{L_{MB}}^{L_{th}} \int_0^{2\pi} \Phi_o R_o d\theta dz \tag{10}$$

where Φ_o is the shear energy dissipation function in the outer film,

$$\Phi_o = 12 \frac{\mu_o}{h_o} \left[\left(\frac{h_o^2}{12 \mu_o} \frac{\partial P_o}{R_o \partial \theta} \right)^2 + \left(\frac{h_o^2}{12 \mu_o} \frac{\partial P_o}{\partial z_o} \right)^2 \right] \tag{11}$$

32

Incidentally, in a SFRB the ring does not rotate ($\Omega_R = 0$); thus in the outer film there is no shear flow induced power converted into heat.

The heat flows from the ring outer surface into the outer film at the TB or the CB sections are

$$Q^{R \to o} = \int_{L_{MB}}^{L_{th}} \int_0^{2\pi} \left[H_o (T_{R_o} - T_o) \right] R_o d\theta dz \tag{12}$$

where H_o is the heat convection coefficient for the outer film bounding the ring, and with $T_{R_o} = T_{(r=R_o, \theta, z)}$ as the temperature of the OD surface of the ring.

The heat flows from the outer film into the TC casing at the TB or the CB sections equal

$$Q^{o \to C} = \int_{L_{MB}}^{L_{th}} \int_0^{2\pi} \left[H_o (T_o - T_C) \right] R_o d\theta dz = -Q^{C \to o} \tag{13}$$

Balance of heat flows in the thrust bearings

Figure 7 shows a schematic view of the energy flows in the film of the thrust bearing at the TB and CB sections.

Note that the sum of the heat advected by the thrust film and the heat flowing from the thrust film into the ring equals to the sum of the mechanical drag power in the thrust film converted and the heat flow from the shaft (thrust collar) into the thrust film, i.e.,

$(E_{th} + Q^{th \to R} = \wp_{th} + Q^{S \to th})_{TB,CB}$.
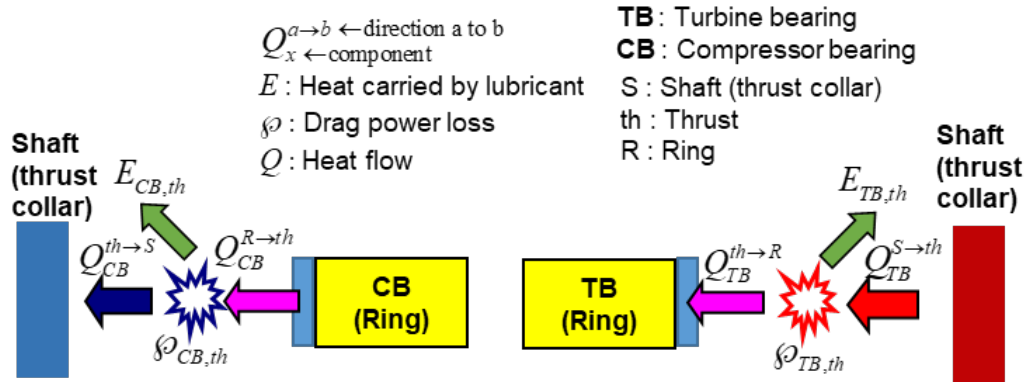
Figure 7. Schematic views of the heat transport in the thrust bearings at the TB and CB sections of a TC SFRB system. See Fig. 4 for the whole SFRB system.

The heat flows convected by the thrust films at the TB or the CB sections equal

$$E_{th} = \int_0^{2\pi} \int_{R_i}^{R_o} C_v \left[\frac{1}{r} \frac{\partial}{\partial r} \left(r \dot{m}_r T_{th} \right) \right] r dr d\theta \tag{14}$$

where $\dot{m}_r$ is the lubricant mass flow rate in the thrust film along the radial direction, T_{th} is the temperature of the film in the thrust bearing. In the current analysis, the lubricant temperature is assumed not to vary across the thrust film thickness (z-direction).

For the thrust films at the TB and CB sections, the mechanical drag powers converted into heat are

$$\wp_{th} = \int_0^{2\pi} \int_{R_i}^{R_o} \left(\frac{h_{th} \Omega}{2} \frac{\partial P_{th}}{\partial \theta} + \frac{\mu_{th}}{h_{th}} \left(r\Omega \right)^2 \right) r \, dr d\theta \tag{15}$$

The heat flowing from the thrust film into the ring surface is

$$Q^{th \to R} = \int_0^{2\pi} \int_{R_i}^{R_o} \left[H_{th} (T_{th} - T_{R_{th}}) \right] r dr d\theta \tag{16}$$

where $T_{R_{th}} = T_{(r,\theta,z=L_{th})}$ is the ring surface temperature at the thrust bearing, and H_{th} is a heat convection coefficient.

Likewise, the heat flow from the shaft (thrust collar) into the thrust film is

$$Q^{S \to th} = \int_0^{2\pi} \int_{R_i}^{R_o} \left[H_{th}(T_S - T_{th}) \right] r\, dr\, d\theta \tag{17}$$

where T_S is the temperature on the shaft (thrust collar) surface.

Heat flows balance and temperature field in a (semi) floating ring

Figure 8 shows a schematic view of the heat flows in the ring. For convenience, the graph shows the ring divided into three sections: the TB, the MB (main body), and the CB.
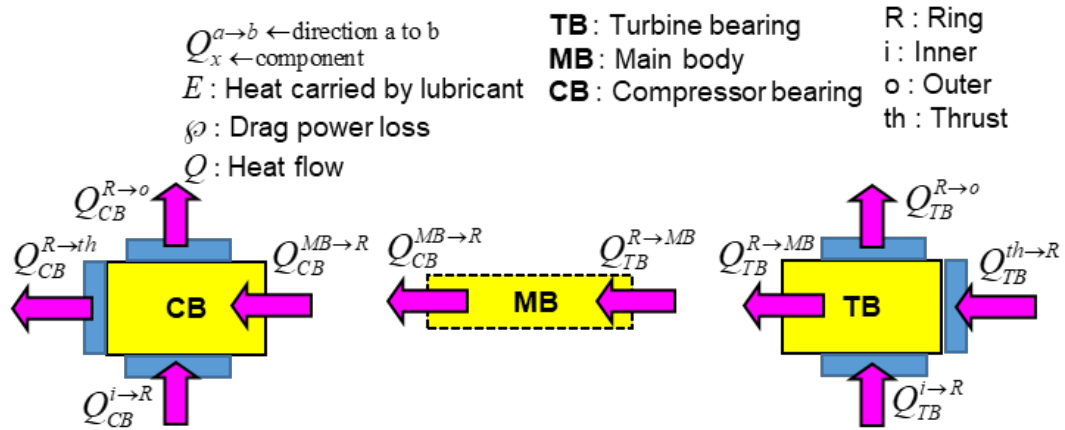
Figure 8. Schematic views of the heat transport in a floating ring: main body and sections with bearings on the turbine and compressor sides. See Fig. 4 for the whole SFRB system.

A solution of the energy transport equations for the inner and outer films produces the heat flows (Q's). Since there is no accumulation of heat in the ring, the sum of heat flows from the inner film and thrust film into the ring must equal the sum of the heat flows from the ring into the outer film and into the main body, $(Q^{i \to R} + Q^{th \to R} = Q^{R \to o} + Q^{R \to MB})_{TB,CB}$.

The heat flow from the inner film into the ring inner surface at the TB or the CB sections equals [13]

$$Q^{i \to R} = \int_{L_{MB}}^{L_{th}} \int_0^{2\pi} \left[H_i(T_i - T_{R_i}) \right] R_i d\theta dz \tag{18}$$

The heat flow from the ring outer surface into the outer film at the TB or the CB sections is

$$Q^{R \to o} = \int_{L_{MB}}^{L_{th}} \int_0^{2\pi} \left[H_o(T_{R_o} - T_o) \right] R_o d\theta dz \tag{19}$$

The heat flow from the thrust film into the ring surface at the bearing end is

$$Q^{th \to R} = \int_0^{2\pi} \int_{R_i}^{R_o} \left[H_{th}(T_{th} - T_{R_{th}}) \right] r dr d\theta = -Q^{R \to th} \tag{20}$$

The heat flow from the ring surface into the main body at boundary surface is

$$Q^{R \to MB} = \int_0^{2\pi} \int_{R_i}^{R_o} \left[H_{MB}(T_{R_{MB}} - T_{MB}) \right] r dr d\theta = -Q^{MB \to R} \tag{21}$$

Since there is no accumulation of heat in the main body, the heat flow from the ring surface into the main body at the TB section must equal to the heat from the main body into the ring at the CB section, $Q_{TB}^{R \to MB} = Q_{CB}^{MB \to R}$, please see Fig. 8.

Above the heat convection coefficients (H_i, H_o, H_s) depend on the local Prandtl number $Pr = C_v \mu / \kappa$ and the Reynolds number $Re = \rho U h / \mu$ which determines the flow condition, laminar or turbulent. Refs. [36,37] provide a variety of heat convection coefficients, including those for fully developed and developing wall temperatures.

Heat conduction equation for floating ring

The steady-state heat conduction equation for a semi-floating ring in the cylindrical coordinate system (r, θ, z) is

$$\vec{\nabla} \cdot \left(\kappa_R \vec{\nabla} T_R \right) = 0 \tag{22}$$

in the domain $\left\{ R_i \leq r \leq R_o, 0 \leq \theta \leq 2\pi, -L_{CB,th} \leq z \leq L_{TB,th} \right\}$. Above κ_R is the thermal conductivity coefficient of the ring (homogeneous) material.

Note that early work conducted by San Andrés et al. [17] for simplicity ignored the heat conduction along the axial direction ($q_z=0$). The current analysis remedies the early shortcoming.

San Andrés et al. [17] details the boundary conditions for the heat flow on the inner and outer surfaces of the floating ring. The boundary conditions on the bearing end sides of the ring ($z = L_{TB,th}, L_{CB,th}$), i.e. the thrust bearings, and on the boundary surface between the bearing and the main body ($z = L_{TB,MB}, L_{CB,MB}$) over the region ($r \in \{R_i, R_o\}$, $\theta \in \{0, 2\pi\}$) are:

$$\left[H_{th}(T_{th} - T_{R_{th}}) = q_z \big|_{r,\theta,z=L_{th}} = -\kappa_R \frac{\partial T_{R_{th}}}{\partial z} \bigg|_{r,\theta,z=L_{th}} \right]_{TB,CB} \tag{23}$$

$$\left[H_{MB}(T_{R_{MB}} - T_{MB}) = q_z \big|_{r,\theta,z=L_{MB}} = -\kappa_R \frac{\partial T_{R_{MB}}}{\partial z} \bigg|_{r,\theta,z=L_{MB}} \right]_{TB,CB} \tag{24}$$

where T_{th} is the temperature of the film of the thrust bearing, and $T_{R_{th}} = T_{(r,\theta,z=L_{th})}$ is the surface temperature of the thrust bearing at the bearing end, respectively. $T_{R_{MB}} = T_{(r,\theta,z=L_{MB})}$

is the ring surface temperature on the boundary between the bearing and the main body, and T_{MB} is the main body temperature on the bearing side, respectively. H_{th} and H_{MB} are the heat convection coefficients on the axial side of the hollow floating ring, respectively.

Note that the heat flow in Eq. (23) includes heat from the thrust bearing and T_{th} is neither constant nor uniform. $T_{th}=T_{inlet}+\Delta T_{th}$, where T_{inlet} is the temperature at the inlet of a thrust pad and obtained from the temperature of the fluid leaving the inner film, and ΔT_{th} is the film temperature rise in one thrust pad.

T_{MB} largely depends on T_{SUP} as the oil supplied flows through the ID and OD of the ring main body with a negligible amount of heat convection and drag power loss.

Equations for generation of hydrodynamic pressure in the thin film flow domains

In operation, the inner film thickness h_i and the outer film thickness h_o are [12,13,17]

$$h_i = c_i(\theta, z_i, T_i) - e_{Sx}\cos\theta - e_{Sy}\sin\theta \tag{25.a}$$

$$h_o = c_o(\theta, z_o, T_o) - e_{Rx}\cos\theta - e_{Ry}\sin\theta \tag{25.b}$$

where c_i and c_o are the inner and outer film clearances, a function of the film temperature and the thermal expansion material properties of the ring, shaft and casing. Above e_S is the shaft eccentricity relative to the ring center, and e_R is the eccentricity of the ring center with respect to the bearing.

In a thin fluid film region, the Reynolds equation determines the generation of hydrodynamic pressure (P) under laminar flow[2] and for a steady-state condition [38]. For the inner and outer films of the radial bearings at the TB or the CB sections, the steady-state equations are:

$$\frac{1}{R_S^2}\frac{\partial}{\partial\theta}\left(\frac{h_i^3}{12\mu_i}\frac{\partial P_i}{\partial\theta}\right)+\frac{\partial}{\partial z_i}\left(\frac{h_i^3}{12\mu_i}\frac{\partial P_i}{\partial z_i}\right)=\frac{\Omega_S}{2}\frac{\partial h_i}{\partial\theta} \qquad (26.a)$$

$$\frac{1}{R_{R_o}^2}\frac{\partial}{\partial\theta}\left(\frac{h_o^3}{12\mu_o}\frac{\partial P_o}{\partial\theta}\right)+\frac{\partial}{\partial z_o}\left(\frac{h_o^3}{12\mu_o}\frac{\partial P_o}{\partial z_o}\right)=0 \qquad (26.b)$$

where (P_i, T_i, h_i) and (P_o, T_o, h_o) denote the pressure, the temperature and the film thickness of the inner and outer films, respectively; and Ω_S is the shaft angular speed. Above μ denotes the oil viscosity, a non-linear physical parameter determined by the local temperature and the shear rate, see Ref. [39].

Figure 9 shows a schematic view of a single thrust bearing pad at the end of the TB or the CB sides and facing a SFRB. The analysis assumes that all pads (total of four) on the thrust bearing are identical. The cylindrical coordinate system (r, θ, z) describes the bearing geometry. The thrust collar and shaft spinning with angular speed (Ω) can only displace axially, thus the analysis neglects rotor tilt. $D_{Ri}(=2R_i)$ and $D_{Ro}(=2R_o)$ are the bearing inner and outer diameters, respectively. The pad film thickness (h_{th}) varies circumferentially in the tapered portion of the pad and remains constant in the flat portion.

---

[2] For most TC oil lubricated bearings, $Re = \rho\Omega R/\mu < 1,500$, thus both fluid inertia and turbulent flow effects are negligible.
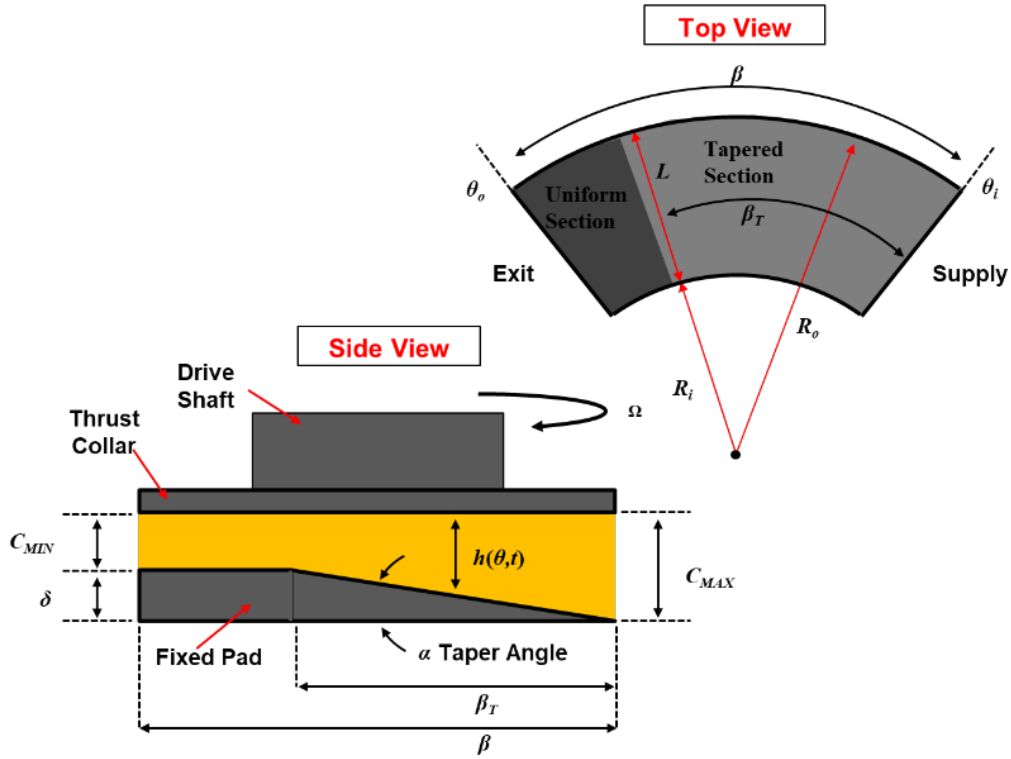
Figure 9. Schematic view of single thrust bearing pad with notation [40].

The flat land, designed to operate at a minimum film clearance (C_{MIN}), prevents unnecessary wear to the bearing and thrust collar during start and stop. C_{MIN} is determined by the thrust load which increases with an increase in shaft speed due to the imbalance between the turbine and compressor axial loads. In the figure, β is the pad arc length, and β_T denotes the tapered arc length, respectively. β_T/β is the fraction of taper in a bearing pad, and α denotes the circumferential taper (inclination) angle. With $R_m (= \frac{R_i + R_o}{2})$ as a mean radius of the thrust bearing pad, $\delta = \alpha R_m \beta_T$ is a maximum taper height, and the pad film thickness $h_{th} = C_{MIN} + \alpha R_m (\beta_T - \theta)$ for $0 \le \theta \le \beta_T$, while $h_{th} = C_{MIN}$ for $\beta_T < \theta \le \beta$.

The Reynolds equation for a thin fluid film in the thrust bearing on the TB or CB sides produces the generation of pressure under steady-state conditions.

$$\frac{1}{r}\frac{\partial}{\partial r}\left(r\frac{h_{th}^{3}}{12\mu_{th}}\frac{\partial P_{th}}{\partial r}\right)+\frac{1}{r}\frac{\partial}{\partial\theta}\left(\frac{h_{th}^{3}}{12\mu_{th}}\frac{\partial P_{th}}{r\,\partial\theta}\right)=\frac{\Omega}{2}\frac{\partial h_{th}}{\partial\theta} \tag{27}$$

where (P_{th}, T_{th}, h_{th}) denote the pressure, temperature, and thickness on a thrust bearing pad, respectively.

Numerical solution procedure

The finite difference method solves 3-D heat conduction equation for the SFRB. Implementation of the finite element method and the control volume method gives the solution of the Reynolds equations and the energy transport (heat flow) equations, respectively. An efficient algorithm couples the solution of the Reynolds equations and the heat transport equations, and updates the temperature-dependent viscosity and film clearances during the iterative process. The entire process, conducted in a regular PC, takes a few seconds to complete for each case (speed or load varying).

CHAPTER III

PREDICTIONS OF HEAT FLOWS IN A TURBINE SFRB[*]

For an example SFRB used in an automotive TC, Table 1 lists the dimensions, lubricant and materials properties, and operating conditions. SAE 10W30 mineral oil at P_{SUP}=3.0 bar and T_{SUP}=120 ºC supplies the SFRB at its inlet plane (z =0). The ring has four equally spaced axial grooves on its inner surface at the compressor bearing (CB) and the turbine bearing (TB) locations.

Note there is a large radial thermal gradient across the floating bearing since the shaft is quite hot ($T_{S,turbine}$ =213 ºC, $T_{S,compressor}$ =195 ºC) while the TC casing is maintained at a temperature T_C =T_{SUP} =120 ºC. The shaft temperature at each bearing location follows from an <u>empirical </u>relation established by San Andrés et al. [17]: (T_S-T_{SUP}) = $\underline{\theta}$ ($T_{turbine}$-T_{SUP}), where $T_{turbine}$ = 700 ºC and the defect temperature ratio $\underline{\theta}$ = 0.16 for $T_{S,turbine}$; while $\underline{\theta}$ = 0.13 for $T_{S,compressor}$. Note the specified ($T_{S,turbine}$ - $T_{S,compressor}$)= 18 ºC temperature gradient along the axial direction is assumed only. In addition, the lubricant flash point temperature T_{flash} ≈ 230ºC, while the actual compressor wheel temperature $T_{compressor}$ = 200~300 ºC.

---

[*] Portion reprinted with permission from San Andrés, L., Jung, W., and Hong, S.K., 2021, "A Thermo-Hydrodynamic Model for Thermal Energy Flow Management in a (Semi) Floating Ring Bearing System for Automotive Turbochargers," ASME J. Eng. Gas Turbines Power, **143**(1), p. 011013.

Table 1. Geometry and operating condition of a SFRB for a TC.

RBS geometry			
Shaft OD, D_s	6 mm		
Ring ID, D_{Ri}	6.015 mm		
Ring OD, D_{Ro}	10.920 mm		
Casing ID, D_c	11 mm		
Inner film axial length, L_i	4.3 mm (Turb.), 4.4 mm (Comp.)		
Outer film axial length, L_o	7.0 mm (Turb.), 5.0 mm (Comp.)		
Inner film radial clearance, c_i	7.5 µm (at 20 ºC)		
Outer film radial clearaance, c_o	40 µm (at 20 ºC)		
Material properties (at 20 ºC)	**Shaft**	**Ring**	**Casing**
Material	Steel	Brass	Cast Iron
Conductivity [W/m ºC], κ	43.2	58.1	53.6
Thermal Exp. [1/ ºC], α	1.24×10^{-5}	1.80×10^{-5}	1.25×10^{-5}
Specific heat [J/kg ºC], C_p	519	377	550
Density [kg/m³], ρ	7,833	8,500	7,170
Thrust bearing geometry			
Number of pads, N_{pad}	4		
Pad arc length, β	70 º		
Ratio pad taper, β_T/β	0.78		
Circumferential Taper angle, α	0.57 º [3]		
Taper height, δ	0.40 mm		
One pad area, A_{pad}	12.7 mm²		
Fraction of hot oil carry over[4]	0.8		
Viscosity temperature coefficient	0.03 1/ ºC		
Lubricant SAE 10W30			
Density, ρ	875 kg/m³		
Specific Heat, C_p	1,901 J/kg		
Conductivity, κ	0.12 W/m ºC		
Viscosity at T_{sup}, μ	6.39 c-Poise		
Flash point temperature, T_{flash}	230 ºC		
Operating conditions			
Oil supply pressure, P_{SUP}	3.0 bar		
Oil supply temperature, T_{SUP}	120 ºC		
Casing temperature, T_C	120 ºC		
Shaft temperature, T_S	213 ºC (Turb.), 195 ºC (Comp.)		

The rotor speed ranges from Ω_1= 30 krpm (500 Hz) to Ω_2= 240 krpm (4 kHz)

Radial specific load $(W/(LD))_{TB}$ = 36 kPa and $(W/(LD))_{CB}$ = 2 kPa.

---

[3] Angle of thrust pad in circumferential direction.
[4] Fraction of the hot oil that is carried over from one pad to the next.

Figure 10 shows a prediction of the ring ID and OD temperatures along the ring circumferential and axial directions. The TC shaft spins at 240 krpm (ΩR_i=99.5 m/s). The inner and outer film temperatures have a large influence on the ID and OD ring surface temperatures along the circumferential and axial directions. The maximum temperature of the ring ID surface occurs near the exit plane ($z=L_i$) and just before the next adjacent axial groove. Likewise, the maximum temperature of the ring OD occurs at the exit plane ($z=L_o$). The ring OD temperature is lowest at $\theta \approx 270°$, the location of the ½ moon groove (140° extent) machined on the bearing casing inner surface. Note that there is heat flow from the ring axial sides (thrust bearings) into the ring.

Figure 11 shows the inner film pressure and temperature fields obtained from an example for shaft operation at 240 krpm. The film pressure reaches a minimum at the location of lubricant cavitation inception. The film temperature enters a supply hole at 120ºC, and the shear drag from journal rotation mixes the upstream oil from the adjacent feed hole. The maximum temperature of the inner film occurs near the outlet plane ($z=L_i$) and just before the next axial groove.

Figure 12 shows a prediction of the minimum clearance (C_{MIN}) and the thrust bearing reaction load versus rotor speed. The current analysis considers the load profile in Ref. [10], and which refers to a similar size thrust bearing with OD = 11 mm and four thrust pads. As rotor speed (Ω) increases, C_{MIN} decreases dramatically while the thrust load (W) increases rapidly with an increase in Ω, thus ($W/(A_{pad} \cdot N_{pad}))/ \Omega^2 \sim$ constant.
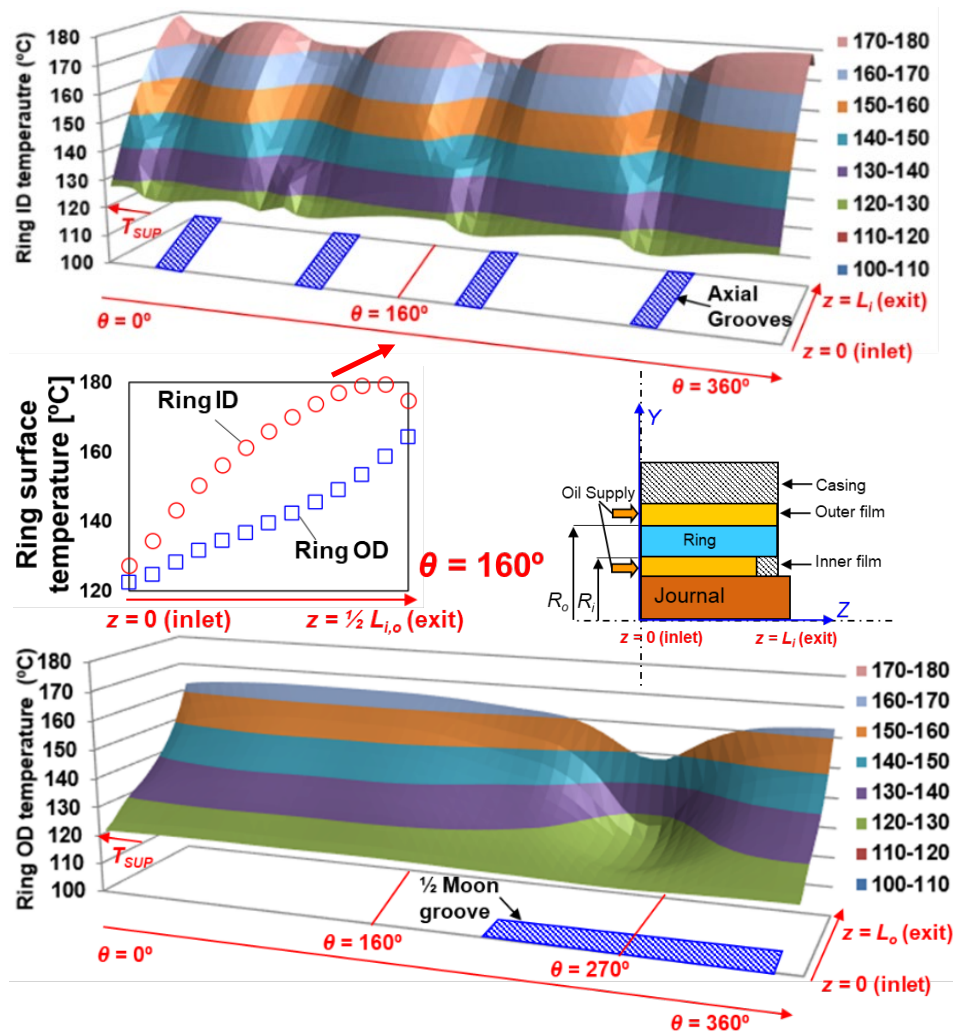
Figure 10. Prediction of ring ID ($r = R_i$) and OD ($r = R_o$) temperatures for an example SFRB along circumferential and axial directions. Rotor speed = 240 krpm. Specific load ($W/(LD)$) = 36 kPa.
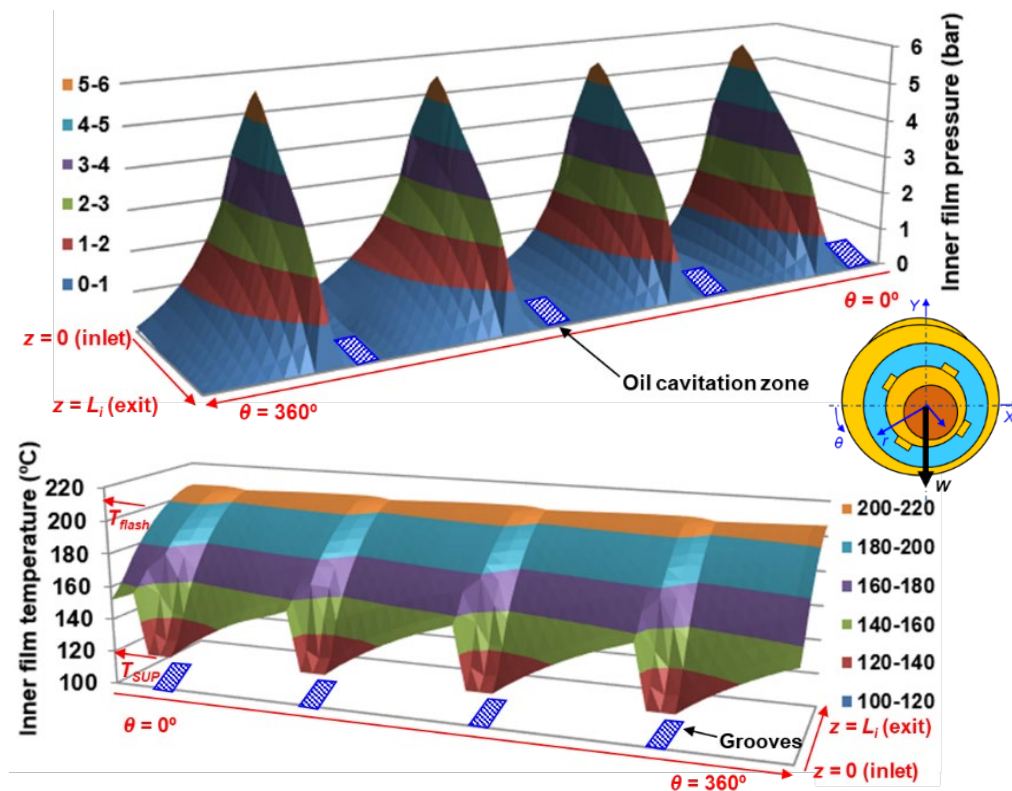
Figure 11. Prediction of pressure and temperature fields in inner film. Shaft speed = 240 krpm. Specific load ($W/(LD)$) = 36 kPa.
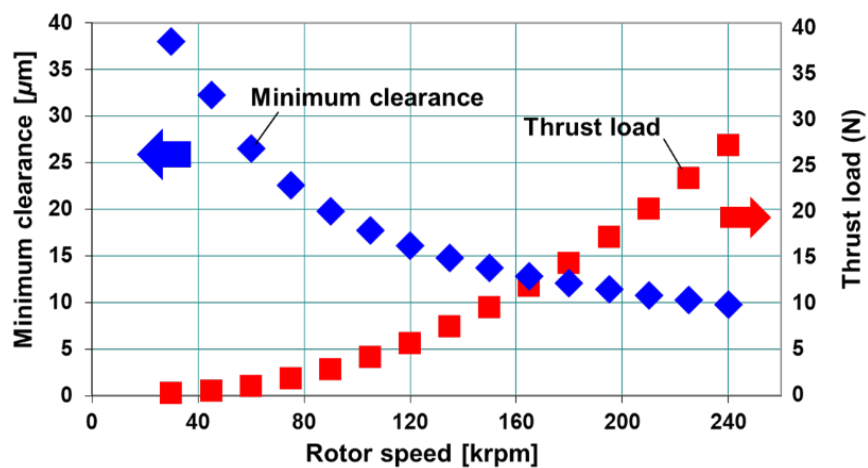
Figure 12. Predicted minimum clearance and specified thrust bearing load [10] versus rotor speed.

Figure 13 shows a prediction of the film pressure field on a thrust pad for shaft operation at 240 krpm ($\Omega R_i = 99.5$ m/s) and with $C_{MIN} = 10$ μm, similar in magnitude to the inner film clearance of the SFRB. The lubricant film pressure reaches a maximum near the end of the tapered section ($\theta = \beta_T = 54.6°$) and at the mid plane along the radial direction. The peak film pressure = 2 MPa ~ four times the applied specific thrust load $W/(A_{pad} \cdot N_{pad})) = 0.5$ MPa.
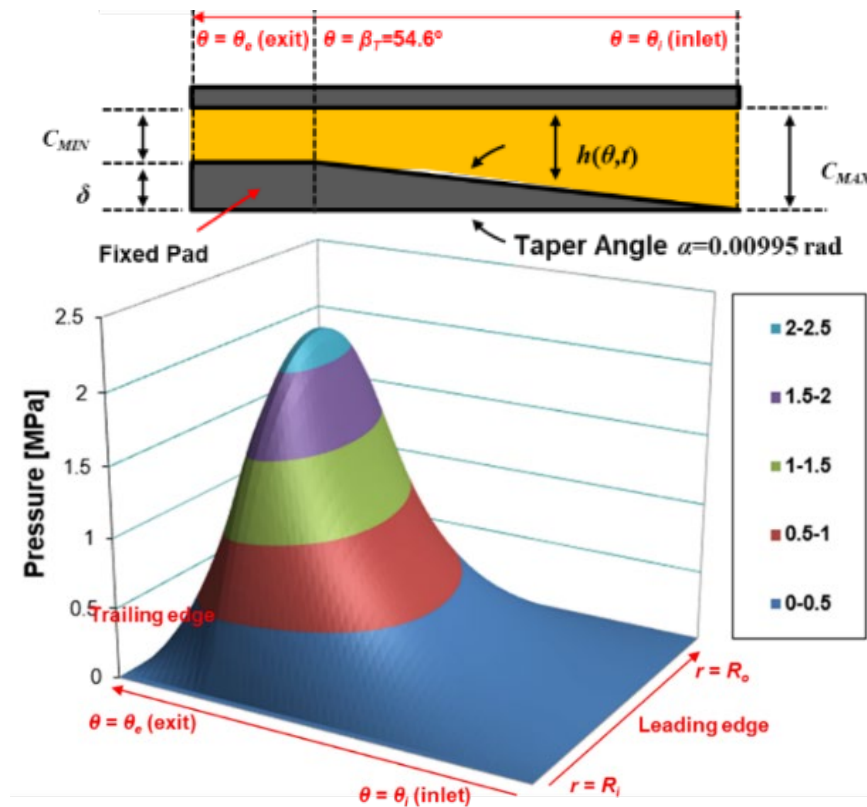
Figure 13. Predicted film pressure field on a pad of thrust bearing (four pads). Specific load ($W/(A_{pad} \cdot N_{pad})) = 0.5$ MPa at shaft speed = 240 krpm and $C_{MIN} = 10$ μm.

Figure 14 shows the predicted drag power loss for the thrust bearing and the temperature rise in the film of one thrust pad (ΔT_{th}) versus rotor speed. As shaft speed increases, the lubricant heats rapidly with an increase in drag power loss ($\wp$), thus $\wp/\Omega^2 \sim$ constant. Recall that $T_{th} = T_{inlet} + \Delta T_{th}$, with T_{inlet} follows from the lubricant temperature leaving the inner film and $\Delta T_{th} \sim \Omega$ as the power loss increases with shaft speed.
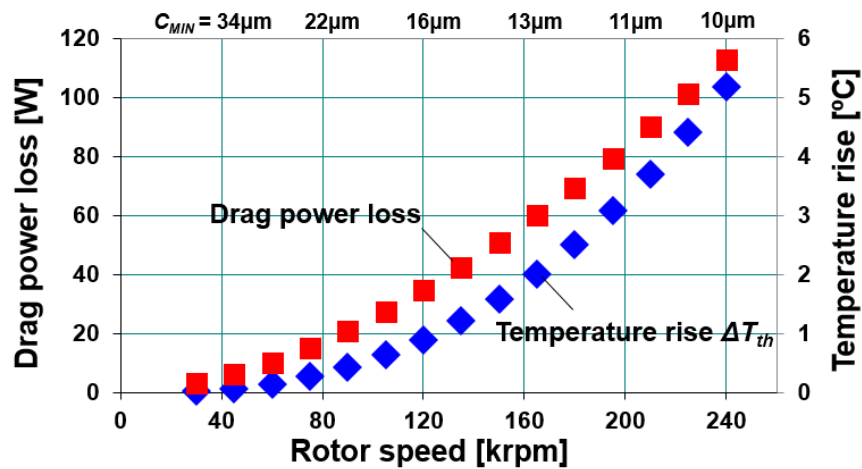
Figure 14. Predicted drag power loss for thrust bearing (turbine side) and temperature rise ΔT_{th} in film of one thrust pad versus rotor speed.

For the CB and the TB, Figure 15 shows a prediction of the average inner and outer film temperatures and the average ring ID and OD surface temperatures, versus rotor speed. The average temperature is a mean value obtained around the bearing circumference and along the axial direction. For both bearings, the outer film heats a few degrees above the supply temperature of 120 °C, whereas the inner film average temperature heats in proportion to an increase in surface speed ($\Omega R_i = 99.5$ m/s). The ring ID surface temperature is ~20 °C higher than the ring OD surface temperature for most operating

speeds. Note the ring temperature varies greatly (> 20 °C), as found from the difference between the maximum temperature and the average temperature, due to the axial heat from the thrust bearing into the ring. Over the entire shaft speed range, the inner and outer film temperatures and the ring ID and OD surface temperatures for the TB are higher than those for the CB since most heat is from the *hot* turbine wheel side ($T_{S,turbine}$ =213 °C), see Figure 4.

As a reference point, note that the lubricant flash point temperature $T_{flash} \approx 230$°C; hence the inner film high temperature remains a constant concern.

(a) Turbine bearing (TB)   **(b) Compressor bearing (CB)**
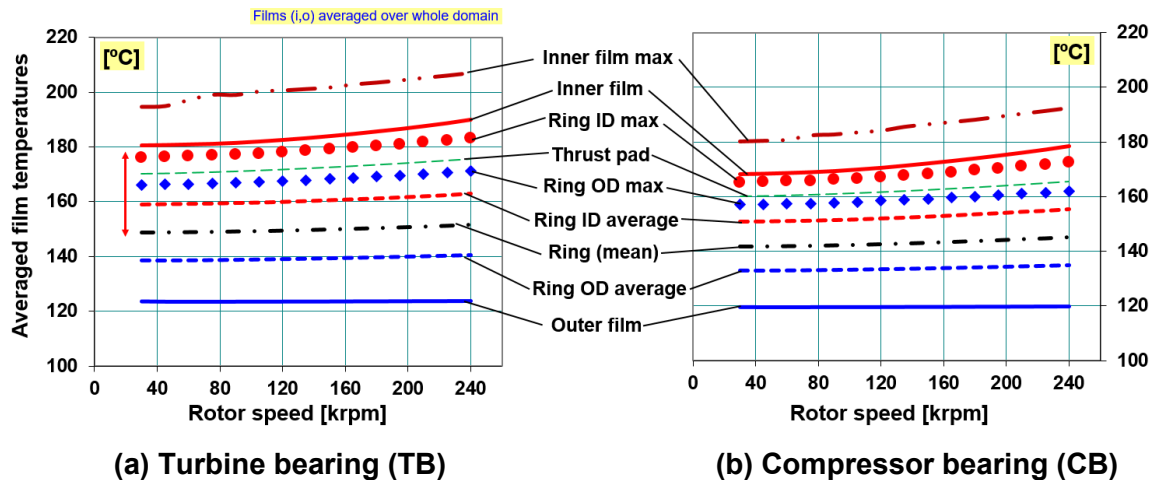
Figure 15. Predicted maximum and average inner and outer film temperatures and ring ID and OD surface temperatures for (a) turbine bearing and (b) compressor bearing versus rotor speed. Radial specific load ($W/(LD)$)$_{TB}$ = 36 kPa and ($W/(LD)$)$_{CB}$ = 2 kPa.

For the CB and the TB, Figure 16 shows the predicted oil exit temperatures leaving the inner and outer films versus rotor speed. Note that the peak temperatures of the inner and outer films occur at the exit plane ($z = L_{i,o}$). For both the CB and the TB, the inner film

temperature is higher than the outer film temperature due to the heat soaking from the shaft and the shear drag effects from shaft rotation. The lubricant exit temperatures are higher at the TB than at the CB due to the heat from the hot turbine wheel.
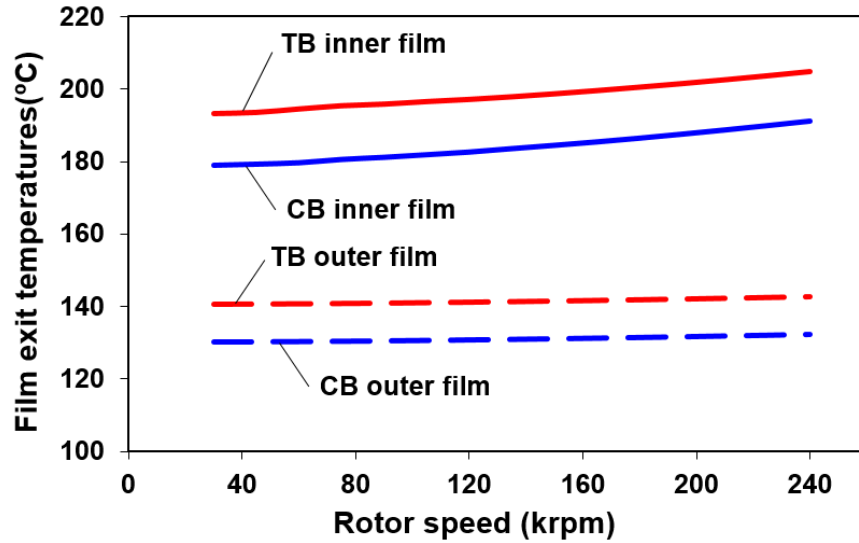
Figure 16. Predicted exit temperature of inner and outer films for compressor bearing (CB) and turbine bearing (TB) versus rotor speed. $T_{S,turbine}$ =213 ⁰C, $T_{S,compressor}$ =195 ⁰C. Radial specific load $(W/(LD))_{TB}$ = 36 kPa and $(W/(LD))_{CB}$ = 2 kPa.

For the CB and the TB, Figure 17 shows the predicted lubricant flow rates through the films versus rotor speed. The flow rate through the outer film is larger than the one through the inner film as the clearance of the outer film, c_o, is larger than that of the inner film, c_i, i.e., c_o/c_i = 5.3 at 20 ⁰C. The flow through the inner film increases as the rotor speed increases since the lubricant viscosity becomes smaller as the film temperature rises and due to lubricant shear thinning from shaft rotation. On the other hand, the flow rate through the outer film is rather constant as the oil temperature does not change dramatically

because the ring does not rotate. The flow rates through the inner and outer films of the

TB are larger than those for the CB because of the higher film temperatures in the TB than

those for the CB and that lead to lower lubricant viscosities. In addition, the flow through

the TB must remove more heat than the flow into the CB.
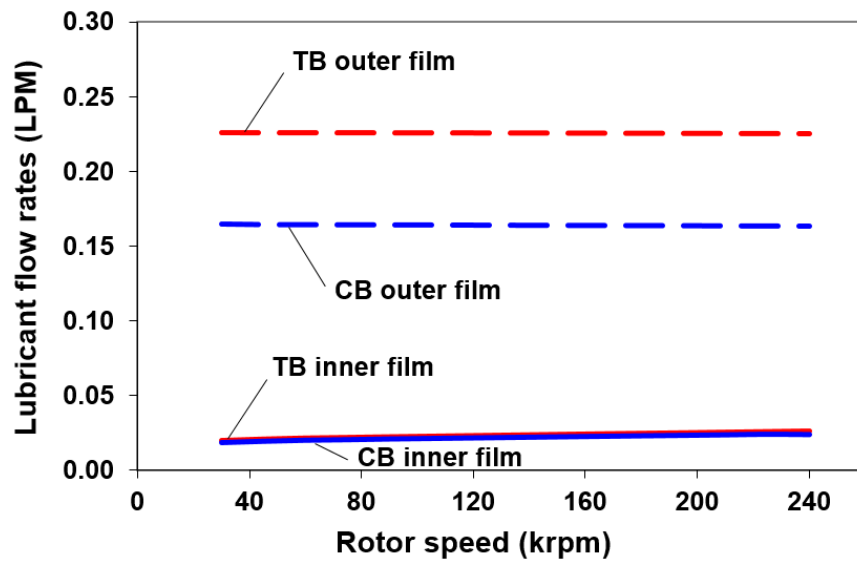
Figure 17. Predicted lubricant flow rates through the inner and outer films for compressor bearing (CB) and turbine bearing (TB) versus rotor speed. Radial specific load ($W/(LD)$)$_{TB}$ = 36 kPa and ($W/(LD)$)$_{CB}$ = 2 kPa.

Figure 18 shows the heat flows and the drag power losses in both the CB and the TB

versus rotor speed. Note the viscous drag power from the inner film and the thrust collar

increase rapidly with shaft speed (power two) while the outer film produces no viscous

power as the ring does not spin. Note the total input energy flow adds the viscous drag

power losses to the heat soaked from the shaft. Important to note that the heat from the

shaft into the inner film and the heat from the thrust collar into the thrust film decrease as

51

shaft speed increases since the films overall temperatures increase. The heat conducted into the ring increases slightly because of the rise in (the inner film) drag power losses, whereas the heat from the outer film into the casing remains relatively constant. Except for the drag power loss and heat flow from the thrust bearings, San Andrés et al. [17] report similar trends on the heat flows as the shaft speed increases.

Note also that the heat from the shaft into the inner film, the heat from the thrust collar into the thrust film, and the heat conducted into the ring are larger on the TB side than those on the CB side as the overall films and the ring temperatures are also higher. For both the CB and the TB, the viscous drag power from the inner film and the thrust collar are almost similar. The heat from the outer film into the casing for the TB is lower than the one on the CB since the outer film temperature is higher in the TB than that in the CB. Recall the casing temperature is constant $T_C = T_{SUP} = 120$ °C.

(a) Turbine bearing (TB)   (b) Compressor bearing (CB)
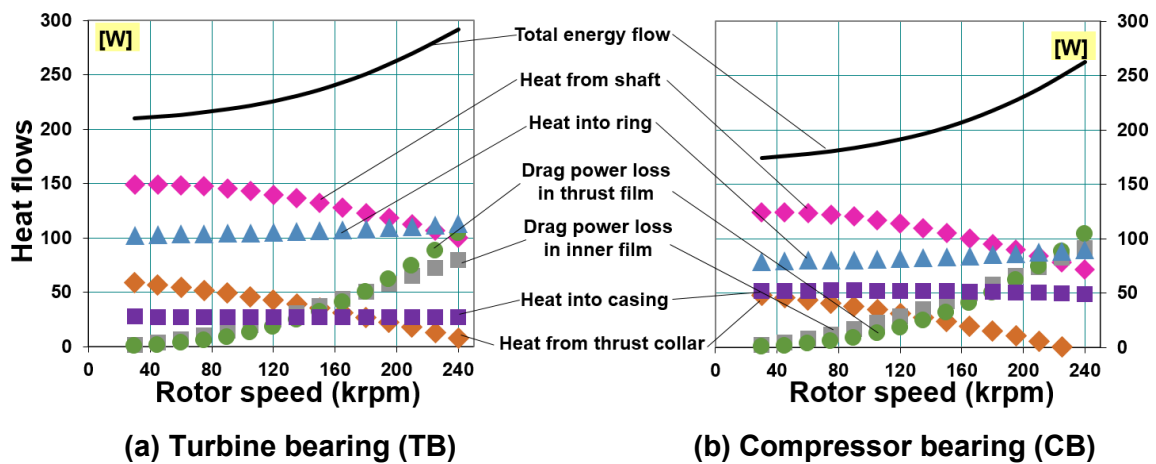
Figure 18. Heat flows and viscous drag power losses in (a) turbine side bearing and in (b) compressor side bearing versus rotor speed. Radial specific load $(W/(LD))_{TB} = 36$ kPa and $(W/(LD))_{CB} = 2$ kPa.

Figure 19 shows schematic representations of the thermal energy flows in the turbine bearing for operation at two shaft speeds, 45 krpm (low) and 240 krpm (high). The representation is similar as the one introduced in Ref. [17]. At the low shaft speed, the heat from the shaft overwhelms the viscous drag power loss, but as the shaft speed increases, the contribution from the drag power to the total energy flow increases significantly from 3% to 63%. The thrust bearing produces 27%-39% of the total energy flow. Note that earlier Ref. [17] does not include the thermal energy flow from the thrust bearing.

The lubricant carries away the majority of the heat flow, from 74% at a low shaft speed to 81% at the highest shaft speed. This indicates the importance of designing a bearing configuration that promotes the flow rates to effectively remove thermal energy flows. Ref. [17] shows larger portion of the total energy flow removed by the lubricant, 90%-98%, as it does not consider both the heat from the thrust bearing and the heat conducted to the compressor bearing. Note that the ring conducts a considerable portion of energy flows from the inner film into the outer film; 49% - 39% of the total energy flow as shaft speed increases, whereas in Ref. [17] the ring conducts less portion of the total energy flow, 23% - 29%, due to omitting the heat flow from the thrust bearing. Note the fractional amount of heat flows conducted into the casing and toward compressor bearing remain nearly invariant with shaft speed. The findings above agree with those in Refs [16,17,41].
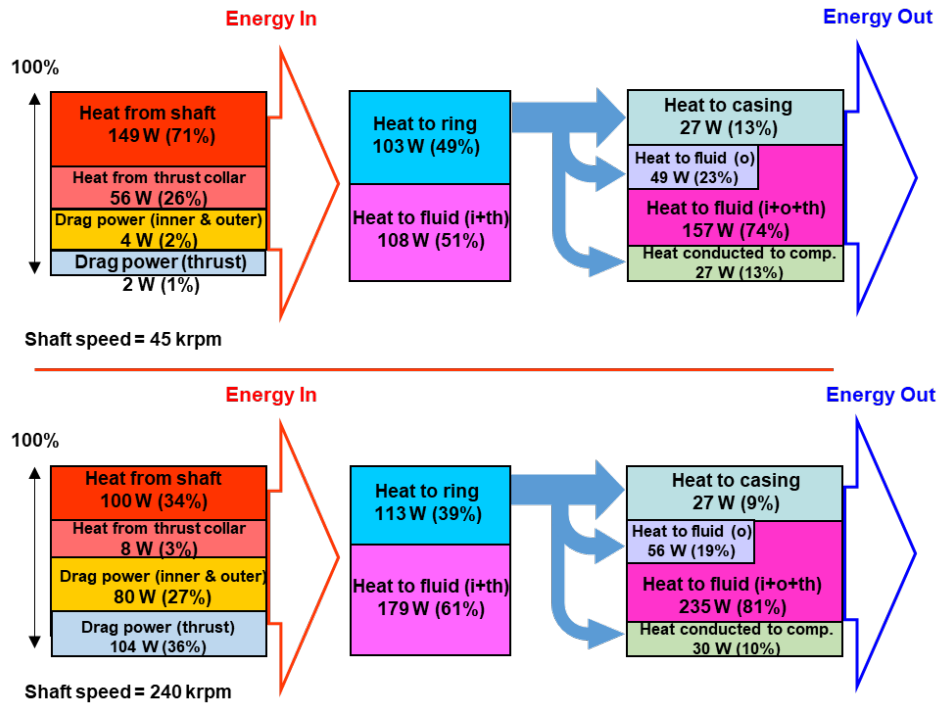
Figure 19. Schematic representation of thermal energy flows in turbine bearing. Predictions at a low speed (45 krpm) and at a high speed (240 krpm). Brass ring; α_{brass} = 1.8E-05, C_p = 377 J/kg-C°, ρ_R = 8,500 kg/m^3, $\kappa_{R,brass}$ = 58.1 W/m-C°.

Effect of ring material on SFRB heat flows

As the ring conducts a considerable portion of heat, it is important to quantify the effect of ring material on the bearing performance. Presently, a steel ring replaces the (original) brass ring. Note that steel ring is more conductive ($\kappa_{R,steel}$ = 73.0 W/m-C°) than brass ring ($\kappa_{R,brass}$ = 58.1 W/m-C°); hence the choice which does not consider key factors such as weight, and material and manufacturability costs. Note also that steel has a lower coefficient of thermal expansion than brass does; see Table 1.

Figure 20 shows schematic representations of the thermal energy flows in the turbine bearing system with a steel ring for operation at a low and a high shaft speed, 45 krpm and 240 krpm. Note that the bearing system with a steel ring transfers less total heat than a brass ring does. The steel ring conducts a larger fraction of the total heat, 60%-64%, than a brass ring does, 39%-49%, as shown in Fig. 19. The energies conducted into the TC casing, 11% -15%, and toward the compressor bearing, 14%-15%, are larger with the steel ring than those a brass ring would conduct. With a steel ring, the lubricant carries away less heat, 70%-74% than the brass ring does, 74%-81% of the total energy flow. As a result, a ring with more conductive material and a lower thermal expansion coefficient leads to a more effective conduction of thermal energy flows, in particular the one from the thrust bearing.
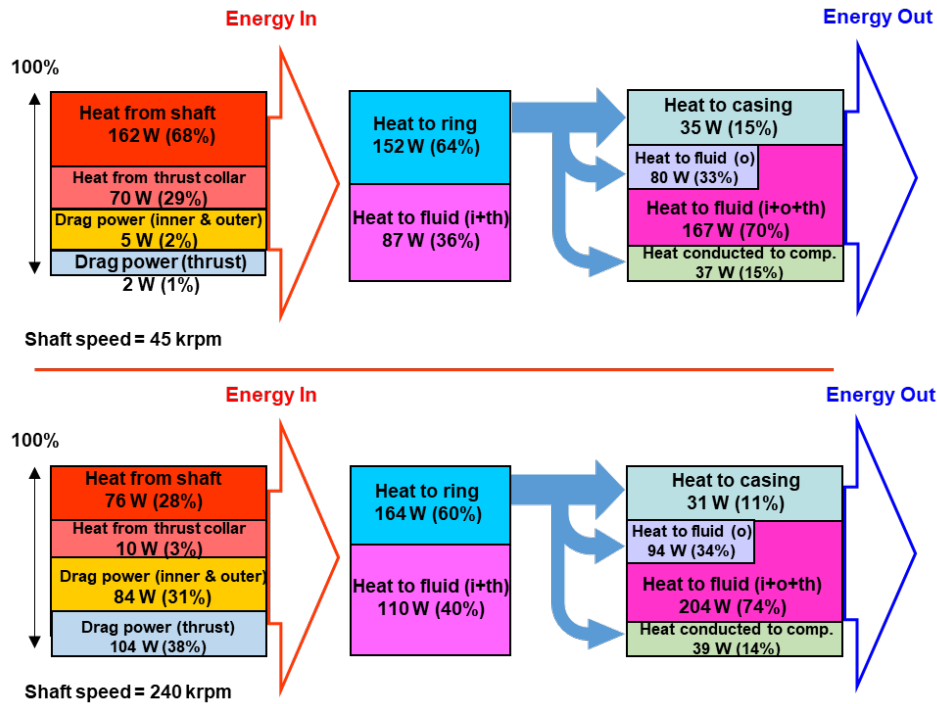
Figure 20. Schematic representation of thermal energy flows in a turbine bearing. Predictions at a low speed (45 krpm) and at a high speed (240 krpm). Steel (0% C) ring; α_{steel} = 1.2E-05, C_p = 452 J/kg-C°, ρ_R = 7,897 kg/m³, $\kappa_{R,steel}$ = 73.0 W/m-C°.

Effect of ring outer film length on SFRB heat flow transport

A ring with a large area $A_o = (\pi \times D_o \times L_o)$ would dispose more heat into the outer film; hence enabling an adequate path for managing heat flow transport. Note that a longer L_o > 7 mm (nominal length) adds resistance to the flow through the outer film which would then decrease. That is, the total flow supplied to the TC SFRB system decreases.

Figure 21 shows the heat flows versus the length of the outer film (L_o) for shaft operation at 240 krpm (ΩR_i = 99.5 m/s) and considering a brass ring. The total energy flow (heat flows from shaft and thrust bearing plus drag power losses) is nearly constant, as expected. Note as the ring conducts more energy flow, the heat flows carried by the inner

film and the thrust film decrease. On the other hand, the heat into the outer film decreases with an increase in L_o, while the heat into the casing and to the compressor bearing increase as the area to dispose energy flow increases. Thus, the total heat carried away by the lubricant decreases with L_o increasing.
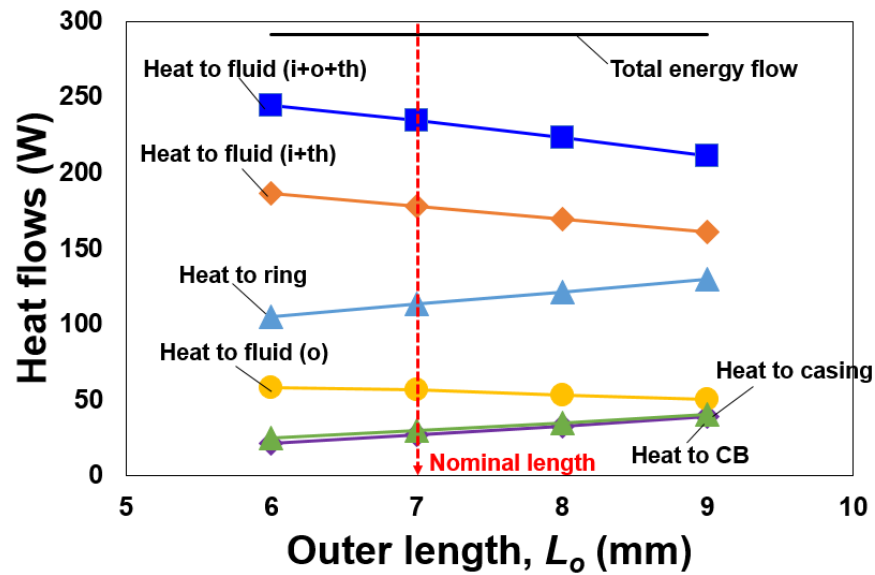
Figure 21. Heat flows versus outer film length (L_o). Shaft speed = 240 krpm. Nominal L_o = 7mm. Analysis with brass ring; L_i = 4.3 mm, L_o = 6 mm to 9 mm, D_i = 6 mm, and D_o = 11 mm.

This section presented a comprehensive model for the energy transport in SFRBs for automotive TCs. The model includes both radial bearings, inner and outer, and the thrust bearing, as well as a three-dimensional heat conduction model for the ring. Predictions obtained for a SFRB used in a passenger vehicle TC show that the ring temperature varies in all directions, in particular axial due to heat conducted from the thrust bearing into the ring. The total energy flow equals the viscous drag power losses from the inner film in the radial bearing and the thrust bearing plus the heat soaked from the shaft.

A SFRB with a brass ring conducts a considerable portion of the heat from the inner film into the outer film; 49% - 39% of the total energy flow at a low and a high shaft speed, 45 krpm and 240 krpm. The lubricant flows, inner and outer, carry away the majority of the heat flow, 74% of total at a low shaft speed, and up to 81% at the highest shaft speed. The predictions show a more conductive ring material (steel vs. brass) or a longer outer film conduct more heat into the ring and casing; but ultimately the lubricant flow carries most of the thermal energy flow from viscous drag power losses and the heat from the shaft.

The model and predictions assist in the design of SFRB systems with engineered thermal energy flow paths, advected and conducted, that will improve TC efficiency and durability.

CHAPTER IV

LINEAR ROTORDYNAMICS MODEL AND PREDICTIONS[*]

Presently a TC rotor (and bearing) models is a collection of elastic beam finite elements and lumped masses and mass moments of inertia representing the turbine and compressor wheels. Mechanical elements with (linearized) spring and damping force coefficients represent the support bearings; though in a generic model, the fluid film bearing forces are complex functions of the rotor (or ring) position and velocity.

The equations of motion (EOMs) for a MDOF rotor-SFRB system are [28]:

$$\mathbf{M}\,\ddot{\mathbf{X}} + \left[\mathbf{C} + \mathbf{G}\Omega\right]\dot{\mathbf{X}} + \mathbf{K}\,\mathbf{X} = \mathbf{F_{stat}} + \mathbf{F_{dyn}}_{(t)} - \mathbf{F_{B}}_{\left(\mathbf{X},\dot{\mathbf{X}},\Omega,t\right)} \tag{28}$$

where $\mathbf{M, G, K, C}$ are global matrices of rotor inertias, gyroscopic, elastic stiffness and damping coefficients, respectively, and Ω is shaft speed, $\mathbf{F_{stat}}$ and $\mathbf{F_{dyn}}$ denote the vectors of static and dynamic loads acting on the rotor, and $\mathbf{F_B}$ represents the vector of bearing reaction forces. .

With $\mathbf{F_{stat}}$ and $\mathbf{F_{dyn}}$ known, EOMs (28) are casted as a set of first-order differential equations with the system state-space vector $\left[\mathbf{X},\dot{\mathbf{X}}\right]_{(t)}$ as a generic unknown, and a procedure solves these equations at discrete instants of time. The rotordynamics model [42] offers a number of integrator choices for the numerical solution; for example Runge-Kutta, Rosenbrock, Average-Acceleration, etc. The proper selection of the numerical

---

[*] Content reproduced with permission from Jung, W., San Andrés, L., 2021, "A Nonlinear Rotordynamics Models for Automotive Turbochargers Coupled to a Physical Model for (Semi) Floating Ring Bearing System," Final Technical Report to KeyYang Precision Co., Ltd., TEES Project 408670 0001.

method (*solver*) and the time step for numerical integration are crucial to obtain accurate results. In addition, the accuracy of the (nonlinear) *solver* relies on the initial state $\left[\mathbf{X},\dot{\mathbf{X}}\right]_{(t=0)} = \left[\mathbf{X}_o,\dot{\mathbf{X}}_o\right]$ representing a true or actual physical condition.

San Andrés et al. (2003-2012) developed increasingly complex physical and numerical models for evaluation of the TC dynamic response [12,13,25-28]. The rotordynamics model integrates a fluid film bearing analysis program that calculates the mechanical element reaction force vector as a function of the current state (rotor position and velocity). The numerical time-transient procedure evaluates the system response while the TC operates at a constant speed or during constant acceleration or deceleration paths toward or from a top shaft speed. The procedure is quite time consuming because of the bearings' nonlinearity. If desired, the model assumes the bearings behave linearly and performs the same procedure using stiffness and damping force coefficients that change with rotor speed [3]. The linear model is rather fast and delivers the system damped natural frequencies and damping ratios (and mode shapes) as well as the rotor synchronous response to specified mass imbalance conditions.

In typical TC rotors, the compressor and turbine wheels, large in size and mass, largely contribute to the imbalance state. The manufacturing process and first balancing of components (C and T) followed by the final (trim) balancing of the rotating assembly are important. In addition, the clocking or relative positioning of the components and the assembly torque (stretch load on the shaft) contribute to the final balancing state, and which is difficult to repeat after disassembly. Table 2 lists the physical properties of a commercial TC rotor-SFRB system including locations for mass imbalance and their magnitudes, as

provided by the TC manufacturer. Note that the imbalance grades are ISO 1940 G40 for the compressor wheel and G16 for the turbine wheel.

Figure 22 shows a structural model for the TC with 60 elements modeling the thin steel rotor that includes a thrust collar and spacer, and 20 elements modeling the brass SFRB with connection to (lateral) bearings at the ring ends. The compressor wheel (left side) and the turbine wheel (right side) are modeled as low density components with known lumped mass and mass moments of inertia, polar and transverse. The inner film is a spring-like structure connecting the rotor to the ring, whereas a spring-like structure connecting the ring to ground represents the outer film.
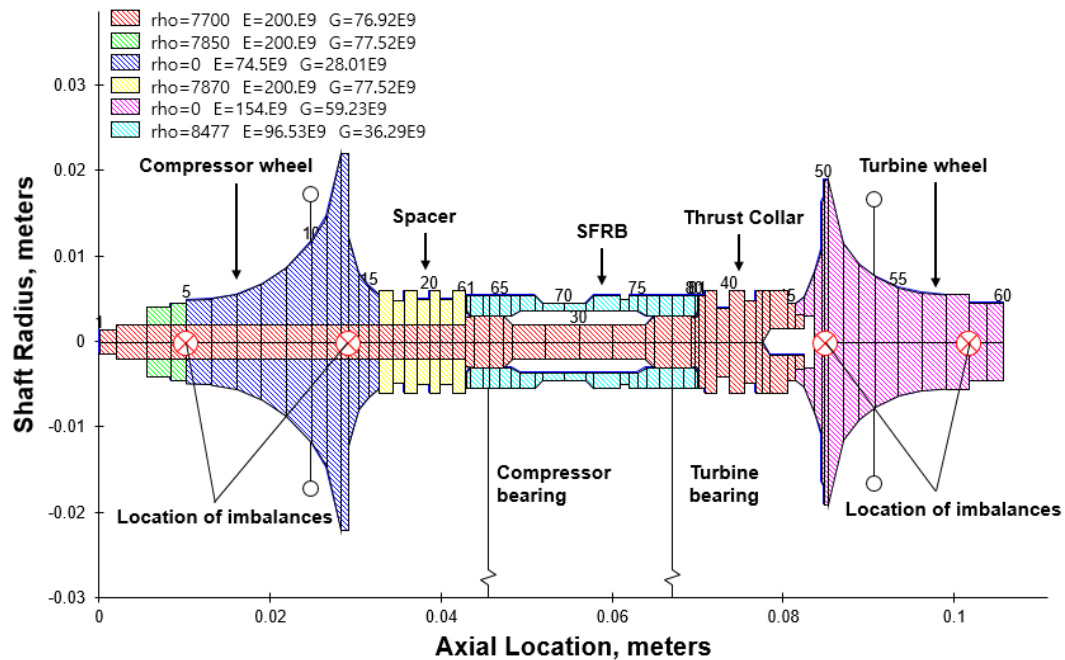
Figure 22. Example of finite element structural model for TC rotor-SFRB system.

Table 2. Physical properties of TC rotor-bearing system including locations for mass imbalances and amounts. Imbalances' phase angle relative to horizontal plane.

Mass of TC rotor [g]		TC rotor length [mm]		C.G. location (from compressor end) [mm]	
100		105.7		66.1	
Station #	**Components**	**mass [gram]**	**Ip [g-cm²]**	**It [g-cm²]**	
10	Compressor wheel	22	28	19	
54	Turbine wheel	54	48	40	
Station #	**Location**	**Imbalance amount [gram-mm]**		**Imbalance phase [degree]**	
5	Comp. nose	0.015		90	
13	Comp. back face	0.027		90	
49	Turbine back face	0.026		90	
58	Turbine nose	0.016		90	

To validate the rotordynamics model, experiments with the rotor alone show its elastic free-free mode natural frequencies. The rotor is suspended from long wires and an impact hammer excites it. Two miniature (1 gram) accelerometers, one fixed and one roaming, produce data from which to extract the rotor mode shapes. Figure 23 shows both the measured and predicted mode shapes for the first two free-free mode natural frequencies. The experiments identify the first two natural frequencies as f_1 = 996 Hz and f_2 = 4,328 Hz while the predictions show a minute difference, f_1 = 995 Hz and f_2 = 4,320 Hz. The lowest natural frequency (996 Hz) is within the range of speed operation for the TC that reaches a maximum of 4,000 Hz (240 krpm). Note the free-free, elastic rotor modes show large deflections at the compressor side, the lighter component.

Similarly, for the floating ring alone, its free-free mode natural frequencies (> 28,000 Hz) are well above the shaft top speed.
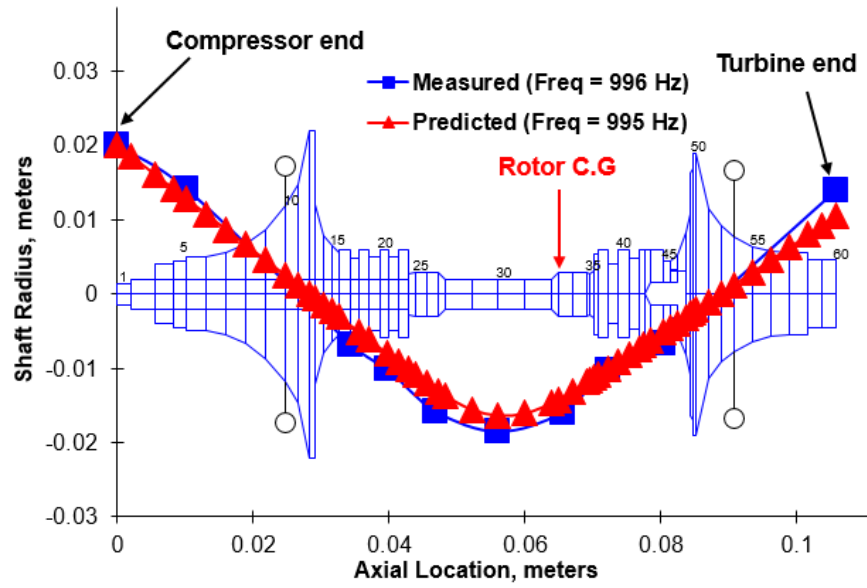
(a) First mode
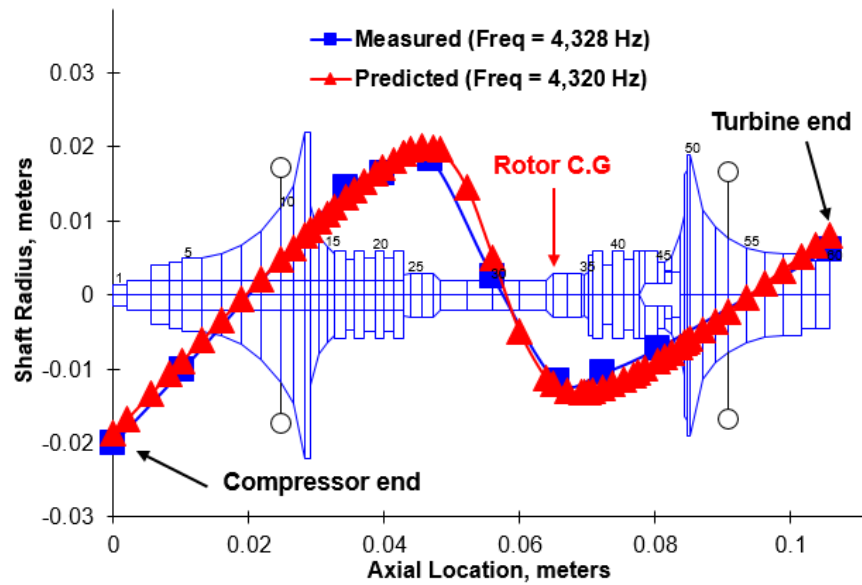
(b) Second mode

Figure 23. TC rotor: Measured and predicted first and second free-free, elastic mode shapes and natural frequencies. (Ring NOT included).

Prediction of natural frequencies and damping ratios for TC

Assuming the bearings, inner and outer films, behave as linear mechanical elements with stiffness (K) and damping (C) coefficients, the rotordynamics model produces the TC system damped natural frequencies and damping ratios (ζ) vs. shaft speed, as depicted in Figure 24. The insets show the rotor and ring forward whirl mode (FWM) shapes for operation at shaft speed = 95 krpm. In the graphs, the left and the right sides of a mode shape correspond to the compressor end and turbine end respectively.

(a) Damped natural frequencies

First FWM: 242 Hz, $\zeta=-0.29$ Second FWM: 465 Hz, $\zeta=-0.26$ Third FWM: 1,093 Hz, $\zeta=+0.13$
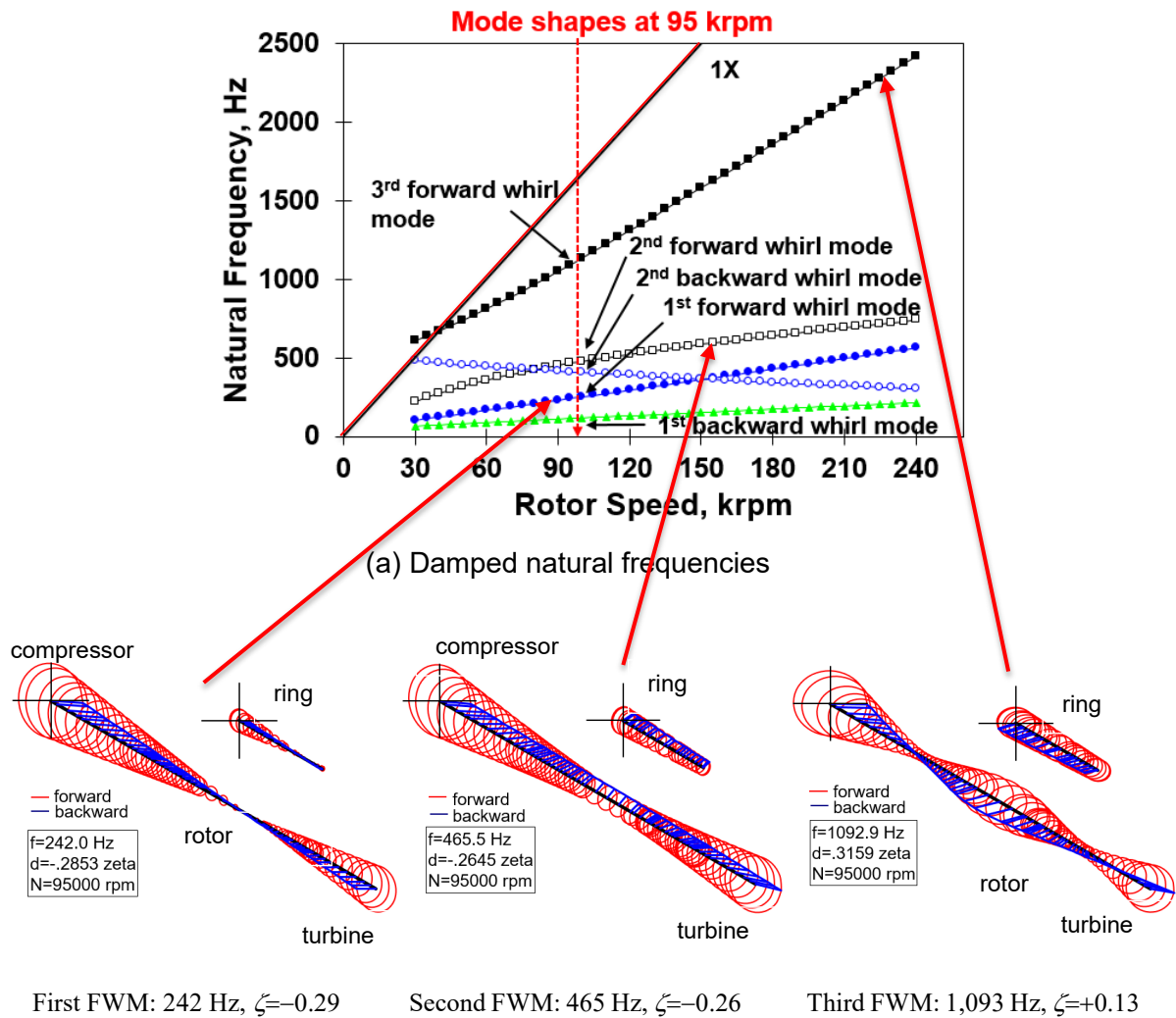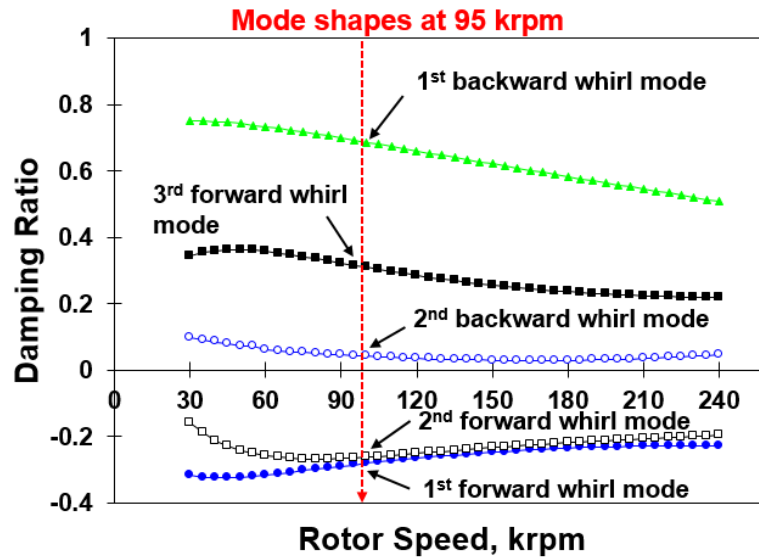
(b) Damping ratios

Figure 24. TC rotor-SFRB: Predicted damped natural frequencies and damping ratios versus speed, and forward whirl modes at speed = 95 krpm (1,583 Hz).

Of interest are the forward whirl modes and their respective damping ratio (ζ). The lowest two forward whirl modes (FWM) show negative damping ($\zeta < 0$) and correspond to a conical mode and a cylindrical-bending mode of the rotor, while the ring modes are conical and cylindrical respectively. The third FWM has $\zeta > 0$ (i.e. stable) and represents a true elastic mode for the rotor while the ring remains in a rigid cylindrical mode. The FWM natural frequencies follow the shaft speed (Ω) with a nearly constant fractional ratio. Figure 25 shows the predicted ratio of the damped natural frequencies to shaft speed for FWM versus rotor speed. It is important to realize that the first two FW modes are the ones that will be excited when the system becomes unstable. Note that as shaft speed increases the ratio (whirl frequency/shaft speed) decreases. This is since the TC rotor operates well above the RBS natural frequencies (two rigid body modes and a third elastic mode).
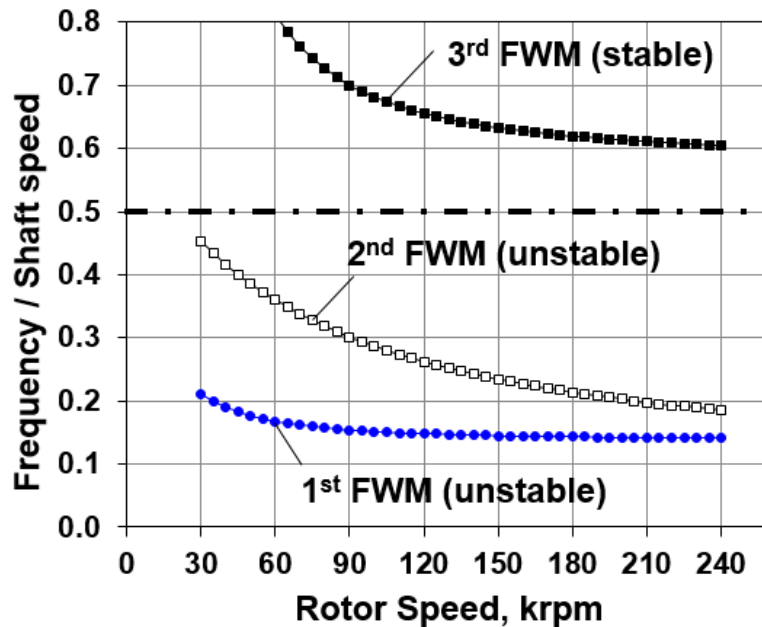
Figure 25. TC rotor-SFRB: Ratio (natural frequency / shaft speed) for forward whirl modes versus rotor speed.

Obtained from the linear analysis, Figure 26 shows the predicted amplitude of imbalance synchronous rotor response at the compressor end (station #3 in Fig. 3) and at the turbine end (station #58 in same Fig.). The model applies the imbalance at the nose and the back faces of the compressor and the turbine, respectively, see Table 2. Note that the amplitude of motion at the compressor side is the largest for the first two (unstable) forward whirl modes. The synchronous response from the linear rotordynamics analysis shows peak amplitudes at 45 krpm (750 Hz), which is likely due to the rotor speed exciting the first elastic mode (3rd FWM) as shown in Fig. 24. The deformed rotor mode shapes also show a larger peak response at the compressor end compared to the one at the turbine end. Note that a maximum allowed physical amplitude for rotor motions at the compressor end is 0.175 mm (0-pk). Note also that the maximum magnitudes in the insets depict the imbalance synchronous rotor response at the compressor end (station #3 in Fig. 22).

66
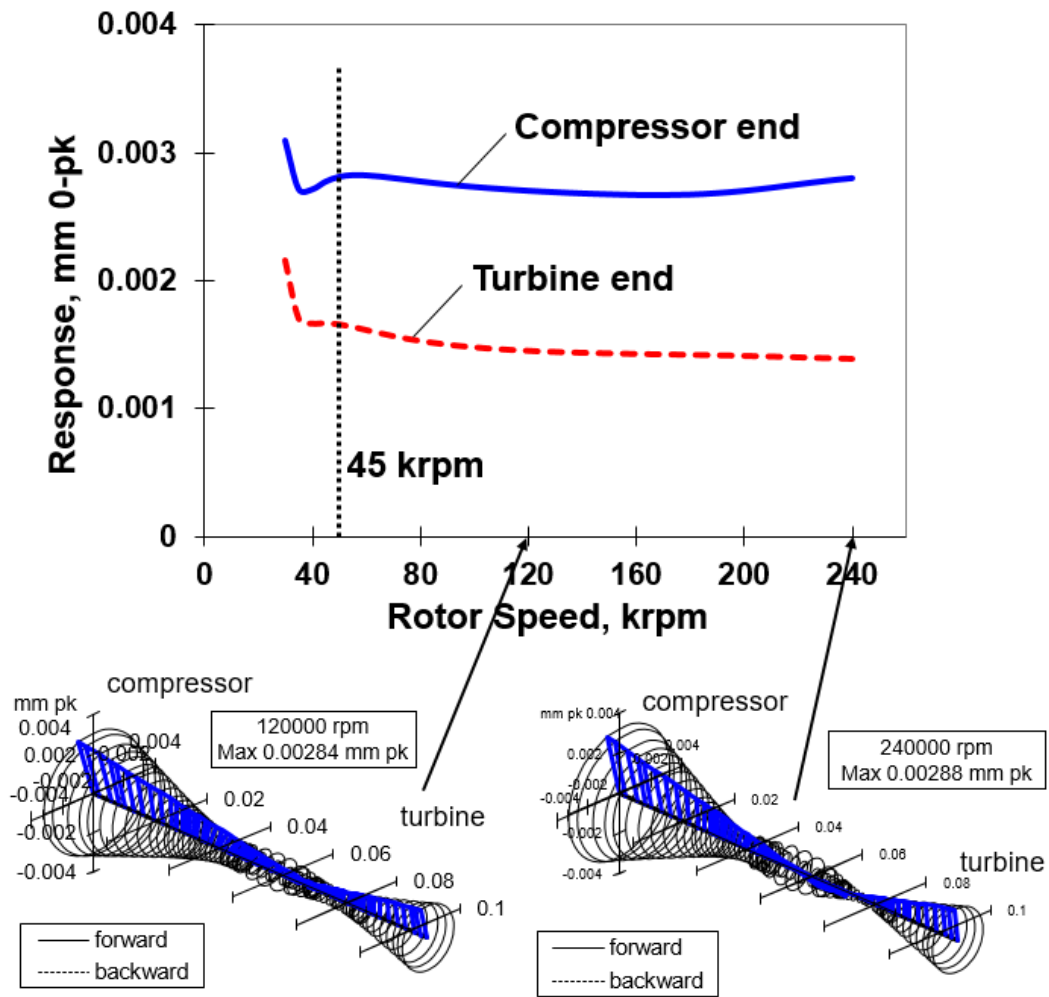
Figure 26. Predicted amplitude of TC rotor synchronous response at compressor and turbine ends (vertical direction). Results from linear rotordynamics analysis.

CHAPTER V

PREDICTION OF NONLINEAR TC ROTOR-SFRB RESPONSE[*]

Comparison of predictions versus test data

This section presents predictions of the nonlinear TC system response corresponding to the operating conditions detailed in a prior section, see Tables 1 and 2. The rotor speed ranges from Ω_1= 30 krpm (500 Hz) to Ω_2= 240 krpm (4 kHz), hence the period of synchronous whirl motion varies from T_1 = 2 ms to T_2=0.25 ms. For the nonlinear solution, the numerical integration time step ΔT= 0.1 ms = $T_1/20$ and $T_2/2.5$. The ΔT for the low speed is enough to capture a period of synchronous motion but barely enough to deliver accurate results for the highest shaft speed condition. As a fact, $T_2/2.5$ barely satisfies the Nyquist criterion of $T_2/2 = 0.125$ ms. However, it is of interest to analyze the rotor motion at low shaft speeds where the largest amplitudes of rotor motion appear.

The number of integration steps equals to N_t = 5,000 so the elapsed time t_{max}= N_t ΔT=500 ms. The integrator chosen is the Rosenbrock method [43] which is an implicit procedure. The initial conditions are set to be the rotor and bearing static equilibrium position due to the rotor weight (deflected rotor shape). Note that over the elapsed t_{max}, the number of full rotor revolutions equal t_{max}/T =250 and 2,000 for the lowest and highest shaft speeds, respectively.

---

[*] Content reproduced with permission from Jung, W., San Andrés, L., 2021, "A Nonlinear Rotordynamics Models for Automotive Turbochargers Coupled to a Physical Model for (Semi) Floating Ring Bearing System," Final Technical Report to KeyYang Precision Co., Ltd., TEES Project 408670 0001.

For analysis of the calculated rotor and ring motions, the algorithm keeps the last 2^{11} (= 2048) data points as it assumes that for $t > \frac{1}{2} \, t_{max}$ the effect of initial conditions is no longer important and that the system has achieved a quasi-steady state motion. The resolution of a discrete Fourier Transform (DFT) of the shaft motions is 4.9 Hz (294 rpm) that will capture the frequency of the lowest vibratory (unstable) modes that correspond to a conical rigid body mode and a cylindrical-bending mode of the rotor, while the ring modes are conical and cylindrical respectively.

A procedure [26,28] analyzes the predicted (or measured) time transient response data to produce the overall amplitude of rotor motion (orbit), extracts time segments of data to process using the discrete Fourier transform (DFT), assembles and displays waterfalls of rotor motion, and filters the DFTs to deliver the amplitude and frequency of (one or more) the subsynchronous vibrations (SSV), synchronous motions (1X), and super synchronous motions (if any).

Figure 27 shows a waterfall plot of the predicted rotor response at the compressor nose and along the vertical direction (station #3) aligned with the gravity plane. The graph shows the frequency content of the compressor response as the shaft increases from 30 krpm (bottom of graph) to the top speed of 240 krpm (top of graph). The straight lines on the graph indicate fractions of shaft speed at 1X (synchronous), ½ frequency whirl and ¼ frequency whirl. The predictions show motion with 1X component having an amplitude that increases moderately with shaft speed and one (or more) subsynchronous whirl frequencies that appear at ½ X to become ~ ¼ X at Ω= 180 krpm. For operation at higher

shaft speeds, the SSV disappears. Recall the linear analysis results shown in Fig. 25, predicts the rotor is unstable over the whole shaft speed range (30 krpm to 240 krpm).
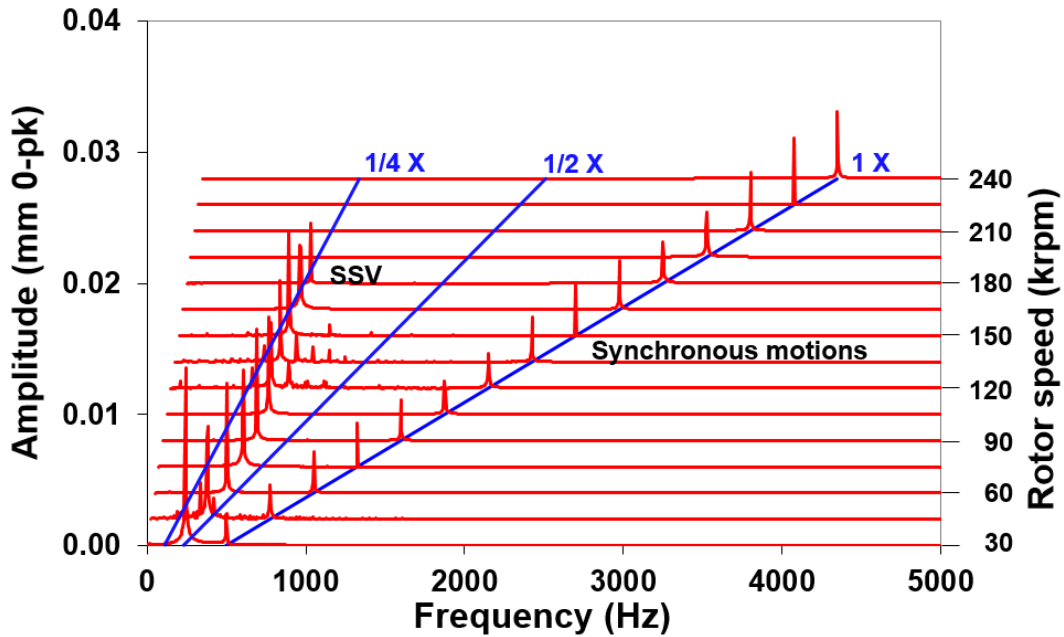
Figure 27. Waterfall plot of predicted rotor motion at compressor nose (station #3), vertical direction. Shaft speed = 30 krpm to 240 krpm. Lines denote fractions of shaft speed (1X).

Figure 28 depicts the waterfall of TC measured motions obtained in a hot gas test stand operated by the sponsor [44]. The rotor speed ranges from 30 krpm (500 Hz) to 210 krpm (3.5 kHz). The test elapsed time equals 120 s. Blue solid lines on the graph indicate fractions of shaft speed at ½ frequency whirl and ¼ frequency whirl. Note that the SSV disappears for shaft speeds above 3,000 Hz (180 krpm), same as with the predicted SSV shown in Fig. 27.
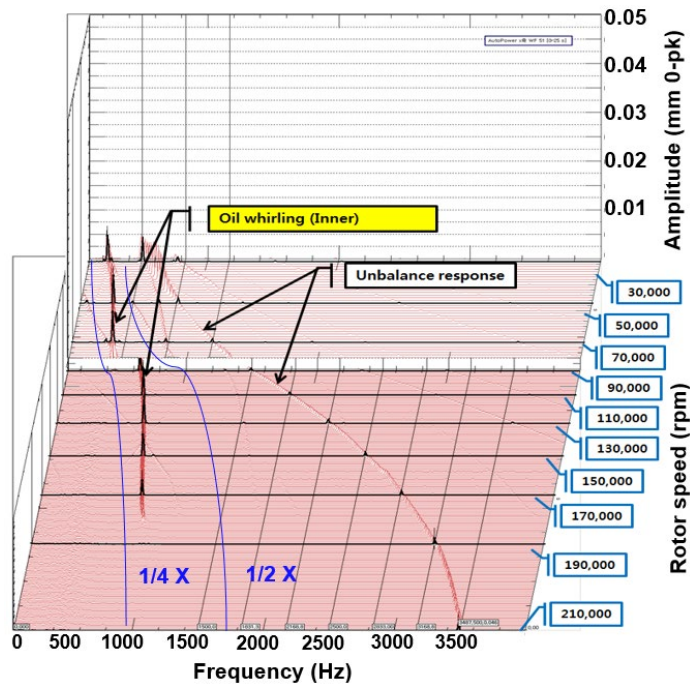
Figure 28. Waterfall plot of measured rotor motion at compressor nose, vertical direction. Shaft speed = 30 krpm to 210 krpm. Test data acquired at KeyYang Precision (KYP) [44].

An analysis of the measured and predicted motions is shown in Figure 29 that depicts the amplitude and frequency of SSV appearing up to a shaft speed of 180 krpm (3,000 Hz). The predictions are in good agreement with the measured SSV amplitude and the whirl frequency for low (30 krpm) to moderately high (180 krpm) shaft speeds. Note that a maximum allowed physical amplitude for rotor motions at the compressor end is 0.175 mm (0-pk).

Maximum physical amplitude = 0.175 mm (0-pk)
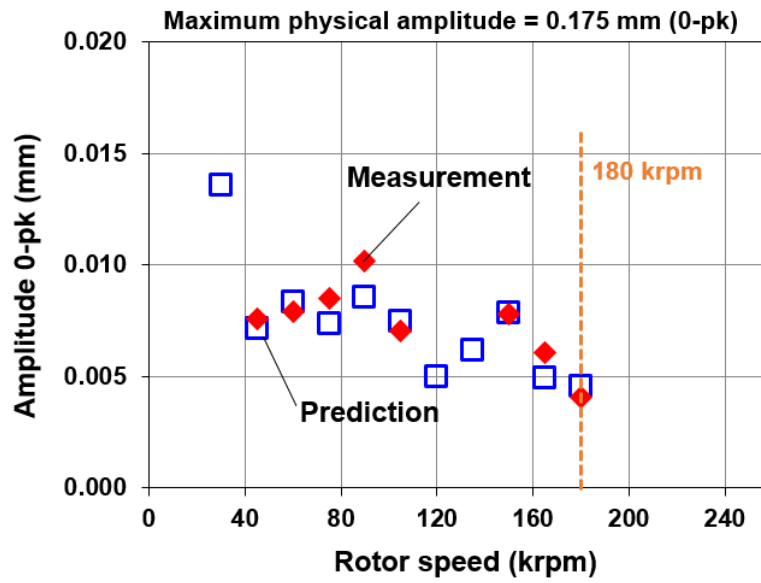
(a) Amplitude of SSV
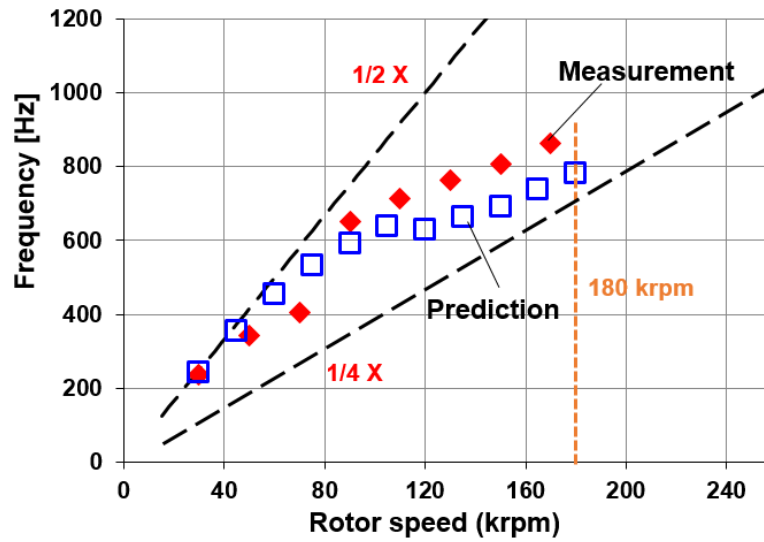
(b) Frequency of SSV

Figure 29. Amplitude and frequency content of SSV motions vs shaft speed. Measured at KYP [44] and predictions. Location; compressor nose, vertical plane.

Figure 30 shows the ratio of the SSV frequencies to shaft speed vs. shaft speed for both the linear and nonlinear models and the test data. The predicted and measured whirl motions follow the 2nd FWM which evolves from a cylindrical rotor mode (at low speeds) to a cylindrical-bending mode at the highest shaft speed. Both the predicted and measured whirl frequency ratios (WFR) are between ½ whirl frequency and ¼ whirl frequency. Note that the rotor mode changes from the cylindrical bending mode at low shaft speeds (~30 krpm) to a conical-bending mode at high shaft speeds (~240 krpm), due to a transition of the rotor mode between the close natural frequencies (~180 Hz = 10 krpm difference at 240 krpm), the 1st FWM (conical) and the 2nd FWM (cylindrical), see Fig. 24.
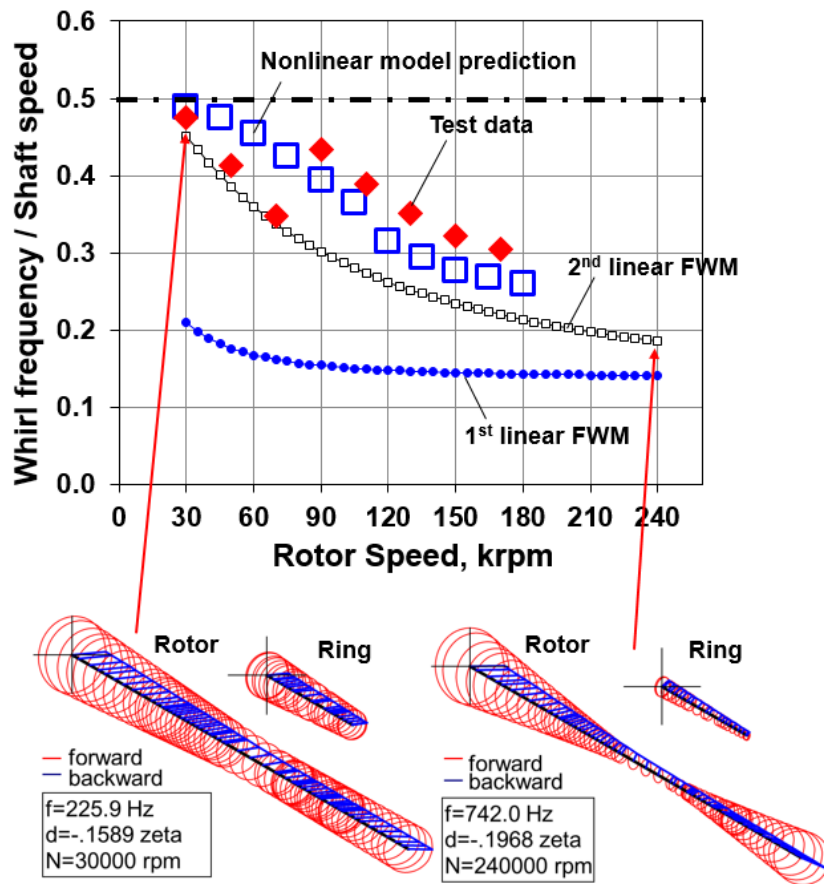
Figure 30. Ratio of SSV whirl frequencies to shaft speed from linear and nonlinear models and test data versus rotor speed.

73

Baseline case for parameter study of nonlinear TC rotordynamic response

Table 3 lists the physical properties of a commercial TC rotor-SFRB system including locations for mass imbalances and their magnitudes. Note that the imbalance grade is ISO 1940 G100 for the rotor-SFRB system. The high imbalance grade is necessary since the rotor speed is high [24]. For a lower imbalance grade, the acceptable balance radius e_{lim}, i.e. the distance from the rotor center to the location where balancing takes places becomes too small.

Table 3. Physical properties of TC rotor-bearing system including locations for mass imbalances and amounts. Imbalances' phase angle relative to horizontal plane.

Mass of TC rotor [g]		TC rotor length [mm]	C.G. location (from compressor end) [mm]	
112		105.7	65.1	
Station #	Components	mass [gram]	Ip [g-cm²]	It [g-cm²]
10	Compressor wheel	22	28	19
54	Turbine wheel	54	48	40
Station #	Location	Imbalance amount [gram-mm]	Imbalance phase [degree]	
5	Comp. nose	0.011	0	
13	Comp. back face	0.037	0	
49	Turbine back face	0.049	0	
58	Turbine nose	0.028	0	
		0.125		

For the balancing quality grade of G100 for an automotive TC [24],

$$e_{\text{lim}} = \frac{100\,mm/s}{\Omega} \tag{29}$$

where Ω is the rotor speed (rad/s). At the maximum rotor operational speed of 280 krpm (28,320 rad/s), $e_{\text{lim}} = 3.4$ μm. With a total rotor mass $m = 112$ gram in Table 3, the total

permissible residual unbalance for the entire rotor-SFRB system at G100 is $U_{\text{lim}} = m \times e_{\text{lim}} = 0.382 \,\text{gram-mm}$. As the rotor configuration has correction (balancing) planes on the compressor and the turbine wheels outside the bearings, the adjusted U_{lim} by the ISO 1940 balance quality requirements [45] is

$$U_{\text{lim,adjusted}} = U_{\text{lim}} \times (\text{distance between bearings / distance between wheels}) \quad (30)$$

$$= 0.382 \,\text{gram-mm} \times (21.48 \,\text{mm} / 65.89 \,\text{mm}) = 0.125 \,\text{gram-mm}$$

The geometric parameters for the rotor-bearing system and operating conditions for the baseline analysis case are

- Oil supply pressure and temperature: 3 bar and 120 ℃
- Lubricant type: SAE 10W30 ($\mu^* = 6.39$ c-Poise at 120 ℃)
- Bearing type: SFRB
- Bearing inner film clearance (c_i^*): 7.5 μm at 20 ℃
- Bearing inner film length (L_i^*): 4.3 mm
- Shaft diameter (D_i^*): 6 mm
- Mass imbalance amounts and distribution: see Table 3, total 0.125 gram-mm, all-in-phase

For the baseline case, Figure 31 shows a waterfall plot of the predicted nonlinear transient response of the TC at the compressor nose and along the vertical direction. The predictions show that subsynchronous rotor motions occur at about 1/5~1/2 shaft speed from 500 Hz (30 krpm) to 4,000 Hz (240 krpm).
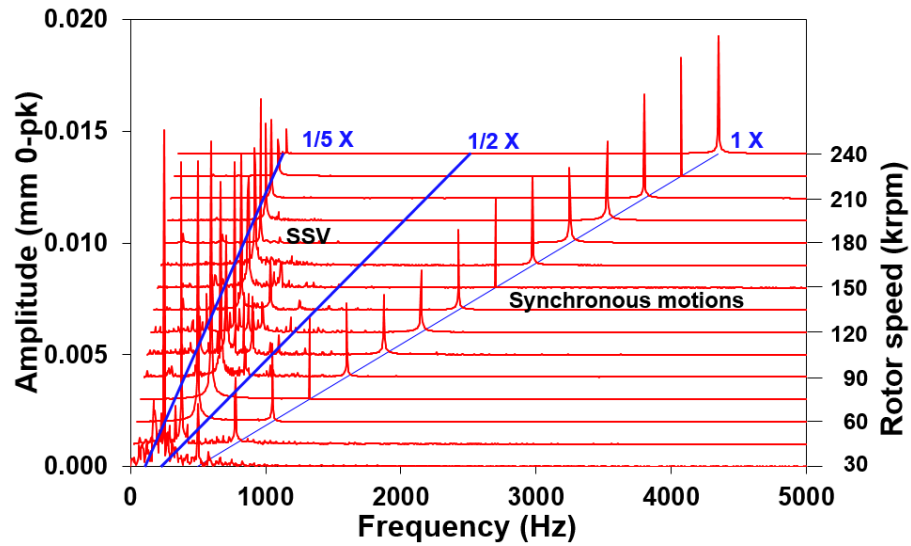
Figure 31. Waterfall plot of nonlinear transient prediction at compressor nose (station #3), vertical direction. Rotor speed = 30 krpm to 240 krpm. Baseline case.

Effect of films' inner clearance on TC-SFRB rotordynamic response

As the ring does not rotate during the operation at a TC rotor-SFRB application, the SSVs occur mainly due to the oil whirl in the inner films. Thus the analysis focuses on the influence of the inner film clearance (c_i) on the rotor motions at the compressor nose. This rotor location shows the largest amplitude motions, see Fig. 26 (page 67).

Recall, see page 71, that a maximum allowed physical amplitude for rotor motions at the compressor end is 0.175 mm (0-pk). For a SFRB with c_i*= 7.5 μm (nominal), 6 μm (20% smaller than c_i*), and 9 μm (20% larger than c_i*), Figure 32 shows the predicted total amplitude of shaft motion at the compressor nose versus rotor speed. The total shaft motion is important for qualification of a TC as it is an upper bound to the rotor motion amplitude because it adds (in vector form) the various components of motion such as synchronous, subsynchronous, and super synchronous [28].

The predicted results show that the total shaft motion amplitudes for the TC-SFRB with c_i =9 μm are ~20 % larger than those for the TC-SFRB with nominal c_i* =7.5 μm. On the other hand, the total shaft motion amplitudes for the TC-SFRB with c_i =6 μm are ~23 % smaller than those for the TC-SFRB with c_i* =7.5 μm. These results show that for this case SSV amplitudes increase with an increase of the inner film clearance (c_i).

For the TC-SFRB with c_i = 6 μm (20% smaller than c_i*), Figure 33 shows a waterfall plot of the nonlinear transient response of the TC at the compressor nose and along the vertical direction. From 30 krpm (500 Hz) to 180 krpm (3,000 Hz), the prediction shows that rotor SSV motions occur at frequencies within 1/5~1/2 of shaft speed.

For a SFRB with c_i* = 7.5 μm, 6 μm (20% smaller than c_i*), and 9 μm (20% larger than c_i*), Figure 34 shows the rotor SSV frequency content at the compressor nose versus rotor speed. The predicted results also show that for low rotor speeds (~45 krpm), the rotor whirl frequencies are quite similar (~240 Hz to ~350 Hz) for the TC-SFRB with any of the three inner film clearances. Above a shaft speed of 180 krpm (3,000 Hz), however, the subsynchronous frequencies for the TC-SFRB with c_i=6 μm disappear while the ones for the other inner film clearances persist. This is likely because the SSV motion amplitudes for the TC-SFRB with c_i=6 μm vanish as the rotor speed increases above 180 krpm. For the TC-SFRB with c_i=6 μm, the rotor deflected mode shapes [50] show a conical mode at 244 Hz for a rotor speed of 30 krpm corresponding to the rotor mode shape of 1st FWM; and a cylindrical-bending mode at 762 Hz for a rotor speed of 180 krpm corresponding to the rotor mode shape of 2nd FWM, respectively, as seen in the inset graphs.

In Fig. 34, the solid lines trace the 1st FWM and the 2nd FWM for the TC-SFRB with nominal c_i*=7.5 μm. Note that each inner film clearance determines natural frequencies and mode shapes for the rotor-bearing system. As the inner film clearance increases ~50 %, from 6 μm to 9 μm, the magnitude of the 1st FWM natural frequency decreases ~23 %, and the magnitude of the 2nd FWM natural frequency decreases ~4 %. The results show that as the rotor speed increases, the rotor motion subsynchronous frequencies for a bearing system with the larger inner film clearance (c_i =9 μm) are lower than the rotor subsynchronous frequencies for the bearing system with a smaller inner film clearance (c_i =6 μm).

Figure 32. Amplitudes of total shaft motion versus shaft speed. Location; compressor nose, vertical plane. Predictions obtained for SFRB inner film clearance c_i =7.5 μm (± 1.5 μm).

Figure 33. Waterfall plot of rotor nonlinear transient response at compressor nose, vertical plane. Rotor speed = 30 krpm to 240 krpm. Prediction obtained for a SFRB with inner film clearance c_i =6 μm.

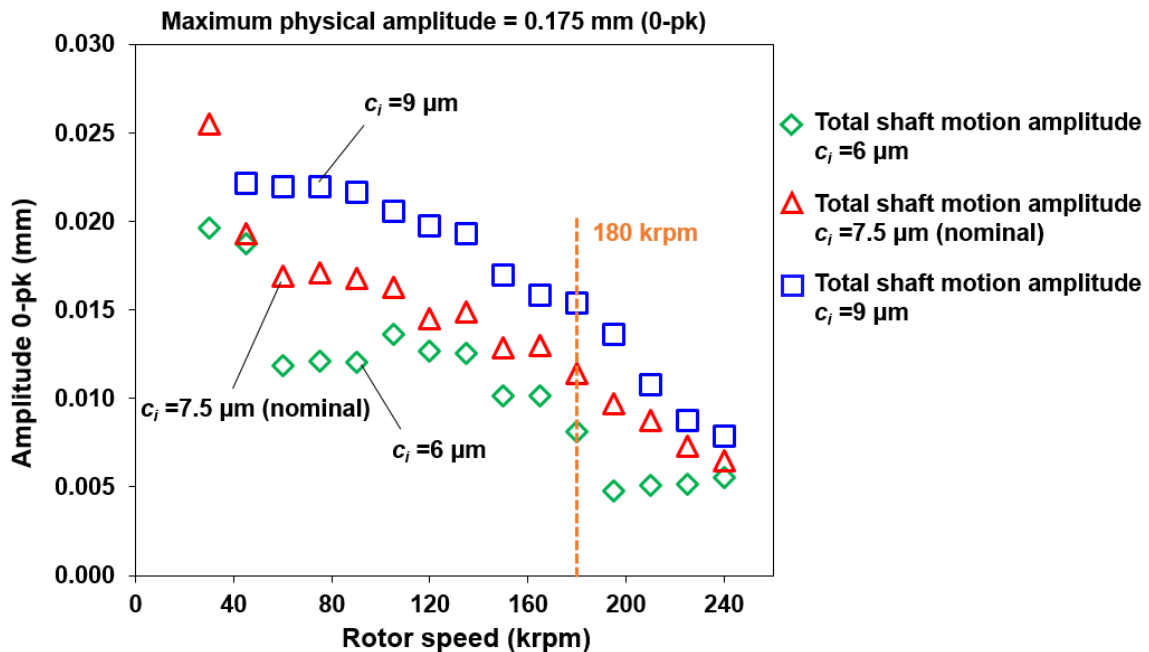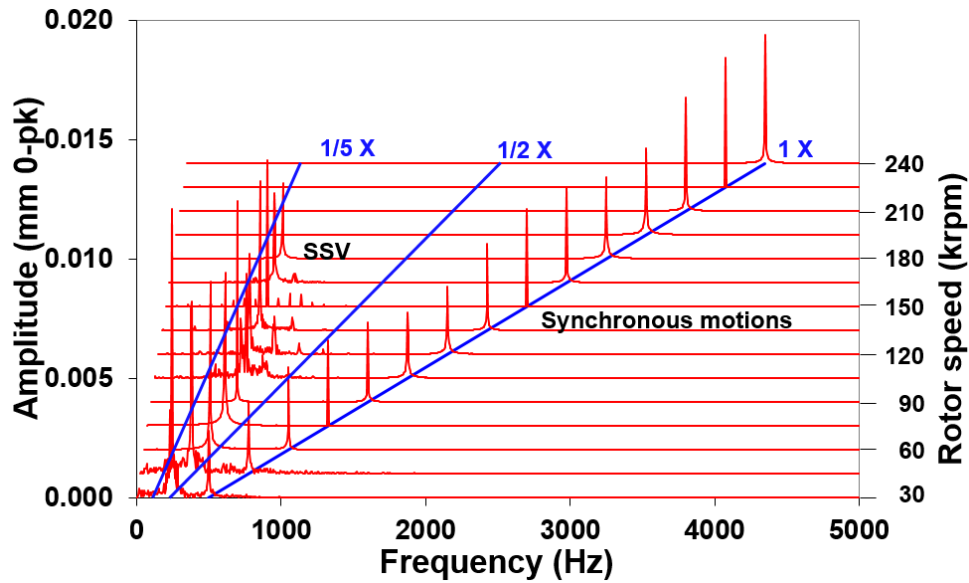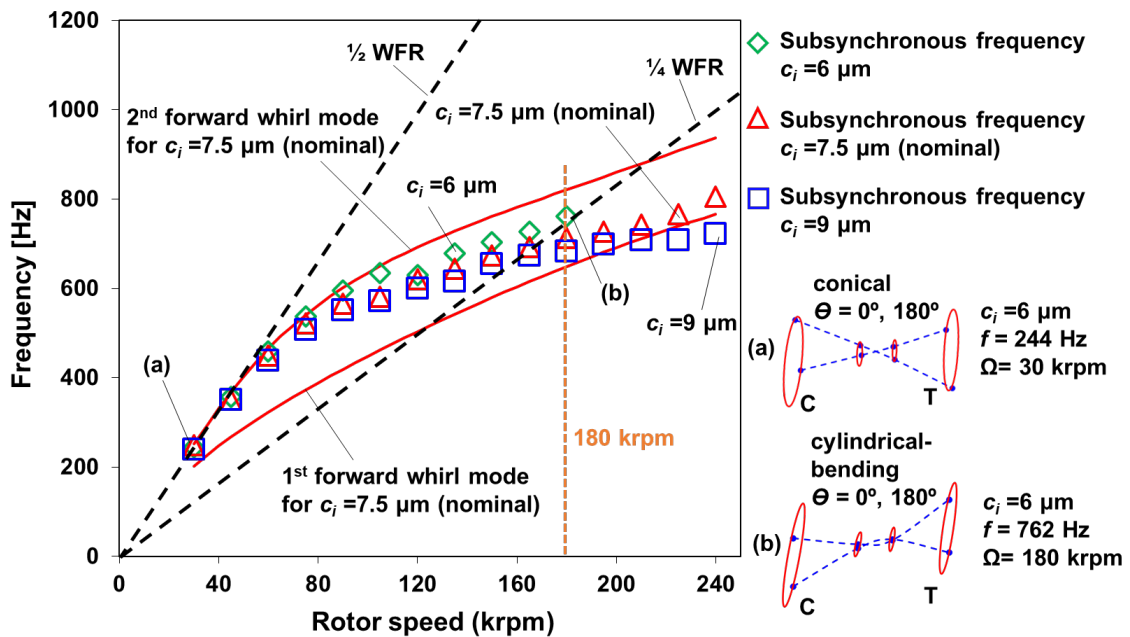**Figure 34. Rotor SSV frequencies versus shaft speed. Location; compressor nose, vertical plane. Predictions obtained for SFRB inner film clearance c_i =7.5 μm (± 1.5 μm). Insets show rotor deflected mode shapes.**

Figure 35 shows a comparison of the rotor motion amplitudes 0 - pk for the rotor-SFRB system with a nominal c_i*=7.5 µm versus the rotor motion amplitudes for the TC-SFRB with c_i=6 µm and c_i=9 µm. For any of the three inner film clearances, the rotor synchronous response amplitudes (1X) are almost the same. However, the subsynchronous response amplitudes (SSV) for the rotor-SFRB system with c_i=9 µm are the largest, while the subsynchronous response amplitudes for the TC-SFRB with c_i=6 µm are the smallest. Note that there are no subsynchronous response components for the rotor-SFRB system with c_i=6 µm at rotor speeds above 180 krpm (3,000 Hz), as also shown in Figure 34.
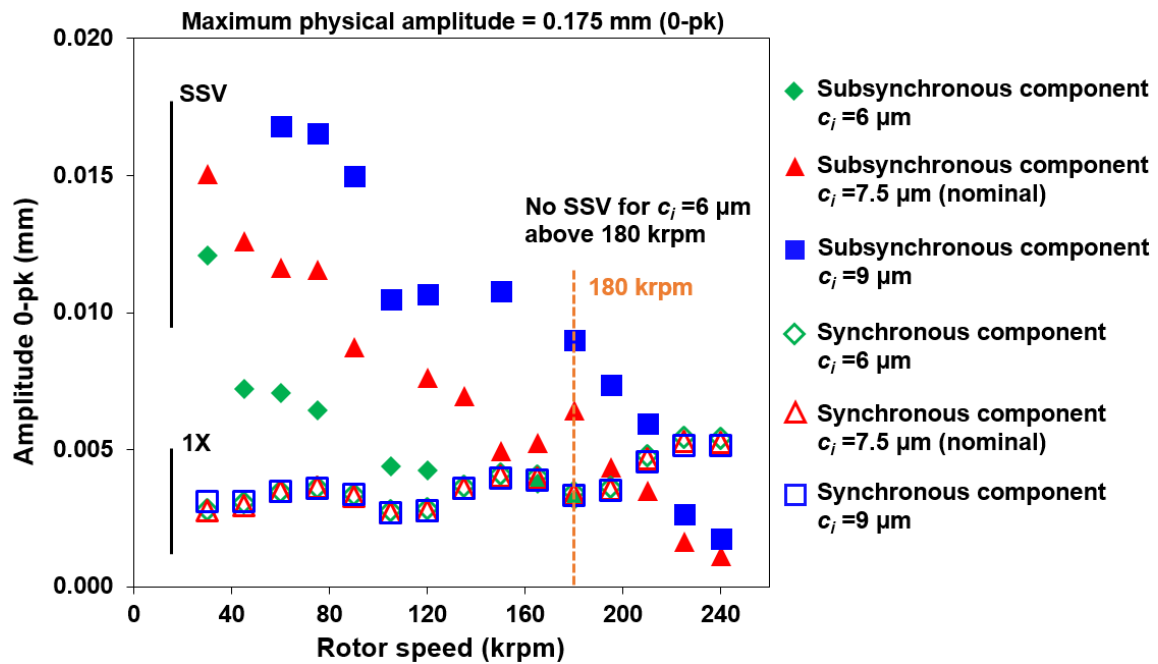
Figure 35. Amplitude components of rotor synchronous and subsynchronous motions (0 to pk) at compressor nose versus rotor speed. Comparison of rotor responses obtained for SFRB inner film clearance c_i = 7.5 µm (± 1.5 µm).

80

Effect of lubricant viscosity on TC-SFRB rotordynamic response

The viscosity of the lubricant for a TC rotor-SFRB system is of interest as the proper oil selection is crucial for TC performance. Table 4 lists the physical properties at $T_{SUP} =$ 120 ºC for SAE 5W10, SAE 10W30 (nominal), and SAE10W40 lubricants. The viscosity (μ) is a function of temperature written as

$$\mu_0 = \mu_R \, e^{\alpha(T-T_R)} = \mu_0(T) \tag{30}$$

where α is a viscosity-temperature coefficient, and μ_R and T_R are the reference viscosity and temperature, respectively. μ also decreases with an increase in lubricant shear rate. The analysis implements Cross equation [39] which accounts for shear thinning effects in the lubricant viscosity. At a specific temperature,

$$\mu(\gamma,T) = \mu_\infty + \frac{\mu_0(T) - \mu_\infty}{1 + |\gamma/\gamma_c|} \tag{31}$$

where μ_∞ is the viscosity at an infinitely high shear rate ($\gamma = U/c$) and μ_0 is the zero shear rate viscosity. γ_c is the shear rate where the lubricant viscosity is exactly 50 % of $(\mu_0 + \mu_\infty)$.

Table 4. Lubricant properties for TC rotor-bearing system at T_{SUP} = 120 ºC.

Lubricant type	Viscosity, μ (c-Poise)	Viscosity-temperature coefficient, α (1/ºC)	Shear rate, γ_c (1/s)
SAE 5W10	1.4	-0.011	1
SAE 10W30 (nominal)	6.4	-0.014	1.58 x 10^5
SAE 10W 40	11.8	-0.018	4.17 x 10^5

For lubricants SAE 10W30 (nominal μ^*= 6.4 c-Poise), SAE 5W10 (μ = 1.4 c-Poise), and SAE 10W40 (μ = 11.8 c-Poise), Figure 36 shows the predicted total amplitude of shaft motion at the compressor nose versus rotor speed. The predicted results show that the total shaft motion amplitudes (0 to pk) for the TC-SFRB lubricated with SAE 10W40 are ~18 % smaller than those for the TC-SFRB lubricated with the nominal viscosity lubricant SAE 10W30. On the other hand, the total amplitudes of shaft motion for the TC-SFRB lubricated with the lighter lubricant SAE 5W10 are ~23 % larger than those for the TC-SFRB supplied with SAE 10W30 (nominal viscosity). These results show that the rotor SSV amplitudes increase with a decrease in lubricant viscosity (μ). However, there is a mandate to select low weight lubricants, such as SAE 5W10. A heavy lubricant aggravates environmental pollution due to NOx production [46].

For the TC-SFRB supplied with SAE 10W40 (μ = 11.8 c-Poise = 1.8 μ^*), Figure 37 shows a waterfall plot of the nonlinear transient response of the TC at the compressor nose and along the vertical direction. From 30 krpm (500 Hz) to 195 krpm (3,250 Hz), the prediction shows that rotor SSV motions occur at frequencies within 1/5~1/2 of shaft speed.

For lubricants SAE 10W30 (nominal), SAE 5W10, and SAE 10W40, Figure 38 shows the rotor SSV frequency content at the compressor nose versus rotor speed. The predictions also show that for low rotor speeds (~45 krpm), the rotor whirl frequencies are similar (~240 Hz to ~350 Hz) for the TC-SFRB supplied with either of the three lubricants. As the rotor speed increases, the subsynchronous frequencies for the TC-SFRB lubricated with the higher lubricant viscosity are higher in magnitude than those for the TC-SFRB

lubricated with the lower lubricant viscosity. Note that above a shaft speed of 195 krpm (3,250 Hz) the subsynchronous frequencies for the TC-SFRB lubricated with SAE 10W40 disappear while the subsynchronous frequencies for the TC-SFRB lubricated with the other two lubricant types persist. This is because as the rotor speed increases the subsynchronous motion amplitudes for the TC-SFRB lubricated with SAE 10W40 vanish. For the TC-SFRB supplied with SAE 10W40, the rotor deflected mode shapes show a conical mode at 244 Hz for a rotor speed of 30 krpm corresponding to the rotor mode shape of 1st FWM; and a cylindrical-bending mode at 791 Hz for a rotor speed of 195 krpm corresponding to the rotor mode shape of 2nd FWM, respectively, as seen in the inset graphs.

As the lubricant viscosity decreases ~88 %, from 11.8 c-Poise (SAE 10W40) to 1.4 c-Poise (SAE 5W10), the magnitude of the 1st FWM natural frequency decreases ~32 %, and the magnitude of the 2nd FWM natural frequency decreases ~11 %.

Figure 39 shows a comparison of the rotor motion amplitude, 0 to pk, for the TC-SFRB lubricated with SAE 5W10, SAE 10W30 (nominal), and SAE 10W40. The rotor subsynchronous response amplitudes (SSV) for the TC-SFRB supplied with SAE 5W10 are the largest, whereas the rotor subsynchronous response amplitudes for the TC-SFRB supplied with SAE 10W40 are the smallest. Note that for rotor speeds above 195 krpm (3,250 Hz), there are no rotor subsynchronous motion components for the TC-SFRB lubricated with SAE 10W40, as also shown in Figure 38. For either of the three lubricants supplied to the TC-SFRB system, the rotor synchronous response amplitudes (1X) are almost the same.

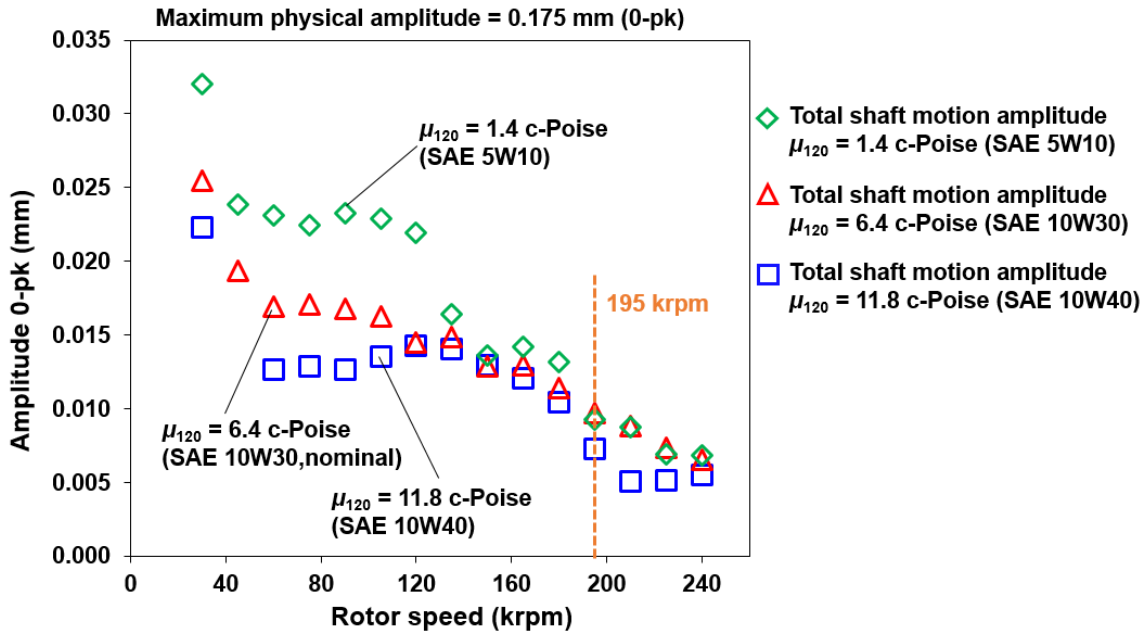**Figure 36. Amplitudes of total shaft motion versus shaft speed. Location; compressor nose, vertical plane. Predictions obtained for TC-SFRB supplied with SAE 5W10, SAE 10W30 (nominal), and SAE 10W40 lubricants.**
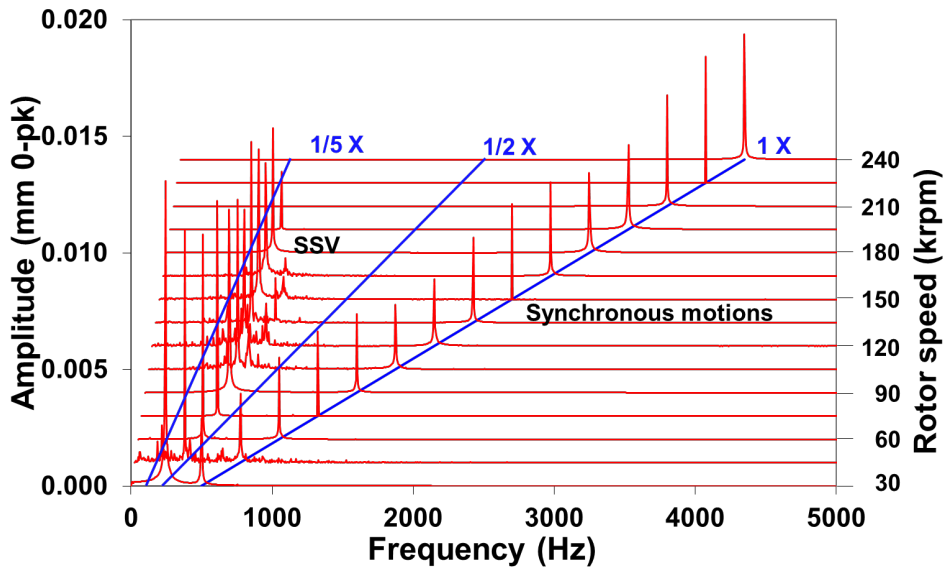
Figure 37. Waterfall plot of rotor nonlinear transient response at compressor nose, vertical plane. Rotor speed = 30 krpm to 240 krpm. Prediction obtained for a TC-SFRB supplied with SAE 10W40 lubricant.
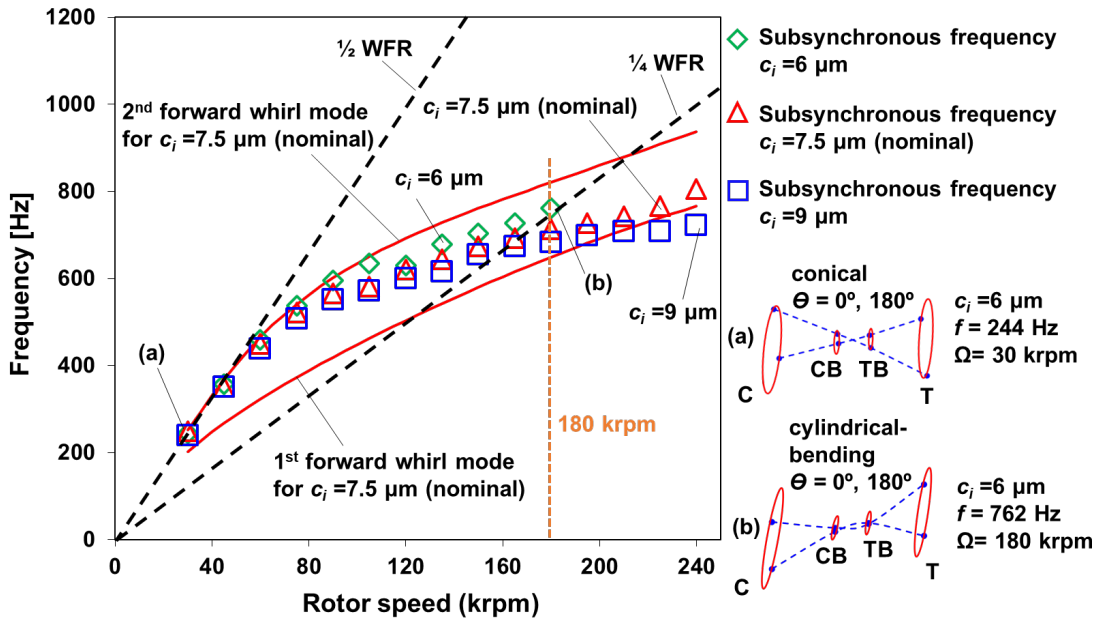
Figure 38. Rotor SSV frequencies versus shaft speed. Location; compressor nose, vertical plane. Predictions obtained for TC-SFRB supplied with SAE 5W10, SAE 10W30 (nominal), and SAE 10W40 lubricants. Insets show rotor deflected mode shapes.
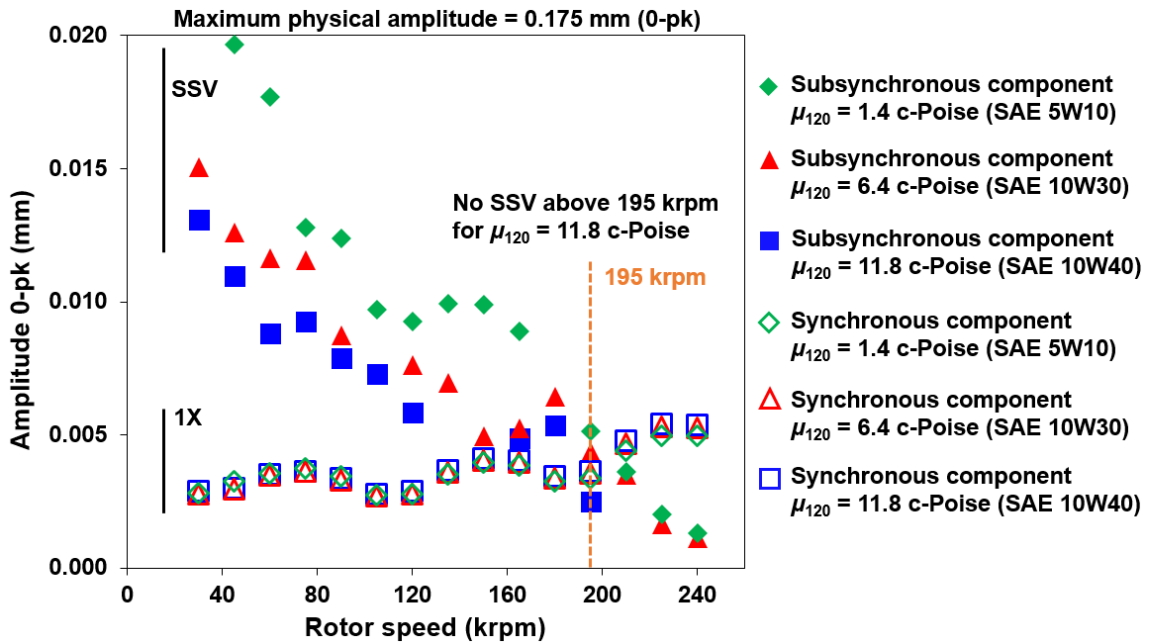
Figure 39. Amplitude components of rotor synchronous and subsynchronous motions (0 to pk) at compressor nose versus rotor speed. Comparison of rotor responses obtained for TC-SFRB supplied with SAE 5W10, SAE 10W30 (nominal), and SAE 10W40 lubricants.

Effect of bearing inner film length and diameter on rotordynamic response

Engineers select a low bearing inner film area ($A_i = \pi$ x D_i x L_i) as it produces less viscous drag power losses. Hence, the analysis investigates the influence of the bearing inner film length (L_i) and diameter (D_i) on the rotordynamic motions of a TC. The analysis assumes the same bearing inner film length and diameter on both the TB and the CB.

For a SFRB with L_i*= 4.3 mm (nominal length), 3 mm (30% shorter than L_i*), and 5.6 mm (30% longer than L_i*), Figure 40 shows the predicted total amplitude of shaft motion at the compressor nose versus rotor speed. The predictions show that the total shaft motion amplitude (0 to pk) for the TC-SFRB with L_i =3 mm are ~19 % larger than the total shaft motion amplitude for the SFRB TC system with the nominal L_i*=4.3 mm. On the other hand, the total shaft motion amplitude for the SFRB TC system with L_i =5.6 mm are ~30 % smaller than the total shaft motion amplitude for the TC-SFRB with the nominal L_i*=4.3 mm. These results show that the rotor SSV amplitude increases with a decrease in the bearing inner film length (L_i). Note that increasing L_i leads to an increase of drag power losses and less heat conducted by the inner film into the ring.

For the TC-SFRB with L_i = 5.6 mm (30% longer than L_i*), Figure 41 shows a waterfall plot of the nonlinear transient response of the TC at the compressor nose and along the vertical direction. From 30 krpm (500 Hz) to 135 krpm (2,250 Hz), the prediction shows that rotor SSV motions occur at frequencies within 1/5~1/2 of shaft speed.

For the TC-SFRB with L_i*= 4.3 mm, 3 mm, and 5.6 mm, Figure 42 shows the predicted rotor SSV frequency content at the compressor nose versus rotor speed. The predicted results show that for low rotor speeds (~45 krpm), the rotor whirl frequencies are similar

86

(~240 Hz to ~350 Hz) for the TC-SFRB with any of the three inner film lengths. However, as the rotor speed increases the subsynchronous frequencies for the TC-SFRB with a longer L_i are higher than the subsynchronous frequencies for the TC-SFRB with a shorter L_i. Note that above a shaft speed of 135 krpm (2,250 Hz) the subsynchronous frequencies for the TC-SFRB with L_i =5.6 mm disappear while the subsynchronous frequencies for the TC-SFRB with the other inner film lengths persist. This is because as the rotor speed increases (> 135 krpm), the SSV amplitudes for the TC-SFRB with L_i =5.6 mm vanish.

For the TC-SFRB with L_i =5.6 mm, the rotor deflected mode shapes show a conical mode at 239 Hz for a rotor speed of 30 krpm corresponding to the rotor mode shape of 1st FWM; and a cylindrical-bending mode at 684 Hz for a rotor speed of 135 krpm corresponding to the rotor mode shape of 2nd FWM, respectively, as seen in the inset graphs. Note that each L_i determines natural frequencies and mode shapes of the rotor-bearing system. As L_i decreases ~46 %, from 5.6 mm to 3 mm, the magnitude of the 1st FWM natural frequency decreases ~29 %, and the magnitude of the 2nd FWM natural frequency decreases ~5 %.

Figure 43 shows a comparison of the rotor motion amplitude, 0 to pk, for the TC-SFRB with the nominal L_i*=4.3 mm versus the rotor motion amplitude for the TC-SFRB with L_i =3 mm and L_i =5.6 mm. The rotor subsynchronous response amplitudes (SSV) for the TC-SFRB with L_i =3 mm are the largest while the rotor subsynchronous response amplitudes for the TC-SFRB with L_i =5.6 mm are the smallest. Note that there are no subsynchronous motions for the TC-SFRB with L_i =5.6 mm at rotor speeds above 135 krpm (2,250 Hz), as shown in Figure 42. Note also that as the rotor speed increases, the

rotor synchronous motion amplitudes (1X) for the TC-SFRB with L_i =5.6 mm are slightly

larger than the rotor synchronous motion amplitudes for the TC-SFRB with the other inner

film lengths.

Figure 40. Amplitudes of total shaft motion versus shaft speed. Location; compressor nose, vertical plane. Predictions obtained for SFRB inner film length L_i = 4.3 mm (± 1.3 mm). Other dimensions as in Table 1.

Figure 41. Waterfall plot of rotor nonlinear transient response at compressor nose, vertical plane. Rotor speed = 30 krpm to 240 krpm. Prediction obtained for a SFRB with inner film length L_i = 5.6 mm. Other dimensions as in Table 1.

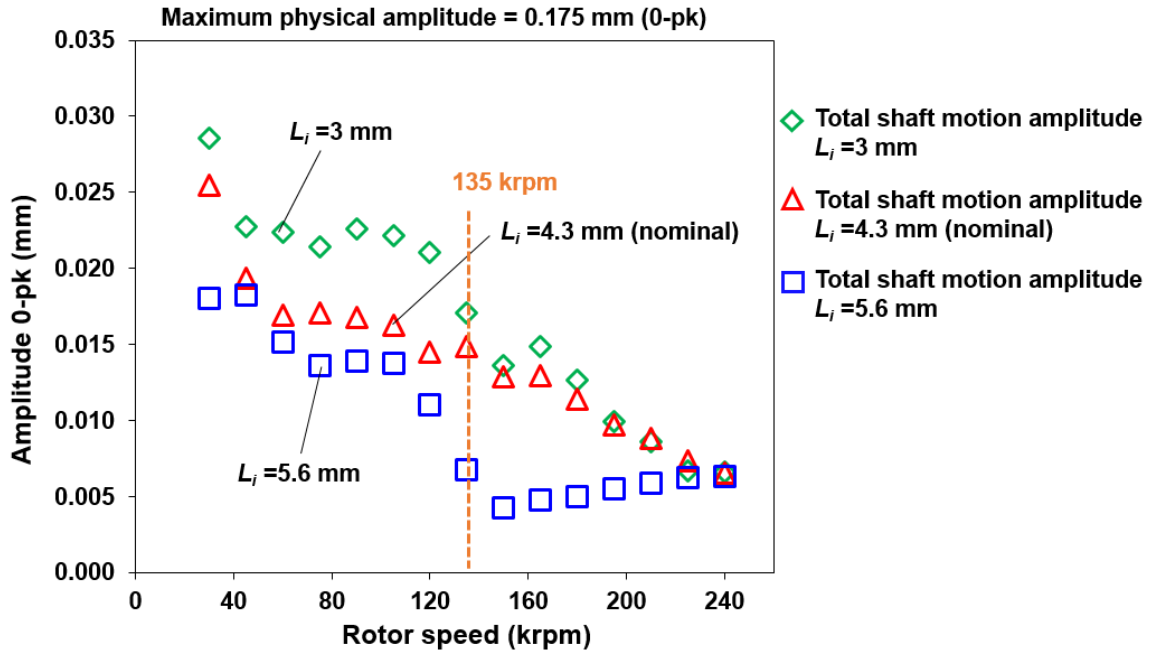**Figure 42. Rotor SSV frequencies versus shaft speed. Location; compressor nose, vertical plane. Predictions obtained for SFRB inner film length L_i = 4.3 mm (± 1.3 mm). Other dimensions as in Table 1. Insets show rotor deflected mode shapes.**
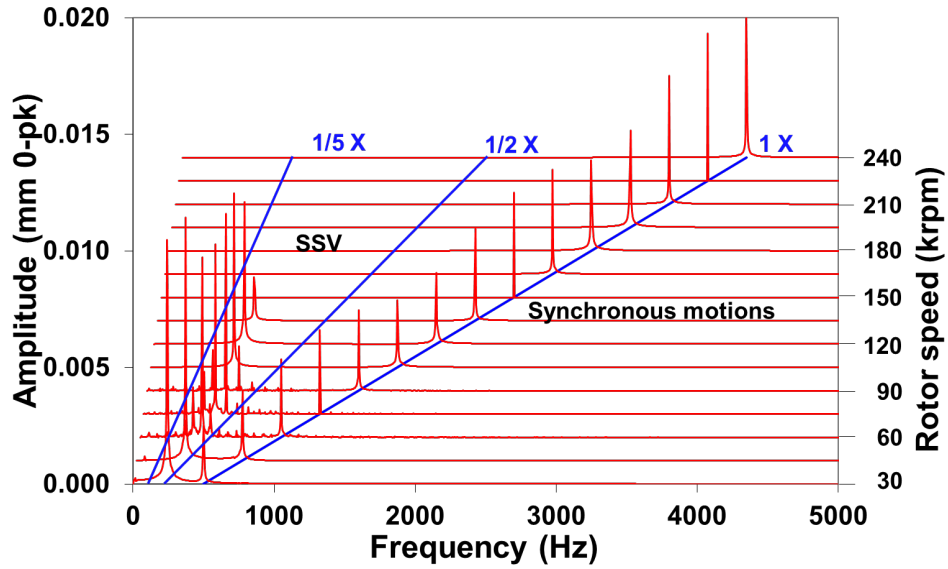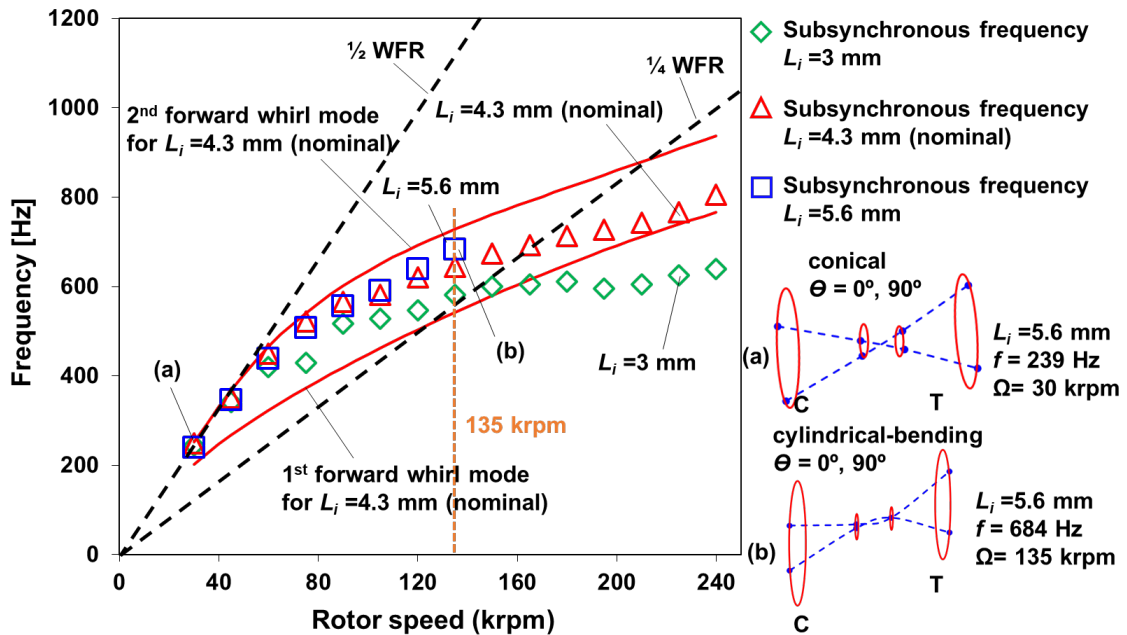
89
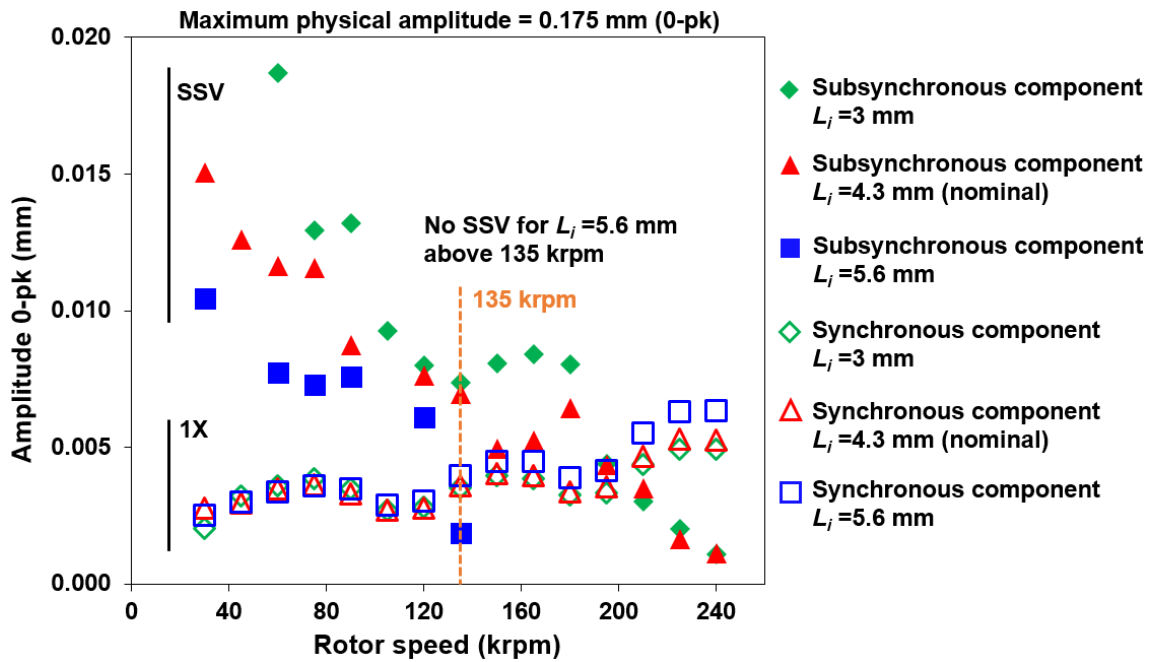
Figure 43. Amplitude components of rotor synchronous and subsynchronous motions (0 to pk) at compressor nose versus rotor speed. Comparison of rotor responses obtained for SFRB inner film length L_i = 4.3 mm (± 1.3 mm). Other dimensions as in Table 1.

For a SFRB with D_i*= 6 mm (nominal), 4 mm (33% thinner than D_i*), and 8 mm (33% thicker than D_i*), Figure 44 shows the predicted total amplitude of shaft motion at the compressor nose versus rotor speed. The results show that the total shaft motion amplitudes (0 to pk) for the TC-SFRB with D_i =4 mm are ~22 % larger than the total shaft motion amplitudes for the TC-SFRB with the nominal D_i*=6 mm. On the other hand, the total shaft motion amplitudes for the TC-SFRB with D_i =8 mm are ~18 % smaller than the total shaft motion amplitudes for the TC-SFRB with the nominal D_i*=6 mm. These results evidence that the rotor SSV amplitudes increase with a decrease of the bearing inner diameter (D_i), as it makes the rotor more flexible.

90

For the TC-SFRB with D_i =8 mm (33% thicker than D_i*), Figure 45 shows a waterfall plot of the nonlinear transient response of the TC at the compressor nose and along the vertical direction. From 30 krpm (500 Hz) to 195 krpm (3,250 Hz), the prediction shows that rotor SSV motions occur at frequencies within 1/5~1/2 of shaft speed.

For the TC-SFRB with D_i*= 6 mm, 4 mm, and 8 mm, Figure 46 shows the predicted rotor SSV frequency content at the compressor nose versus rotor speed. The predicted results also show that as the rotor speed increases the rotor subsynchronous frequencies for the TC-SFRB with the larger D_i are higher than the rotor subsynchronous frequencies for the TC-SFRB with the smaller D_i. For low rotor speeds (~45 krpm), the rotor whirl frequencies are similar (~240 Hz to ~350 Hz) for the TC-SFRB with any of the three inner film diameters. Note that above a shaft speed of 195 krpm (3,250 Hz) the rotor subsynchronous frequencies for the TC-SFRB with D_i =8 mm disappear while the rotor subsynchronous frequencies for the TC-SFRB with other inner diameters persist. This is because as the rotor speed increases the SSV amplitudes for the TC-SFRB with D_i =8 mm vanish. For the TC-SFRB with D_i =8 mm, the rotor deflected mode shapes show a conical mode at 244 Hz for a rotor speed of 30 krpm corresponding to the rotor mode shape of 1st FWM; and a cylindrical-bending mode at 786 Hz for a rotor speed of 195 krpm corresponding to the rotor mode shape of 2nd FWM, respectively, as seen in the inset graphs. Note that each D_i determines natural frequencies and mode shapes of the rotor-bearing system. As D_i decreases ~50 %, from 8 mm to 4 mm, the magnitude of the 1st FWM natural frequency decreases ~32 %, and the magnitude of the 2nd FWM natural frequency decreases ~9 %.

Figure 44. Amplitudes of total shaft motion versus shaft speed. Location; compressor nose, vertical plane. Predictions obtained for SFRB inner film diameter D_i = 6 mm (± 2 mm). Other dimensions as in Table 1.

Figure 45. Waterfall plot of rotor nonlinear transient response at compressor nose, vertical plane. Rotor speed = 30 krpm to 240 krpm. Prediction obtained for a SFRB with inner film diameter D_i = 8 mm. Other dimensions as in Table 1.
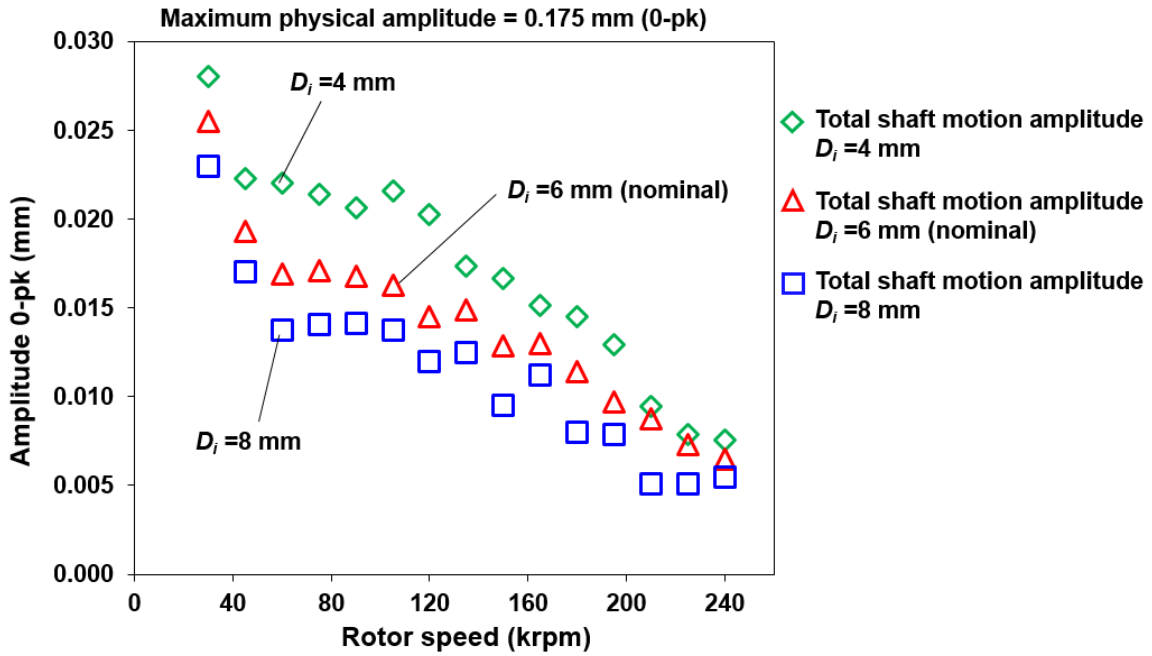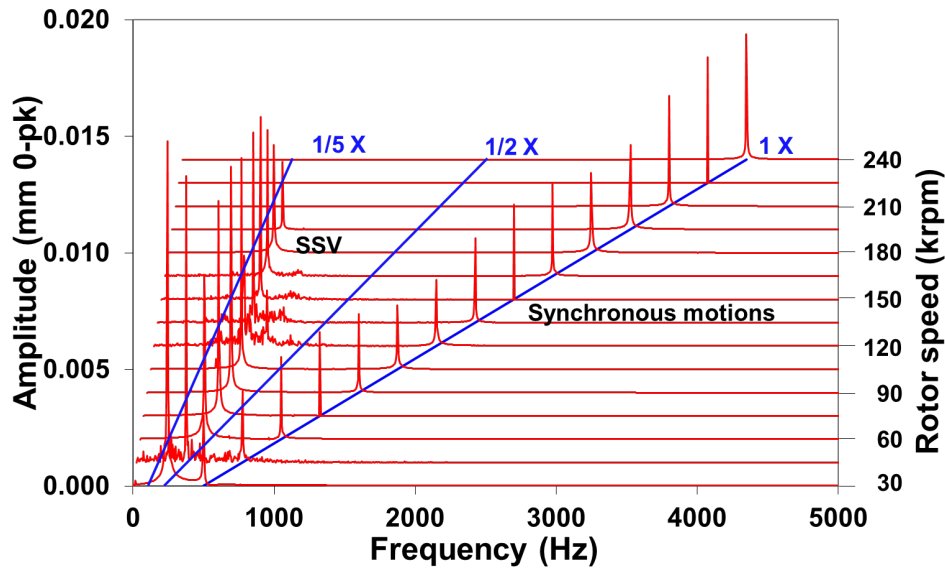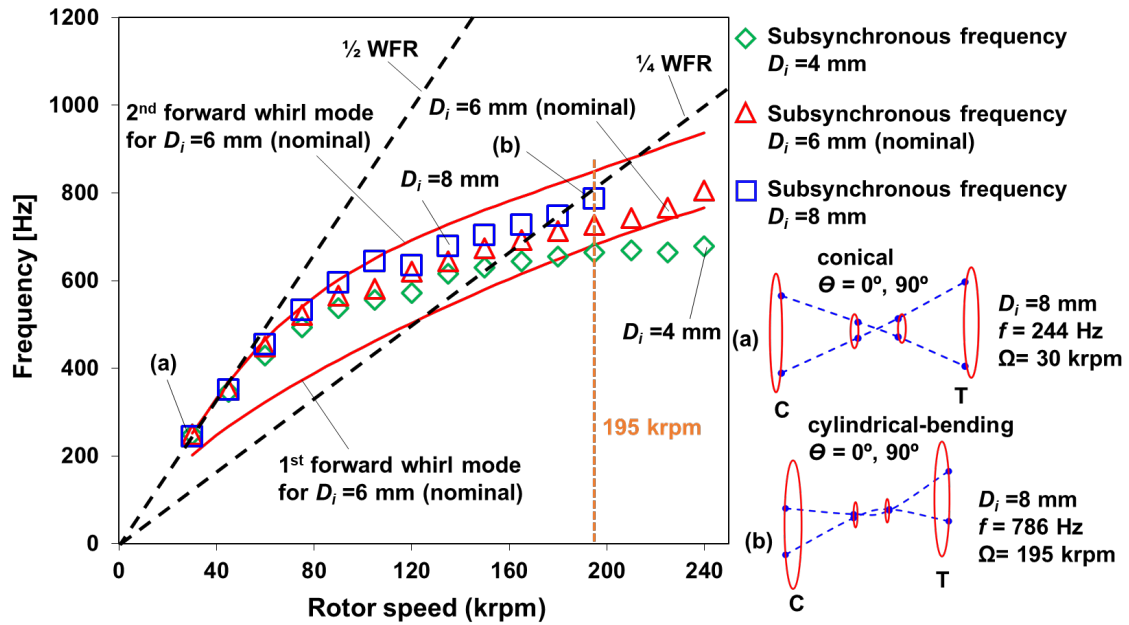
Figure 46. Rotor SSV frequencies versus shaft speed. Location; compressor nose, vertical plane. Predictions obtained for SFRB inner film diameter D_i = 6 mm (± 2 mm). Other dimensions as in Table 1. Insets show rotor deflected mode shapes.

Influence of mass imbalance distribution on TC-SFRB rotordynamic response
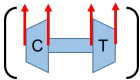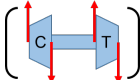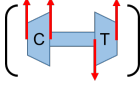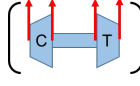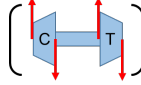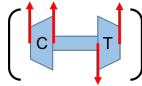
The nominal mass imbalances are applied to the front and back planes of the compressor and the turbine wheels ($\varphi_1 \sim \varphi_4 = 0°$, respectively) with all-in-phase angles. In the following analysis, the phase angles differ but the same amounts of mass imbalances are kept. Recall the imbalance state in Table 3 corresponds to an ISO 1940 G100 for the rotor-SFRB system.

Figure 47 shows the predicted TC total amplitude of shaft motion (0-pk) and frequency of the SSV motions at the compressor nose versus rotor speed. The predicted results show that the total shaft motion amplitudes for the TC-SFRB with imbalances located at $\varphi_1 = \varphi_3 = 0°$ and $\varphi_2 = \varphi_4 = 180°$ are ~26 % smaller than the total shaft motion

amplitudes for the TC-SFRB with imbalances located at $\varphi_{i=1,4}=0°$. Likewise, the total shaft motion amplitudes for the TC-SFRB with imbalances located at $\varphi_1=\varphi_2=\varphi_4=0°$ and $\varphi_3=180°$ are ~15 % smaller than the total shaft motion amplitudes for the TC-SFRB with imbalances located at $\varphi_{i=1,4}=0°$. Moreover, above a rotor speed of 150 krpm (2,500 Hz), the total shaft motion amplitudes for the TC-SFRB with imbalances located at $\varphi_1=\varphi_3=0°$ and $\varphi_2=\varphi_4=180°$ are ~57 % smaller than the total shaft motion amplitudes for the TC-SFRB with imbalances located at $\varphi_{i=1,4}=0°$. Above a rotor speed of 150 krpm (2,500 Hz), the total shaft motion amplitudes for the TC-SFRB with imbalances located at $\varphi_1=\varphi_2=\varphi_4=0°$ and $\varphi_3=180°$ are ~31 % smaller than the total shaft motion amplitudes for the TC-SFRB with imbalances located at $\varphi_{i=1,4}=0°$.
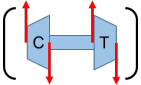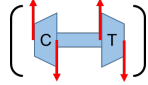
For the TC-SFRB with imbalances located at $\varphi_1=\varphi_3=0°$ and $\varphi_2=\varphi_4=180°$, Figure 48 shows a waterfall plot of the nonlinear transient response of the TC at the compressor nose and along the vertical direction. From 30 krpm (500 Hz) to 210 krpm (3,500 Hz), the prediction shows that rotor SSV motions occur at frequencies within 1/5~1/2 of shaft speed.

Figure 49 shows the predicted frequency of the rotor SSV motions at the compressor nose versus rotor speed. Below a rotor speed of 210 krpm (3,500 Hz), the rotor subsynchronous frequencies are almost the same (~240 Hz to ~750 Hz) for the TC-SFRB with either of the three phase angle combinations. For the TC-SFRB with imbalances located at $\varphi_1=\varphi_3=0°$ and $\varphi_2=\varphi_4=180°$ the rotor deflected mode shapes show a conical mode at 239 Hz for a rotor speed of 30 krpm corresponding to the rotor mode shape of 1st FWM; and a cylindrical-bending mode at 742 Hz for a rotor speed of 210

krpm corresponding to the rotor mode shape of 2nd FWM, respectively, as seen in the inset

graphs. Note that the rotor subsynchronous frequencies for the TC-SFRB with imbalances

located at $\varphi_1=\varphi_3=0°$ and $\varphi_2=\varphi_4=180°$ [diagram] and the rotor subsynchronous

frequencies for the TC-SFRB with imbalances located at $\varphi_1=\varphi_2=\varphi_4=0°$ and $\varphi_3=180°$

[diagram] disappear for rotor speed above 210 krpm (3,500 Hz).
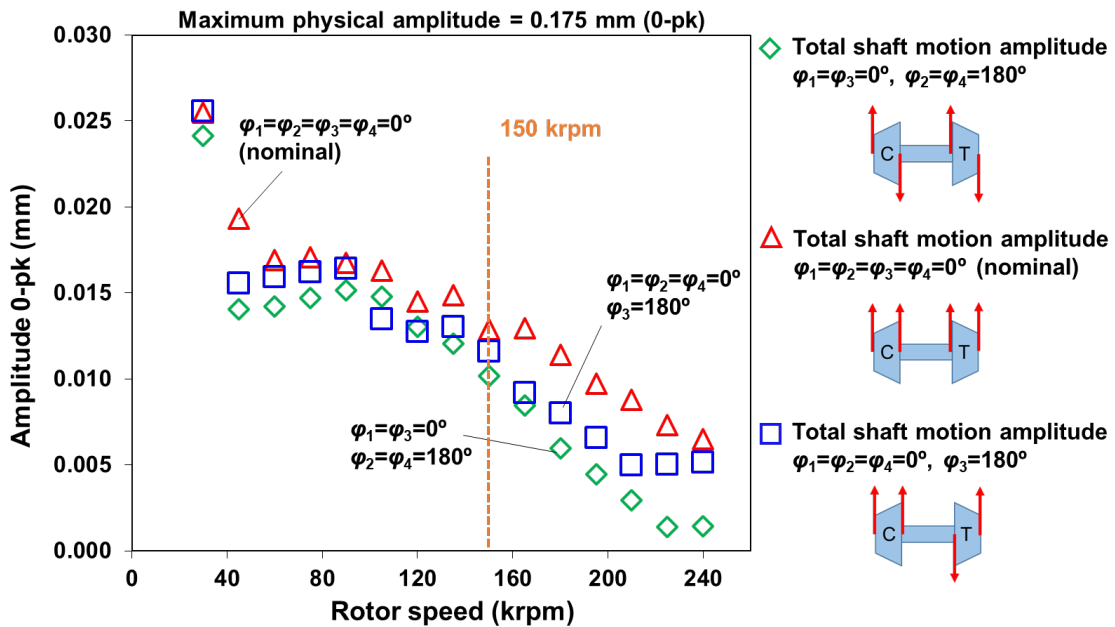
Figure 47. Amplitudes of total shaft motion versus shaft speed. Location; compressor nose, vertical plane. Comparison of rotor responses obtained for nominal mass imbalance distribution ($\varphi_1=\varphi_2=\varphi_3=\varphi_4=0°$) and others with different phase angles; ($\varphi_1=\varphi_3=0°$, $\varphi_2=\varphi_4=180°$), ($\varphi_1=\varphi_2=\varphi_4=0°$, $\varphi_3=180°$). Insets show imbalance distributions in graphical form.
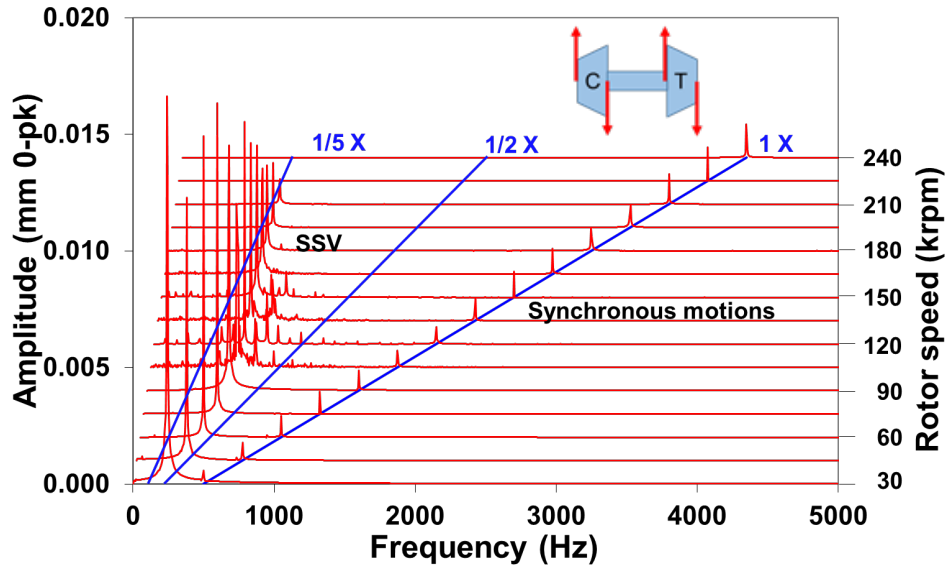
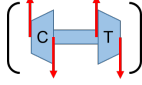**Figure 48. Waterfall plot of rotor nonlinear transient response at compressor nose, vertical plane. Rotor speed = 30 krpm to 240 krpm. Prediction obtained for a TC-SFRB with imbalances located at $\varphi_1=\varphi_3=0°$ and $\varphi_2=\varphi_4=180°$.**
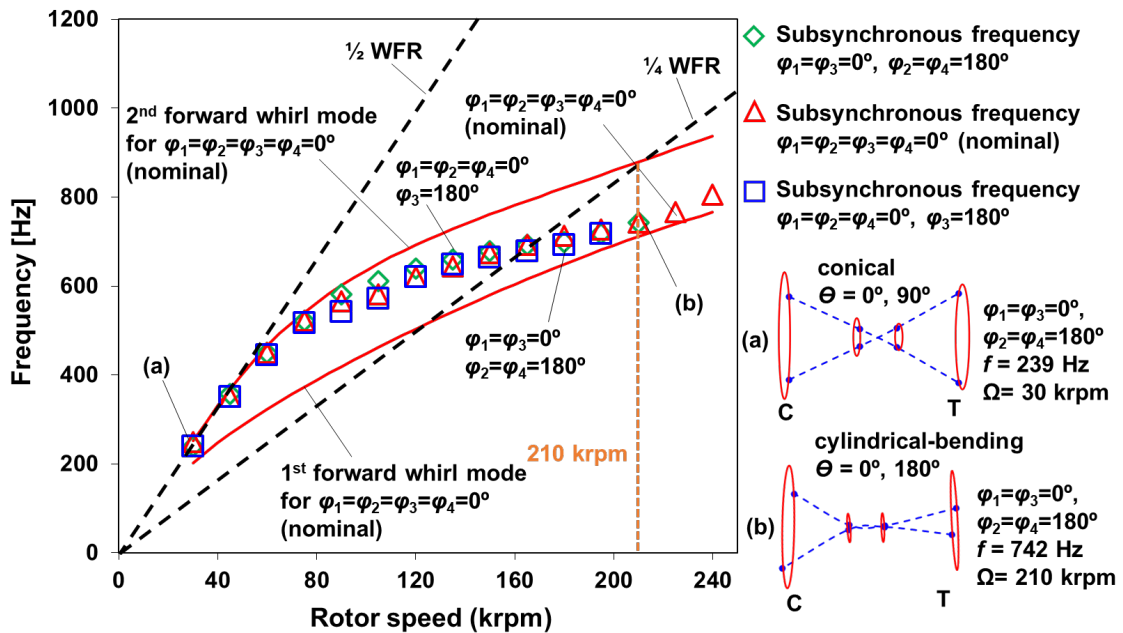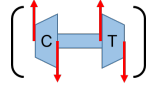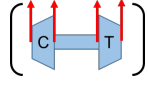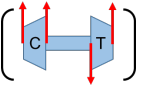
Figure 49. Rotor SSV frequencies versus shaft speed. Location; compressor nose, vertical plane. Comparison of rotor responses obtained for nominal mass imbalance distribution ($\varphi_1=\varphi_2=\varphi_3=\varphi_4=0°$) and others with different phase angles; ($\varphi_1=\varphi_3=0°$, $\varphi_2=\varphi_4=180°$), ($\varphi_1=\varphi_2=\varphi_4=0°$, $\varphi_3=180°$). Insets show rotor deflected mode shapes.

Figure 50 shows predicted rotor synchronous (1X) and subsynchronous (SSV) motion amplitude components for the TC-SFRB with the nominal imbalance distribution and others with distinct phase angles. Note that the rotor synchronous motion amplitudes for the TC-SFRB with imbalances located at $\varphi_1=\varphi_3=0^o$ and $\varphi_2=\varphi_4=180^o$ are ~73 % smaller than the rotor synchronous motion amplitudes for t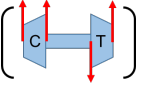he TC-SFRB with imbalances located at $\varphi_{i=1,4}=0^o$. The rotor subsynchronous motion amplitudes for the TC-SFRB with imbalances located at $\varphi_1=\varphi_3=0^o$ and $\varphi_2=\varphi_4=180^o$ and the rotor subsynchronous motion amplitudes for the TC-SFRB with imbalances located at $\varphi_1=\varphi_2=\varphi_4=0^o$ and $\varphi_3=180^o$ disappear for a rotor speed above 210 krpm (3,500 Hz), as shown in Figure 49.
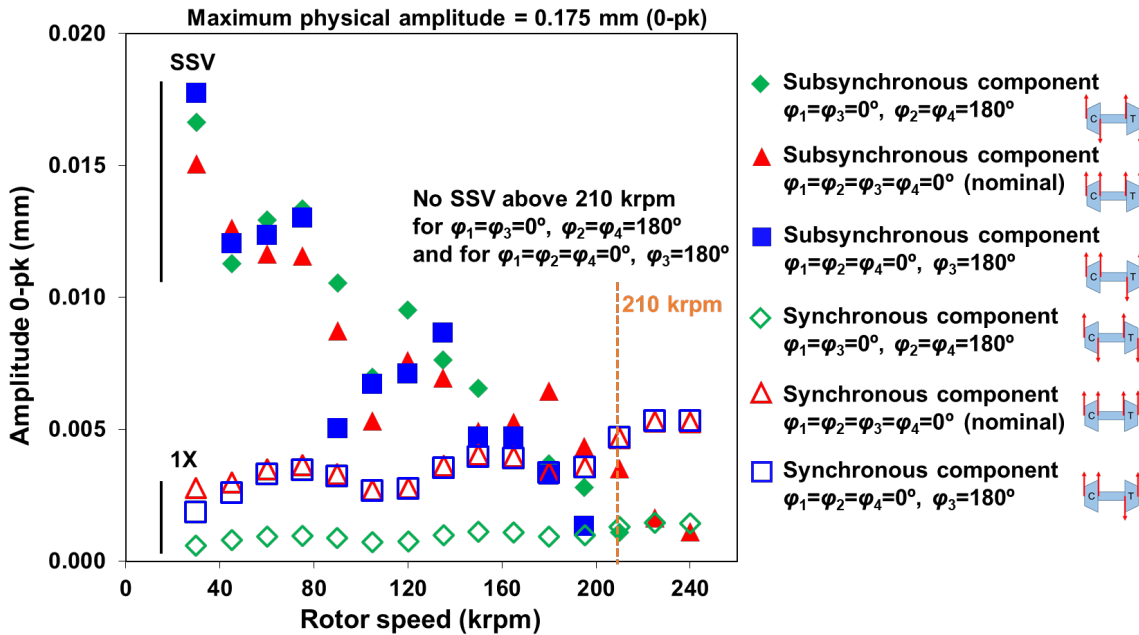
Figure 50. Amplitude components of rotor synchronous and subsynchronous motions (0 to pk) at compressor nose versus rotor speed. Comparison of rotor responses obtained for nominal mass imbalance distribution ($\varphi_1=\varphi_2=\varphi_3=\varphi_4=0^o$) and others with different phase angles; ($\varphi_1=\varphi_3=0^o$, $\varphi_2=\varphi_4=180^o$), ($\varphi_1=\varphi_2=\varphi_4=0^o$, $\varphi_3=180^o$). Insets show imbalance distributions in graphical form.

Influence of mass imbalance amount on TC-SFRB rotordynamic response

For half and twice the amount of nominal mass imbalance shown in Table 3, Figure 51 shows the predicted TC total amplitude of shaft motion (0-peak) at the compressor nose versus rotor speed. The predicted results show that the differences of the total shaft motion amplitudes (0-pk) between the mass imbalances are less than ~10 %.

For the TC-SFRB with twice the amount of nominal mass imbalance, Figure 52 shows a waterfall plot of the nonlinear transient response of the TC at the compressor nose and along the vertical direction. From 30 krpm (500 Hz) to 180 krpm (3,000 Hz), the prediction shows that rotor SSV motions occur at frequencies within 1/5~1/2 of shaft speed.

For half and twice the amount of nominal mass imbalance, Figure 53 shows the predicted frequencies of the rotor SSV motions at the compressor nose versus rotor speed. The predictions show that as the rotor speed increases the rotor subsynchronous frequencies for the TC-SFRB with the smaller amount of the mass imbalance are higher than the rotor subsynchronous frequencies for the TC-SFRB with the larger amount of the mass imbalance. For low rotor speeds (~60 krpm), the rotor whirl frequencies are similar (~240 Hz to ~450 Hz) for the TC-SFRB with any of the three mass imbalance amounts. Note that above a shaft speed of 180 krpm (3,000 Hz), the rotor subsynchronous frequencies for the TC-SFRB with twice amount of the nominal mass imbalance distribution disappear while the rotor subsynchronous frequencies for the TC-SFRB with the smaller amount of mass imbalances persist. This is likely because, for the TC-SFRB with twice amount of the nominal mass imbalance and as the rotor speed increases, the amplitude of synchronous motion increases while suppressing the motions at

subsynchronous frequencies. For the TC-SFRB with twice the amount of nominal mass imbalance, the rotor deflected mode shapes show a conical mode at 249 Hz for a rotor speed of 30 krpm corresponding to the rotor mode shape of 1st FWM; and a cylindrical-bending mode at 679 Hz for a rotor speed of 180 krpm corresponding to the rotor mode shape of 2nd FWM, respectively, as seen in the inset graphs.
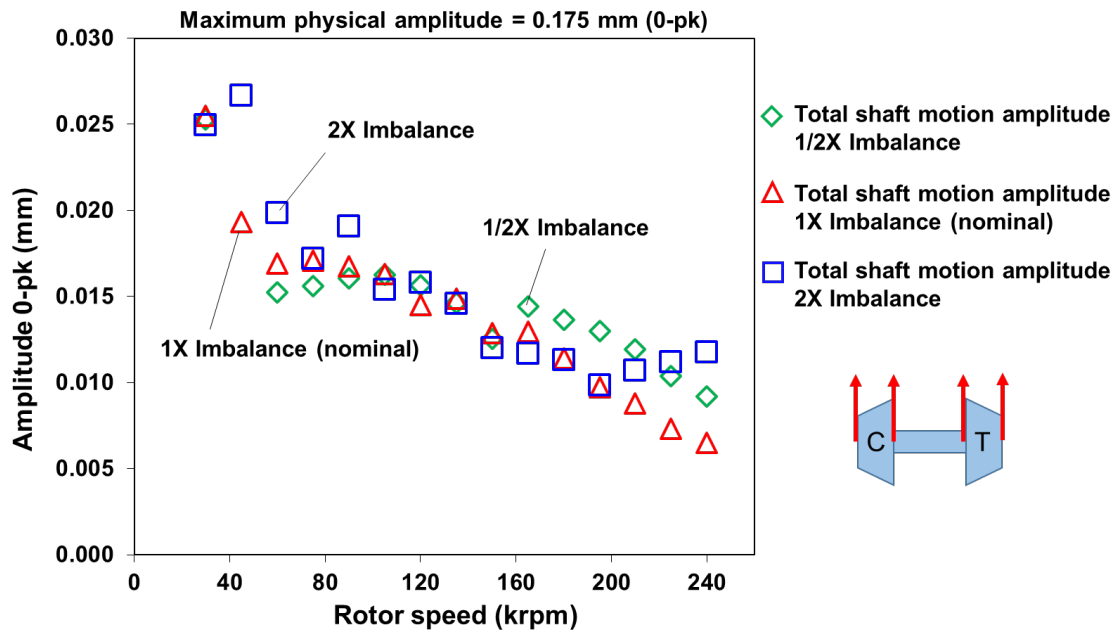
Figure 51. Amplitudes of total shaft motion versus shaft speed. Location; compressor nose, vertical plane. Comparison of rotor responses obtained from nominal mass imbalance with half and twice nominal. ($\varphi_1=\varphi_2=\varphi_3=\varphi_4=90^o$).

99
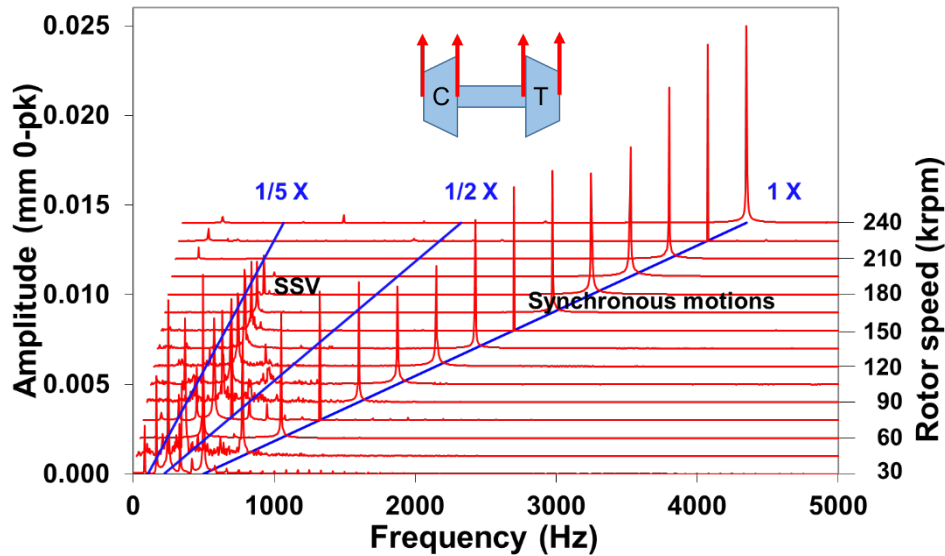
Figure 52. Waterfall plot of rotor nonlinear transient response at compressor nose, vertical plane. Rotor speed = 30 krpm to 240 krpm. Prediction obtained for a TC-SFRB with twice nominal mass imbalance. ($\varphi_1=\varphi_2=\varphi_3=\varphi_4=90º$).
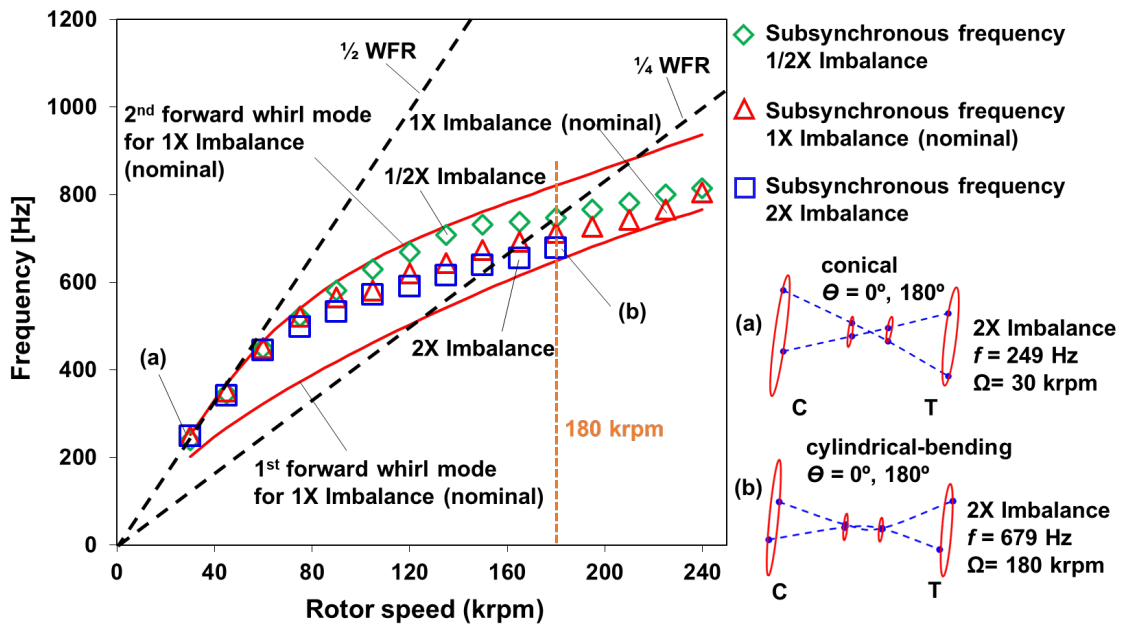
Figure 53. Rotor SSV frequencies versus shaft speed. Location; compressor nose, vertical plane. Comparison of rotor responses obtained from nominal mass imbalance with half and twice nominal. ($\varphi_1=\varphi_2=\varphi_3=\varphi_4=90º$). Insets show rotor deflected mode shapes.

100

Figure 54 shows predicted amplitude components of rotor synchronous (1X) and subsynchronous (SSV) motions obtained for the nominal, half, and twice amount of the mass imbalance distributions. The rotor synchronous motion amplitudes for the TC-SFRB with twice the amount of nominal mass imbalance are ~twice larger than the rotor synchronous motion amplitudes for the TC-SFRB with nominal mass imbalance. Likewise, the rotor synchronous motion amplitudes for the TC-SFRB with half the amount of nominal mass imbalance are ~half smaller than the rotor synchronous motion amplitudes obtained for the TC-SFRB with a nominal mass imbalance.

On the other hand, the rotor subsynchronous motion amplitudes (SSV) for the TC-SFRB with twice the amount of nominal mass imbalance are ~37 % smaller than the rotor subsynchronous motion amplitudes for the TC-SFRB with nominal mass imbalance. The rotor subsynchronous motion amplitudes for the TC-SFRB with half the amount of nominal mass imbalance are ~39 % larger than the rotor subsynchronous motion amplitudes for the TC-SFRB with a nominal mass imbalance.
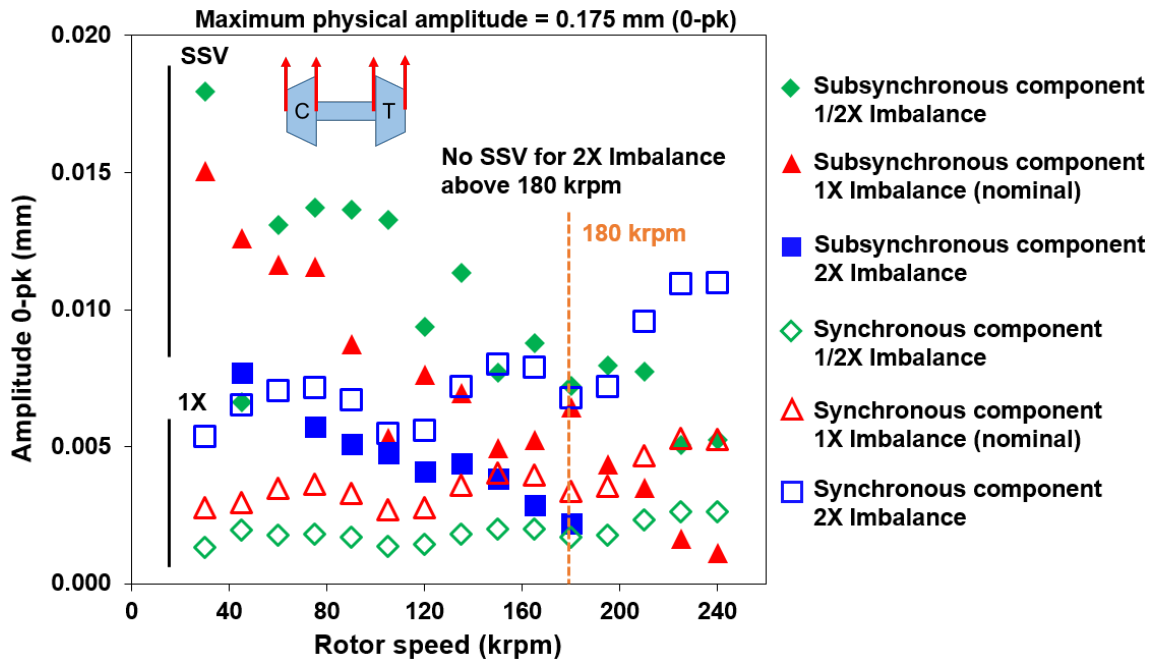
Figure 54. Amplitude components of rotor synchronous and subsynchronous motions (0 to pk) at compressor nose versus rotor speed. Comparison of rotor responses obtained from nominal mass imbalance with half and twice nominal. ($\varphi_1=\varphi_2=\varphi_3=\varphi_4=90^\circ$).

Assessment of current model predictions compared to published literature

Based on the analysis of the predictions for one TC-SFRB system discussed in this dissertation, the rotor SSV amplitudes decrease when the SFRB is supplied with a large lubricant viscosity (μ), and constructed to have a small inner film clearance (c_i), a long bearing inner film length (L_i) and a thick shaft diameter (D_i). Note that the nonlinear bearing reaction forces ($F_B = f(\mu, L_i, D_i/c_i)$) increase as the parameters above increase.

To support the findings above, Smolík et al. [47] investigate the influence of radial bearing clearance on the rotordynamic response of a TC rotor supported on floating ring bearings. For rotor speeds of 20 krpm to 180 krpm, the simulation results show the rotor SSV amplitudes decrease with a decrease in the bearings' inner film clearance. Gjika and San Andrés [48] performed measurements and predictions of the nonlinear rotordyanmics responses for a TC rotor supported on SFRBs. In Fig. 55, the results show that the TC-SFRB system with the largest inner film clearance presents the largest rotor SSV amplitudes.

In the current analysis, the predicted results show that the rotor SSV amplitudes for TC-SFRB system with a SFRB having the largest inner film clearance (c_i =9 μm) are ~56% larger than the rotor SSV amplitudes for a TC-SFRB system with a smaller inner film clearance (c_i =6 μm). Note that decreasing the inner film clearance demands of less flow while increasing the shear drag power losses.
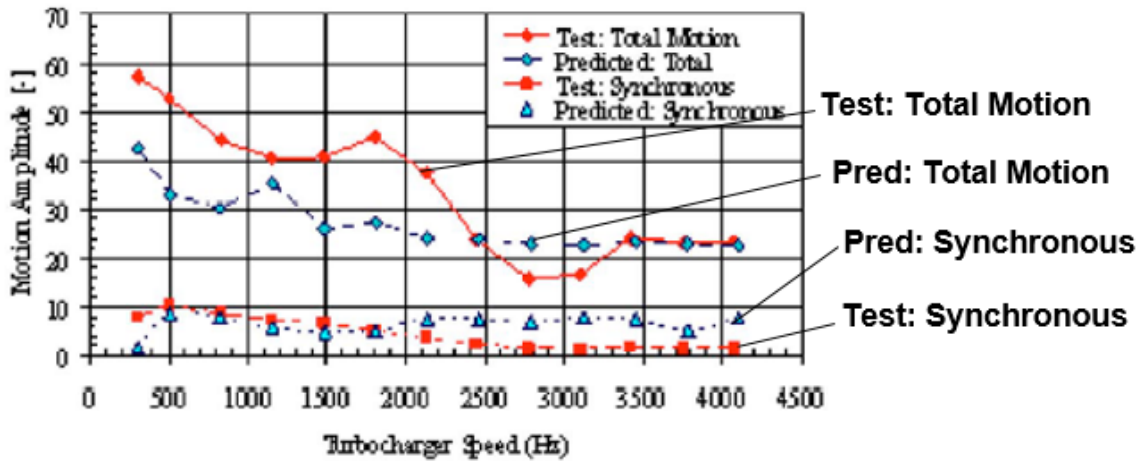
(a) Amplitude of SSV for rotor-bearing system with inner film of large c_i
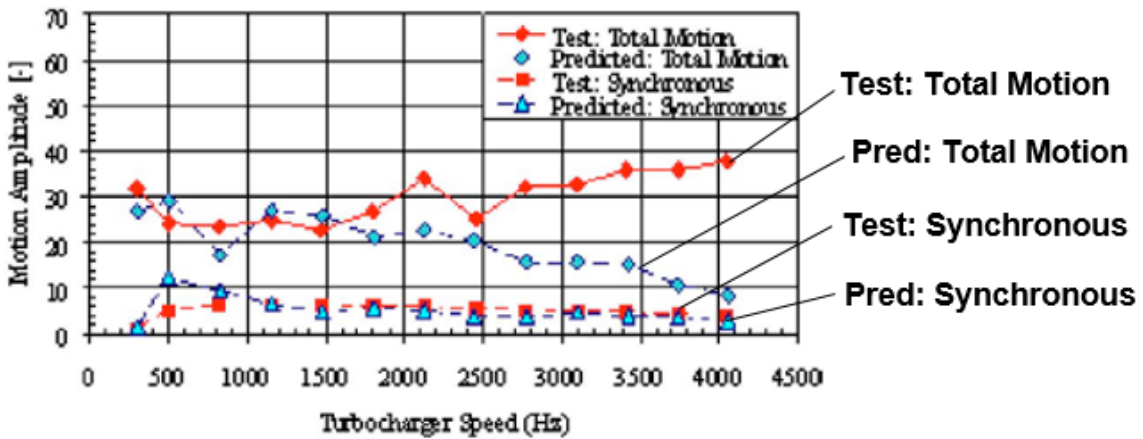
(b) Amplitude of SSV for rotor-bearing system with inner film of small c_i

Figure 55. Amplitude of total shaft motion and rotor synchronous (1X) motion versus shaft speed taken from Ref. [48]. Comparison of rotor responses obtained with two inner film clearances. Oil inlet at 150 ºC and 4 bar supply pressure.

Mutra [49] studies the influence of physical parameters such as the bearing clearance and the oil viscosity on the response of a TC rotor supported on fully floating ring bearings. In Fig. 56, the predictions show that the SSV amplitudes decrease with a decrease in the FRB inner film clearance (c_i) and also with an increase in the lubricant viscosity (μ). In the current analysis, the rotor SSV amplitudes for a TC-SFRB system supplied with a

104

small viscosity lubricant (μ =1.4 c-Poise) are ~50% larger than the rotor SSV amplitudes for the TC-SFRB system supplied with a larger lubricant viscosity (μ =11.8 c-Poise). However, increasing lubricant viscosity leads to a lesser lubricant flow and thus increases the drag power losses and heat in the film. Moreover, a TC supplied with a heavy lubricant can generate NOx productions due to a reaction between the oil and atmospheric nitrogen by the *hot* exhaust gas that could exceed acceptable emission standards for PVs [46].

(a) RBS with inner film of c_i =200 μm (b) RBS with lubricant μ=1.46 c-Poise

(c) RBS with inner film of c_i =500 μm (d) RBS with lubricant μ=9.10 c-Poise
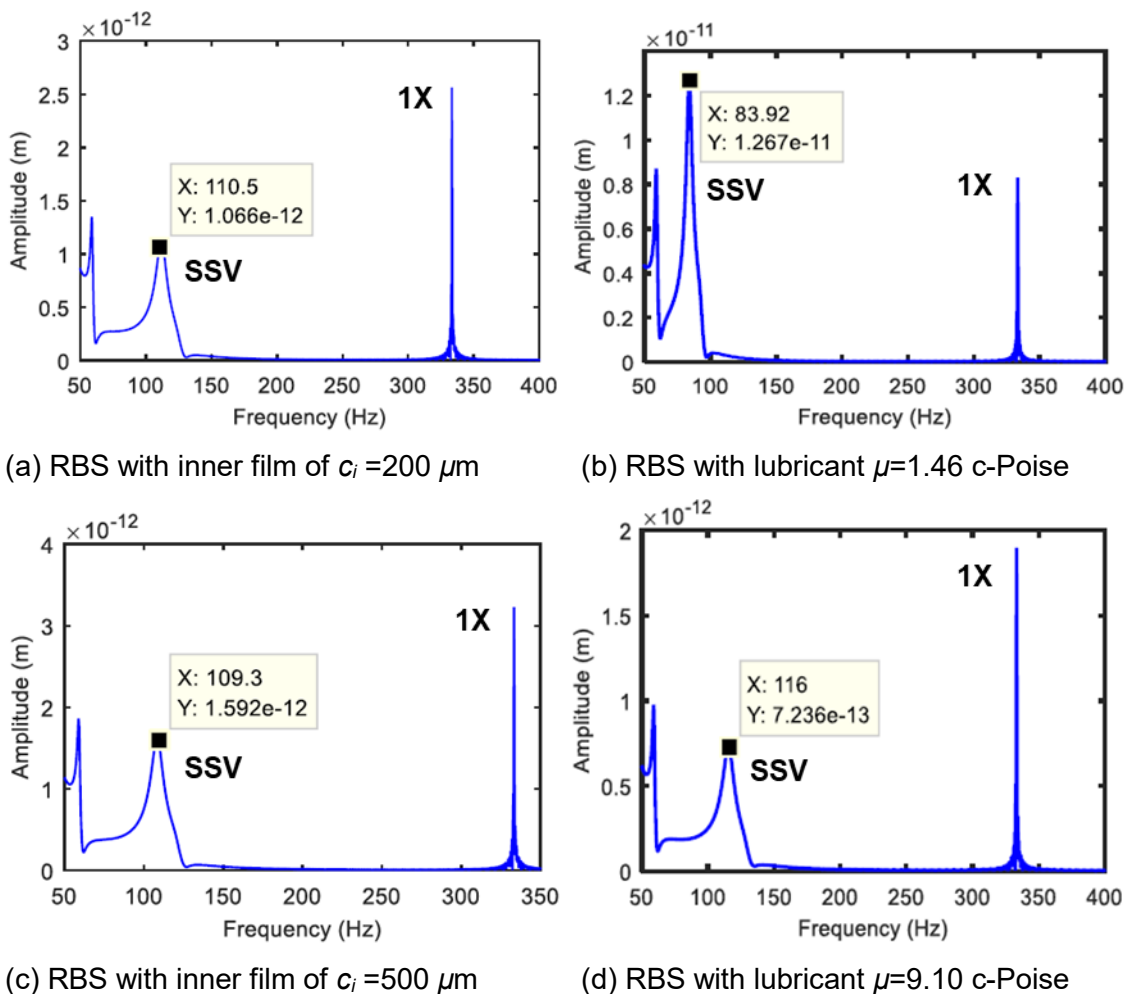
Figure 56. Fast Fourier Transform amplitude components of shaft motion versus frequency. Taken from Ref. [49]. Comparison of rotor responses obtained with distinct inner film clearances (left) and with distinct lubricant viscosities (right). Rotor speed of 200 krpm.

The current work also shows that the rotor SSV amplitudes decrease with an increase of the SFRB inner film length and/or the inner diameter, respectively, as the rotor becomes less flexible. This observation is consistent with the statement by Vistamehr [50], who performed nonlinear rotordynamic predictions for a TC rotor supported on a SFRB. For rotor speeds from 30 krpm to 240 krpm, the SSV amplitudes decrease by ~11% with an increase of the SFRB inner film length by ~15 %. Note that for the same rotor speed range, the current work shows the SSV amplitudes decrease by ~30% with an increase in the SFRB inner film length by ~30%. Moreover, Koutsovasilis et al. [31] quantify the SSV for a TC rotor supported on fully floating ring bearings and show that a flexible rotor with a small the inner diameter produces larger SSV amplitudes.

In the current analysis, the rotor synchronous motion amplitudes increase with an increase in the mass imbalance amount while the rotor subsynchronous motion amplitudes decrease, as shown in Fig. 54. Wang [51] shows the rotor synchronous motion amplitudes increase with an increase in the amount of mass imbalance, while the SSV amplitudes are suppressed, as shown in Fig. 57. Note that the rotor synchronous motion amplitudes do not exceed the bearings' clearances, otherwise the rotor failures due to the rubbing contact. In addition, the rotor onset speed of instability is delayed as the increased amplitudes of rotor synchronous motion restrain the oil film instability. Hence, an increase in the mass imbalance amount could improve the stability of a TC rotor-bearing system. In Fig. 58, San Andrés and Vistamehr [28] show that increasing the mass imbalance amount produces a rotor-bearing system response without SSV motions over a wide range of rotor speeds (~100 krpm to ~240 krpm).

(a) 1/2 x Imbalance

(b) 1 x Imbalance

(c) 2 x Imbalance
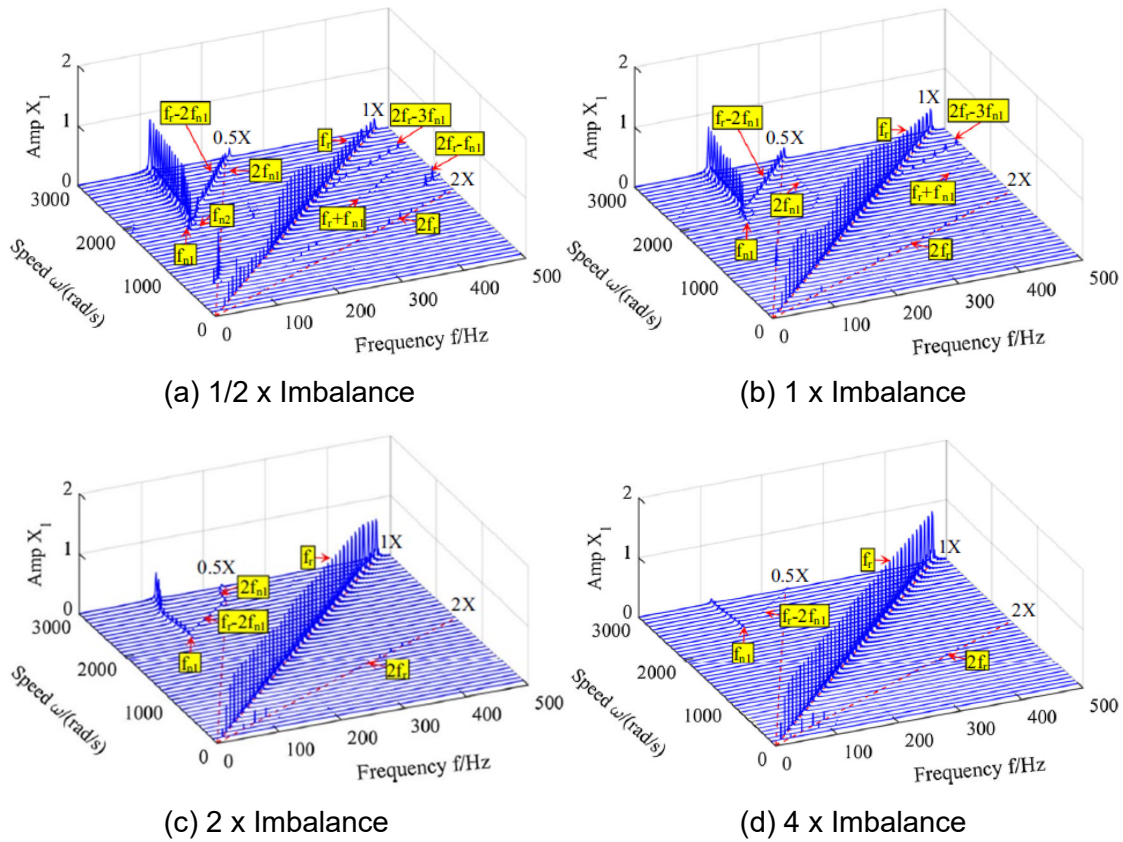
(d) 4 x Imbalance

Figure 57. Waterfall plots of nonlinear transient response predictions taken from Ref. [51]. Comparison of rotor responses obtained with distinct amounts of mass imbalance.

(a) 1 x Imbalance
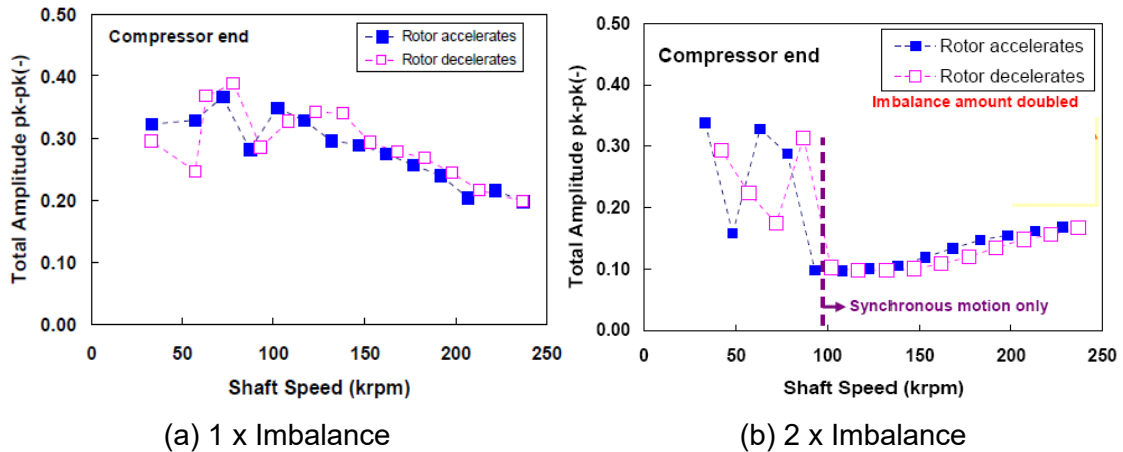
(b) 2 x Imbalance

Figure 58. Amplitude of total shaft motion versus shaft speed reproduced with permission of Ref. [28]. Location; compressor nose, vertical plane. Comparison of rotor responses obtained with nominal mass imbalance and with twice nominal. ($\varphi_{i=1,4}=0^o$).

107

San Andrés and Vistamehr [28] also show the total amplitude of shaft motion decreases with imbalances located at $\varphi_1=\varphi_3=0^o$ and $\varphi_2=\varphi_4=180^o$ (opposing coupled imbalance) and with imbalances located at $\varphi_1=\varphi_2=\varphi_4=0^o$ and $\varphi_3=180^o$ (turbine-back of-out-of-phase), as shown in Fig. 59. The predictions obtained from the current work show that the total shaft motion amplitudes for the TC-SFRB with imbalances located at $\varphi_1=\varphi_3=0^o$ and $\varphi_2=\varphi_4=180^o$ are ~26 % smaller than the total shaft motion amplitudes for the TC-SFRB with nominal magnitude imbalances located at all-in-phase angles ($\varphi_{i=1,4}=0^o$). The total shaft motion amplitudes for the TC-SFRB with imbalances located at $\varphi_1=\varphi_2=\varphi_4=0^o$ and $\varphi_3=180^o$ are ~15 % smaller than the total shaft motion amplitudes for the TC-SFRB with a nominal imbalance distribution ($\varphi_{i=1,4}=0^o$).

(a) $\varphi_1=\varphi_3=0^o$ and $\varphi_2=\varphi_4=180^o$ (b) $\varphi_1=\varphi_2=\varphi_4=0^o$ and $\varphi_3=180^o$
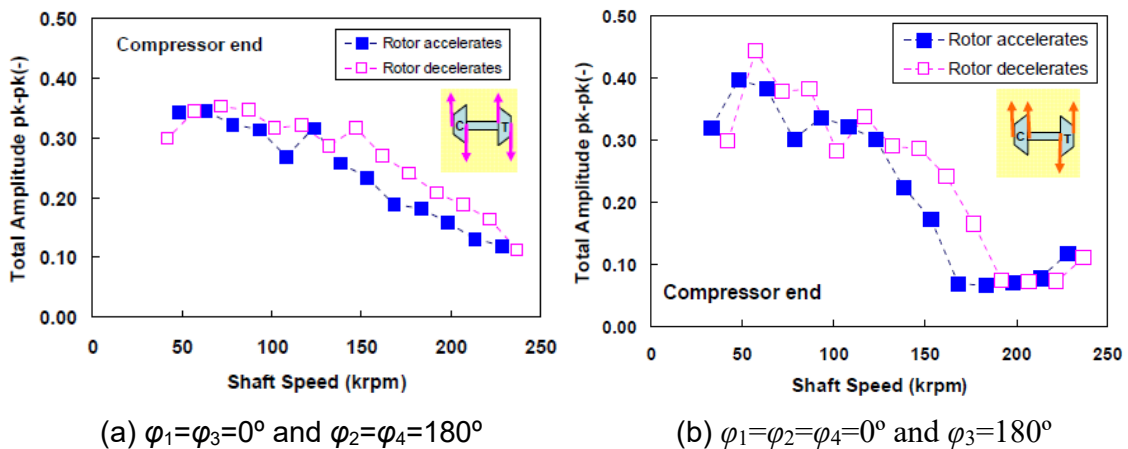
Figure 59. Amplitude of total shaft motion versus shaft speed reproduced with permission of Ref. [28]. Location; compressor nose, vertical plane. Comparison of rotor responses obtained with imbalances located at distinct phase angles; ($\varphi_1=\varphi_3=0^o$, $\varphi_2=\varphi_4=180^o$), ($\varphi_1=\varphi_2=\varphi_4=0^o$, $\varphi_3=180^o$).

In sum, for the rotordynamic stable performance of a TC rotor-bearing system (i.e. showing little to no SSV), a TC manufacturer may consider a TC-SFRB which operates with a ~84 % larger lubricant viscosity (μ =11.8 c-Poise > μ^* =6.4 c-Poise), and is constructed to have a ~20 % smaller inner film clearance (c_i =6 μm < c_i^* =7.5 μm), ~30 % longer bearing inner film length (L_i =5.6 mm > L_i^* =4.3 mm) and ~33 % thicker shaft diameter (D_i =8 mm > D_i^* =6 mm). However, considering an effective thermal management to ensure reliable TC operation, the aforementioned recommended TC rotor-bearing system may aggravate the performance of TC, as the TC-SFRB system demands ~54 % less lubricant flow and increases the viscous drag power loss by ~91 % and the heat transported in the film is ~15 % larger.

CHAPTER VI

CONCLUSIONS

This dissertation describes the integration of a finite length (semi) floating ring bearing (SFRB) model into a rotor and ring structural model for prediction of both the linear and nonlinear rotor responses for a TC and their characterization in terms of motion amplitudes and whirl frequencies.

The research investigates the effect of thermal energy transport on the performance of oil lubricated SFRBs for automotive TCs. The SFRB model considers a three-dimensional heat conduction equation that couples to a thermal energy transport network for the inner and outer radial films and the thrust bearings on each side of the ring. Thermal gradients affect the films' operating clearances and oil viscosity in each lubricated element, radial and axial.

In addition, rotordynamic force coefficients obtained from the SFRB analysis are coupled to a linear rotordynamics model that performs a linear stability analysis and produces damped natural frequencies and mode shapes. With estimated mass imbalances and their distributions the model calculates the TC rotor synchronous response. Obtained from the SFRB analysis, the SFRB operating clearances and effective lubricant viscosities for the inner and outer films are coupled to a rotordynamics model as the main input for predicting bearing nonlinear reaction forces; and thus then to conduct a nonlinear time transient response analysis.

Predictions where obtained for a particular TC and SFRB configuration with the following nominal operating parameters:

- Oil supply pressure and temperature: 3 bar and 120 ºC
- Lubricant type: SAE 10W30 ($\mu^* = 6.39$ c-Poise at 120 ºC)
- Bearing inner film clearance (c_i^*): 7.5 µm at 20 ºC, inner film length (L_i^*): 4.3 mm, inner film diameter (D_i^*): 6 mm
- Mass imbalance amounts and distribution: see Table 3, total 0.125 gram-mm, all masses-in-phase

The major conclusions drawn from this work are as follows:

Predictions of heat flows with thermohydrodynamic model for TC-SFRB system

1) For both the CB and the TB, the ring temperature varies greatly (> 20 ºC) along the entire rotor speed range (30 krpm to 240 krpm), as found from the difference between the maximum temperature and the average temperature, mainly due to the axial heat from the thrust bearing into the ring.

2) Over the entire shaft speed range, the inner and outer film temperatures and the ring ID and OD surface temperatures for the TB are higher than those for the CB since most heat is drawn from the *hot* turbine wheel side ($T_{S,turbine}$ =213 ºC).

3) For the CB and the TB, the flow rates through the inner and outer films of the TB are larger than those in the CB because of lower lubricant viscosities due to the higher film temperatures in the TB.

4) The heat from the shaft into the inner film, the heat from the thrust collar into the thrust film, and the heat conducted into the ring are larger on the TB side

111

than those on the CB side, as the overall films and the ring temperatures are also higher.
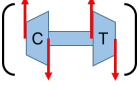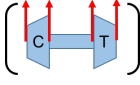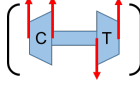
5) At a low shaft speed of 45 krpm, the heat flow from the shaft overwhelms the viscous drag power loss. However, as the shaft speed increases to 240 krpm, the contribution from the shear drag power to the total energy flow increases significantly from 3% to 63%. The thrust bearing produces 27%-39% of the total energy flow.

6) The lubricant carries away the majority of the heat flow, from 74% at a low shaft speed (45 krpm) to 81% at the highest shaft speed (240 krpm). The ring conducts a considerable portion of energy flows from the inner film into the outer film; 49% - 39% of the total energy flow as shaft speed increases.

7) A more conductive ring material or a longer outer film would conduct more heat into the ring and casing. Ultimately, however, the lubricant flow carries most of the thermal energy flow (> 70 %) from viscous drag power losses and the heat from the shaft.

Predictions of linear and nonlinear rotordynamic responses for TC-SFRB system

1) The elastic free-free rotor modes show large deflections at the compressor side, the lighter component.

2) The lowest two forward whirl modes (FWM) of the TC rotor show a negative damping ratio ($\zeta < 0$) and correspond to a rotor conical mode and a rotor cylindrical-bending mode. The corresponding ring (rigid body) natural modes are conical and cylindrical, respectively.

3) Over the entire shaft speed range (30 krpm to 240 krpm), the synchronous rotor response to imbalance shows peak amplitudes at the compressor end, since the compressor end is more flexible than the turbine end.

4) For rotor speeds of 30 krpm to 240 krpm, the rotor subsynchronous motion (SSV) amplitudes for a TC-SFRB with an inner film c_i =6 μm (=0.8 c_i*) are ~23 % smaller than the rotor SSV amplitudes for the TC-SFRB with a nominal inner film c_i* =7.5 μm.

5) The rotor SSV amplitudes for a TC-SFRB system supplied with a large lubricant viscosity (μ =11.8 c-Poise =1.8 μ*) are ~18% smaller than the rotor SSV amplitudes for the same system supplied with a lower (nominal) lubricant viscosity (μ* =6.4 c-Poise).

6) The rotor SSV amplitudes for a TC-SFRB with an inner length L_i =5.6 mm (= 1.3 L_i*) are ~30 % smaller than the rotor SSV amplitudes for a TC-SFRB with a nominal inner length L_i* =4.3 mm.

7) The rotor SSV amplitudes for a TC-SFRB with a shaft diameter D_i =8 mm (= 1.3 D_i*) are ~18 % smaller than the total shaft motion amplitudes for the TC-SFRB with a nominal shaft diameter D_i* =6 mm.

8) A TC-SFRB system supplied with a larger lubricant viscosity (μ =11.8 c-Poise), ~84 % than a nominal lubricant viscosity (μ* =6.4 c-Poise), and constructed to have bearings with a ~20 % smaller inner film clearance (c_i =6 μm < c_i* =7.5 μm), ~30 % longer bearing inner film length (L_i =5.6 mm > L_i* =4.3 mm), and ~33 % thicker shaft diameter (D_i =8 mm > D_i* =6 mm), demands ~54 % less

lubricant flow, ~91 % more viscous drag power loss, and ~15 % more heat in the film than the nominal TC-SFRB system.

9) The rotor SSV amplitudes of motion for a TC-SFRB with mass imbalances $\varphi_1=\varphi_3=0^\circ$ and $\varphi_2=\varphi_4=180^\circ$ (opposing couples) are ~26 % smaller than the rotor SSV amplitudes for a TC-SFRB with mass imbalances located at $\varphi_{i=1,4}=0^\circ$ (all-in-phase). Likewise, the rotor SSV amplitudes for a TC-SFRB with mass imbalances located at $\varphi_1=\varphi_2=\varphi_4=0^\circ$ and $\varphi_3=180^\circ$ (turbine-back of-out-of-phase) are ~15 % smaller than the rotor SSV amplitudes for a TC-SFRB with mass imbalances located at $\varphi_{i=1,4}=0^\circ$.

10) The rotor SSV amplitudes for a TC-SFRB with twice the amount of nominal mass imbalance (total 0.250 gram-mm) are ~37 % smaller than the rotor SSV amplitudes for a TC-SFRB with nominal mass imbalance (total 0.125 gram-mm), all-in-phase.

In conclusion, the rotor SSV amplitudes decrease when the SFRB is supplied with a lubricant with a large viscosity ($\mu= 1.8\ \mu^*$), and the bearings constructed to have a small inner film clearance ($c_i=0.8\ c_i^*$), a long inner film length ($L_i= 1.3\ L_i^*$), and a shaft with a thick diameter ($D_i= 1.3\ D_i^*$). However, changing the TC-SFRB parameters is neither practical nor realistic as the system demands time and resources. The recommended TC rotor-bearing system may aggravate the thermal efficiency of the TC performance as the system demands less lubricant flow and increases the viscous drag power loss and the heat

in the film. A TC supplied with a heavy lubricant can produce more NOx that could exceed acceptable emission standards for PVs [46].

The model and predictions may assist to the design of TC-SFRB systems with engineered thermal energy flow paths in order to improve TC efficiency and durability. The predictive rotordynamics model further enables an assessment of TC rotordynamic performance that otherwise would require experimentation.

REFERENCES

[1]   Watel, E., Pagot, A., Pacaud, P. and Schmitt, J.C., 2010, "Matching and Evaluating Methods for Euro 6 and Efficient Two-Stage Turbocharging Diesel Engine," SAE Technical Paper No. 2010-01-1229.

[2]   Kirwan, J.E., Shost, M., Roth, G. and Zizelman, J., 2010, "3-Cylinder Turbocharged Gasoline Direct Injection: A High Value Solution for Low CO_2 and NO_X emissions," SAE Int. J. Engines, **3**(1), pp.355-371.

[3]   Bonello, P., 2009, "Transient Modal Analysis of the Non-Linear Dynamics of a Turbocharger on Floating Ring Bearings," Proc. IMechE, Part J, **223**(1), pp. 79-93.

[4]   San Andrés, L., Jung, W., and Hong, S.K., 2021, "A Thermo-Hydrodynamic Model for Thermal Energy Flow Management in a (Semi) Floating Ring Bearing System for Automotive Turbochargers," ASME J. Eng. Gas Turbines Power, **143**(1), p. 011013.

[5]   Shaaban, S., 2004, "Experimental Investigation and Extended Simulation of Turbocharger Non-adiabatic Performance," Ph.D. thesis, Mechanical Power Engineering Department, Helwan University, Egypt.

[6]   Bohn, D., Moritz, N., and Wolff, M., 2003, "Conjugate Flow and Heat Transfer Investigation of a Turbo Charger—Part II: Experimental Results," ASME Paper No. GT2003-38449.

[7]   Cormerais, M., Hetet, J. F., Chesse, P., and Maiboom, A., 2006, "Heat Transfer Analysis in a Turbocharger Compressor: Modeling and Experiments," SAE Technical Paper No. 2006-01-0023.

[8]   Baines, N., Wygant, K. D., and Antonis, D., 2010, "The Analysis of Heat Transfer in Automotive Turbochargers," ASME J. Eng. Gas Turbines Power, **132**, p. 042301.

[9]   Romagnoli, A., and Martinez-Botas, R., 2012, "Heat Transfer Analysis in a Turbocharger Turbine: An Experimental and Computational Evaluation," Appl. Therm. Eng., **38**, pp. 58–77.

[10] Lamquin, T., and Gjika, K., 2009, "Power Losses on a Turbocharger Hydrodynamic Bearing Systems: Test and Prediction," ASME Paper No. GT2009-59599.

[11] Deligant, M., Povedin, P., and Descombes, G., 2011, "CFD Model for Turbocharger Journal Bearing Performances," Appl. Therm. Eng., **31**, pp. 811–819.

[12] San Andrés, L., and Kerth, J., 2004, "Thermal Effects on the Performance of Floating Ring Bearing for Turbocharger," Proc. IMechE, Part J, **218**(5), pp. 437–450.

[13] San Andrés, L., Barbarie, V., Bhattacharya, A., and Gjika, K., 2012, "On the Effect of Thermal Energy Transport to the Performance of (Semi) Floating Ring Bearing Systems for Automotive Turbocharger," ASME J. Eng. Gas Turbines Power, **134**(10), p.102507.

[14] Bohn, D., Heuer, T., and Kusterer, K., 2005, "Conjugate Flow and Heat Transfer Investigation of a Turbo Charger," ASME J. Eng. Gas Turbines Power, **127**(3), pp. 663–669.

[15] Heuer, T., Engels, B., Klein, A., and Heger, H., 2006, "Numerical and Experimental Analysis of the Thermo-Mechanical Load on Turbine Wheels of Turbochargers," ASME Paper No. GT2006-90526.

[16] Liang, F., Li, Y., Zhou, M., Xu, Q. and Du, F., 2017, "Integrated Three-Dimensional Thermohydrodynamic Analysis of Turbocharger Rotor and Semifloating Ring Bearings," ASME J. Eng. Gas Turbines Power, **139**(8), p.082501.

[17] San Andrés, L., Yu, F. and Gjika, K., 2018, "On the Influence of Lubricant Supply Conditions and Bearing Configuration to the Performance of (Semi) Floating Ring Bearing Systems for Turbochargers," ASME J. Eng. Gas Turbines Power, **140**(3), p.032503.

[18] Nitzschke, S., Woschke, E. and Daniel, C., 2018, "Application of Regularised Cavitation Algorithm for Transient Analysis of Rotors Supported in Floating Ring Bearings," IFToMM, **63**, pp. 371-387, Springer, Cham.

[19] Sandoval, O.R., Machado, L.H., Caetano, B., Lara, I.F. and Molina, R., 2018, "Influence of Temperature and Injection Pressure of Lubrication in the Vibration of an Automotive Turbocharger," IFToMM, **63**, pp. 388-397, Springer, Cham.

[20] Zhang, C., Men, R., Wang, Y., He, H. and Chen, W., 2019, "Experimental and Numerical Investigation on Thermodynamic Performance of Full-Floating Ring Bearings with Circumferential Oil Groove," Proc. IMechE, Part J, p.1350650119826421.

[21] Yu, T. H., and Sadeghi, F., 2002, "Thermal Effects in Thrust Washer Lubrication," ASME J. Tribol., **124**(1), pp. 166–177.

[22] Lee, I.B., Hong, S.K. and Choi, B.L., 2018, "Investigation of the Axial Thrust Load Using Numerical and Experimental Techniques during Turbocharger Operation," Proc. IMechE, Part D, **232(6)**, pp.755-765.

[23] Peixoto, T.F., Nordmann, R. and Cavalca, K.L., 2021, "Dynamic Analysis of Turbochargers with Thermo-Hydrodynamic Lubrication Bearings," J. Sound and Vib., **505**, p.116140

[24] Nguyen-Schäfer, H., 2012, "Rotordynamics of Automotive Turbochargers," Springer, Cham.

[25] Holt, C., San Andrés, L., Sahay, S., Tang, P., LaRue, G., and Gjika, K., 2005, "Test Response and Nonlinear Analysis of a Turbocharger Supported on Floating Ring Bearings," ASME J. Vib. Acoust., **127**, pp. 107-115.

[26] San Andrés, L., Rivadeneira, J. C., Gjika, K., Groves, C., and G. LaRue, 2007, "A Virtual Tool for Prediction of Turbocharger Nonlinear Dynamic Response: Validation Against Test Data," ASME J. Eng. Gas Turbines Power, 129, pp. 1035–1046.

[27] San Andrés, L., Maruyama, A., Gjika, K., and Xia, S., 2010, "Turbocharger Nonlinear Response with Engine-Induced Excitations: Predictions and Test Data," ASME J. Eng. Gas Turbines Power, **132**, p. 032502.

[28] San Andrés, L., and Vistamehr, A., 2010, "Nonlinear Rotordynamics of Vehicle Turbochargers: Parameters Affecting Sub Harmonic Whirl Frequencies and Their Jump," Proc. of the 8th IFToMM Int. Conf., pp. 12-15.

[29] Gjika, K., and Groves, C., 2006, "Nonlinear Dynamic Behavior of Rotor-Bearing Systems Involving Two Hydrodynamic Oil Films in Series: Prediction and Test Application to High-Speed Turbochargers," Proc. ASME ESDA 95792, pp. 393-399.

[30] Schweizer, B., and Sievert, M., 2009, "Nonlinear Oscillations of Automotive Turbocharger Turbines," J. Sound and Vib., **321**(3-5), pp.955-975.

[31] Koutsovasilis, P., Driot, N., Lu, D. and Schweizer, B., 2015, "Quantification of Sub-Synchronous Vibrations for Turbocharger Rotors with Full-Floating Ring Bearings," Arch. Appl. Mech., **85(4)**, pp.481-502.

[32] Liang, F., Xu, Q. and Zhou, M., 2015, "Predicting the Frequency of the Rotor Whirl Excited by Semi-Floating Ring Bearing," ASME 2015 International Design Engineering Technical Conferences and Computers and Information in Engineering Conference.

[33] Cao, J., Dousti, S., Allaire, P. and Dimond, T., 2017, "Nonlinear Transient Modeling and Design of Turbocharger Rotor/Semi-Floating Bush Bearing System," Lubricants, **5**(2), p.16.

[34] R. Vengala, P., Chandrasekaran, L., Selvaraj, P.K. and Arthanarisamy, S.D., 2019, "Investigation of Sub Synchronous Vibration of Very High Speed Turbocharger Semi-Floating Bearing System: Prediction vs Test," ASME Int. Mech. Eng. Congress and Expo., **59414**, p. V004T05A032.

[35] Koutsovasilis, P., 2019, "Automotive Turbocharger Rotordynamics: Interaction of Thrust and Radial Bearings in Shaft Motion Simulation," J. Sound and Vib., **455**, pp. 413-429.

[36] Kays, W.M., and Crawford, M.E., 1980, *Convective Heat and Mass Transfer*, 2nd ed., McGraw-Hill, inc., NY, Chap. 8.

[37] Lee, P., Garimella, S.V., and Liu D., 2005, "Investigation of Heat Transfer in Rectangular Microchannels," Int. J. Heat and Mass Transfer, **48**, pp. 1688-1704.

[38] Tanaka, M., and Hori, Y., 1972, "Stability Characteristics of Floating Bush Bearings," ASME J. Lub. Tech., **94**, pp. 248-259.

[39] Cross, M. M., 1965, "Rheology of Non-Newtonian Fluids: a New Flow Equation for Pseudo Plastic System," J. Colloid Sci., **20**, pp. 417-437.

[40] San Andrés, L., Cable, T.A., Wygant, K. and Morton, A., 2015, "On the Predicted Performance of Oil Lubricated Thrust Collars in Integrally Geared Compressors," ASME J. Eng. Gas Turbines Power, **137**(5), p.052502.

[41] Chatzisavvas, I., Nowald, G., Schweizer, B. and Koutsovasilis, P., 2017, "Experimental and Numerical Investigations of Turbocharger Rotors on Full-Floating Ring Bearings with Circumferential Oil-Groove," ASME Paper No. GT2017-64628.

[42] Murphy, B.T., 2019. XLRotor Version 5.60. *Austin, Texas. http://www. xlrotor. com.*

[43] Shampine, L.F., 1982, "Implementation of Rosenbrock Methods," ACM TOMS, **8**(2), pp.93-113.

[44] Lee, I.B., and Kim, J.B., 2016, KeyYang Precision Co., Ltd., Gimcheon, South Korea, 740180, personal communication.

[45] IRD Balancing, 2001, "Balance Quality Requirements of Rigid Rotors: The Practical Application of ISO 1940/1," www.irdbalancing.com/irdbalancing/techpapers/TechPaper-1BalQuality.Regmts.pdf.

[46] Singh, S.K., Singh, S. and Sehgal, A.K., 2016 "Impact of Low Viscosity Engine Oil on Performance, Fuel Economy and Emissions of Light Duty Diesel Engine," SAE Technical Paper No. 2016-01-2316.

[47] Smolík, L., Hajžman, M. and Byrtus, M., 2017, "Investigation of Bearing Clearance Effects in Dynamics of Turbochargers," Int. J. Mech. Sci., **127**, pp.62-72.

[48] Gjika, K., San Andrés, L. and LaRue, G.D., 2010, "Nonlinear Dynamic Behavior of Turbocharger Rotor-Bearing Systems with Hydrodynamic Oil Film and Squeeze Film Damper in Series: Prediction and Experiment," ASME J. Comput. Nonlinear Dynam., **5**(4). p.041006.

[49] Mutra, R.R., 2019, "Identification of Rotor Bearing Parameters Using Vibration Response Data in a Turbocharger Rotor," JCARME, **9**(1), pp.145-156.

[50] Vistamehr, A., 2009, "Analysis of Automotive Turbocharger Nonlinear Vibrations Including Bifurcations", Master Thesis, Texas A&M University, College Station, TX.

[51] Wang, L., Wang, A., Jin, M., Huang, Q. and Yin, Y., 2019, "Nonlinear Effects of Induced Unbalance in the Rod Fastening Rotor-Bearing System Considering Nonlinear Contact," Arch. Appl. Mech., **90**, pp.917-943.

[52] San Andrés, L., 2010, Modern Lubrication Theory, "Static Load Performance of Plain Journal Bearings," Notes 4, Texas A&M University Digital Libraries.

APPENDIX A

OPERATION OF COMPUTER PROGRAM

This section outlines the integration of both radial bearings (turbine and compressor sides) and the thrust bearings to produce a complete thermal analysis predictive tool. The tool is coupled to a rotordynamic model for an automotive TC rotor supported on a SFRB.

Figure A1 shows a flow chart for the operation of the computer program to calculate the SFRB performance (temperature and the pressure fields in fluid films, viscous drag power losses, and force coefficients) and the linear and the nonlinear rotor model response (eigenvalues analysis, synchronous and subsynchronous motions).

The SFRB geometry (diameter, length, clearance, material property, etc.) and operating conditions (oil supply pressure and temperature, lubricant property, rotor speed, static load) are the input parameters. The output parameters contain the operating clearances and the lubricant viscosity for the inner and the outer films, temperature and the pressure fields in fluid films, viscous drag power losses, and force coefficients.

In addition, the rotordynamic force coefficients obtained from the SFRB analysis are coupled to a linear rotordynamics model to perform a linear stability analysis and obtain the damped natural frequencies and mode shapes of the system. Estimated mass imbalances and their distribution are used to calculate the TC rotor synchronous response.

SFRB operating clearance and lubricant viscosity for the inner and outer films are the main input for predicting bearing forces to conduct a nonlinear time transient response

analysis which could yield rotor responses with a rich content in subsynchronous frequencies and amplitudes for specific operating conditions.
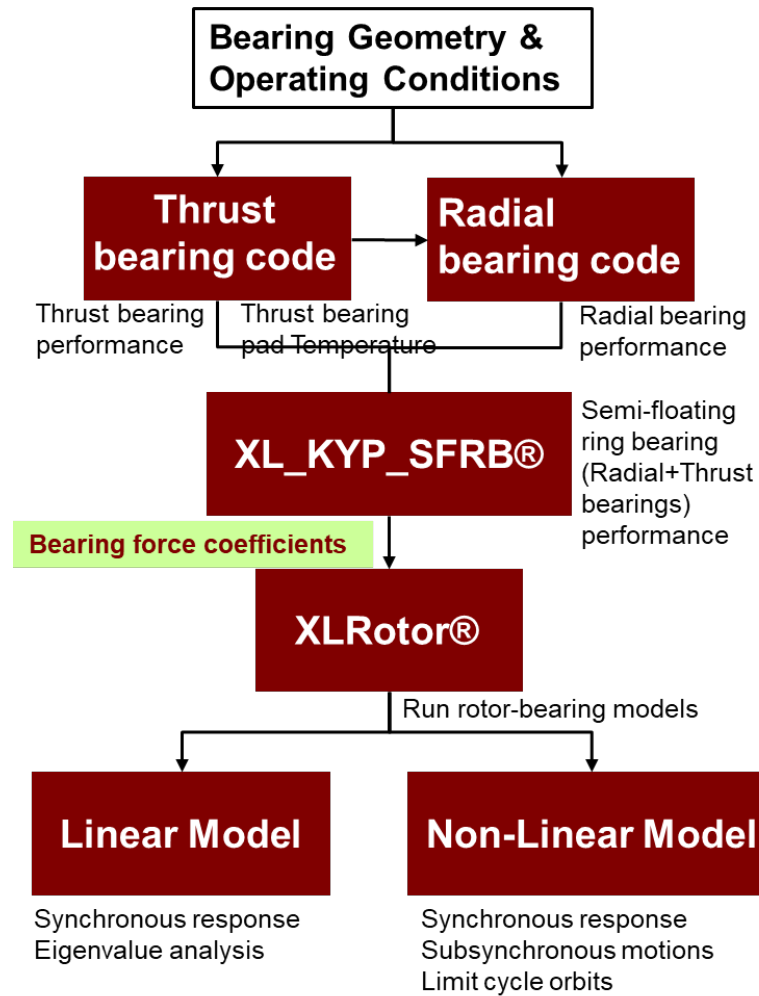

Figure A1. Flow chart for operation of computer program to calculate SFRB performance, linear and nonlinear rotor model response.

APPENDIX B

INITIAL CONDITIONS FOR TRANSIENT ANALYSIS RESPONSE CASES[5]

The equations of motion (EOMs) for a MDOF rotor system are (in general) [28]:

$$\mathbf{M}\ddot{\mathbf{X}} + \left[\mathbf{C} + \mathbf{G}\Omega\right]\dot{\mathbf{X}} + \mathbf{K}\mathbf{X} = \mathbf{F_{stat}} + \mathbf{F_{dyn}}_{(t)} - \mathbf{F_{B}}_{\left(\mathbf{X},\dot{\mathbf{X}},\Omega,t\right)} \tag{B1}$$

where $\mathbf{M, G, K, C}$ are global matrices of rotor inertias, gyroscopic effects, and the structure stiffness and damping coefficients. Ω is shaft speed, $\mathbf{F_{stat}}$ and $\mathbf{F_{dyn}}$ denote the vectors of static and dynamic loads acting on the rotor, for example. $\mathbf{F_B}$ represents the vector of nonlinear reaction forces arising from the lubricated bearings, for example.

Given $\mathbf{F_{stat}}$ and $\mathbf{F_{dyn}}$, a numerical procedure discretizes the equations above in terms of a system state-space vector $\left[\mathbf{X}, \dot{\mathbf{X}}\right]_{(t)}$ and solves them at discrete instants of time. The rotordynamics model [42] offers a number of choices for the numerical integration of Eq. (B1), for example Runge-Kutta, Rosenbrock, Average-Acceleration, etc. The proper selection of the numerical method (*solver*) and the time step for numerical integration are crucial to obtain accurate results.

Figure B1 shows a structural model of a simple rotor-bearing system for an example. The finite element model consists of 20 elements for the steel rotor and 2 elements for the journal bearings. For simplicity the compressor wheel and the turbine wheel are modeled with lumped mass and mass moment of inertia (polar and transverse). The inner film is a

---

[5] Portion reprinted from San Andrés, L. and Jung, W., 2020, "Analysis to Produce Physically Found Initial Conditions and Integration into a Model for Numerical Solution of the Transient Response of a Nonlinear Rotor-Bearing System", PhD Preliminary Exam Technical Report.

spring-like structure connecting the rotor to the ring, and a spring-like structure connecting

the ring to ground represents the outer film. Table B1 lists the geometry of the simple

rotor-bearing system and the lubricant physical properties.

Table B1. Geometry of a simple rotor-bearing system and lubricant physical properties.

RBS geometry	
Shaft OD, D_s	11.5 mm
Ring ID, D_{Ri}	11.534 mm
Ring OD, D_{Ro}	17.8 mm
Casing ID, D_c	17.883 mm
Inner film axial length, L_i	8.02 mm
Outer film axial length, L_o	10.6 mm
Inner film radial clearance, c_i	17 µm (at 20 ºC)
Outer film radial clearaance, c_o	41.5 µm (at 20 ºC)
Lubricant SAE 10W30	
Density, ρ	875 kg/m^3
Specific Heat, C_p	1,901 J/kg
Conductivity, κ	0.12 W/m ºC
Viscosity at T_{sup}, μ	6.39 c-Poise
Flash point temperature, T_{flash}	230 ºC
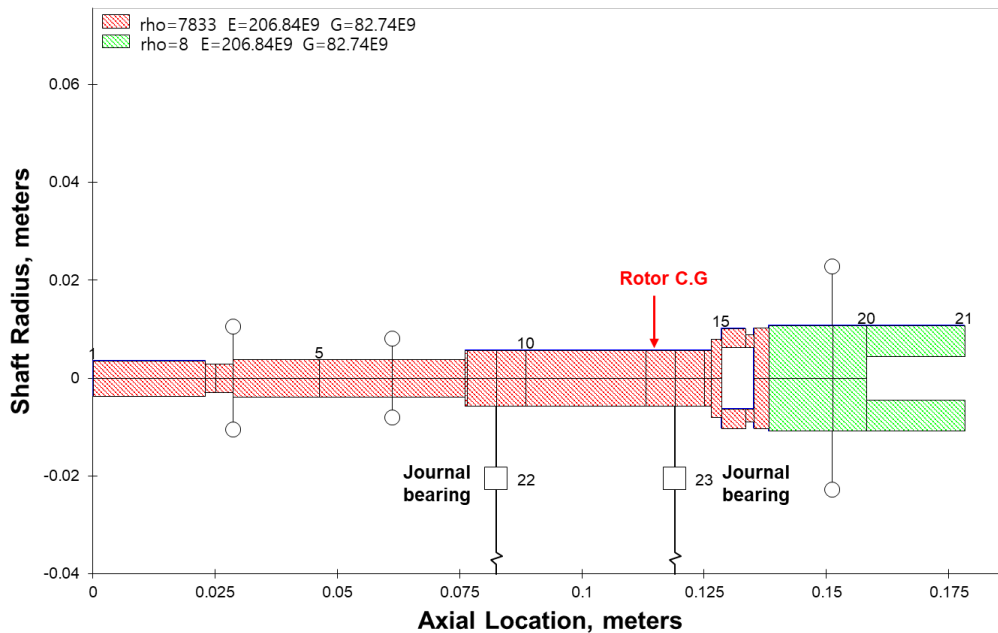
Figure B1. Elastic structure model of simple rotor-bearing system for example.

The rotor static sag line, $\mathbf{X_{RS}}$, is obtained from a short length journal bearing model. The total static load on the rotor is 6.04 N (total rotor mass = 616 g) and the location of the rotor center of mass is 114 mm from the compressor end. Note the rotor total length is 178 mm. Thus, the static loads on each bearings are 0.78 N for the CB and 5.25 N for the TB, respectively. Note that $\mathbf{X_{RS}}$ is little to null for the rotor and the ring at each bearing locations due to the *rigid* bearing supports.

The nonlinear bearing static displacement, $\mathbf{X_{BS}}$, is obtained from the journal and ring equilibrium eccentricities (e) for an applied load (W) given and the bearing geometry such as clearance (c), length (L), diameter (D), and lubricant viscosity (μ) and operating speed (Ω). Each bearing reaction force (F_B) balances a fraction of the applied static load, $F_B = a_i W$. Note that $a_{CB} = 0.13$ and $a_{TB} = 0.87$, respectively. For short length journal bearings, a modified Sommerfeld number (σ) is [52]

$$\frac{\mu \Omega L R}{4 F_B} \left(\frac{L}{c}\right)^2 = \sigma = \frac{(1-\varepsilon^2)^2}{\varepsilon \sqrt{\{16\varepsilon^2 + \pi^2(1-\varepsilon^2)\}}} \tag{B2}$$

where ε is the relative eccentricity ratio to the ring. Then the journal eccentricity relative to the ring, ε_j, is calculated using a bisection method with given σ iteratively and converges quickly ($\ll$ 100 times of iterations).

$$f(\varepsilon_j, \sigma) = \frac{(1-\varepsilon_j^2)^2}{\varepsilon_j \sqrt{\{16\varepsilon_j^2 + \pi^2(1-\varepsilon_j^2)\}}} - \sigma = 0 \tag{B3}$$

On the other hand, the ring eccentricity relative to the casing, ε_r, is obtained with a simple linear connection considering a pin stiffness (K_{PIN}) as the ring does not rotate ($\Omega_R = 0$). Note that K_{PIN} is assumed to the ring speed ratio (RSR) = 0.01.

The equilibrium attitude angles for the journal (φ_j) and the ring (φ_r) between the static

load direction and the eccentricity vector are

$$\varphi_j = \tan^{-1}\left[\frac{\pi(1-\varepsilon_j^2)^{\frac{1}{2}}}{4\varepsilon_j}\right] \tag{B4.a}$$

$$\varphi_r = \tan^{-1}\left[\frac{\pi(1-\varepsilon_r^2)^{\frac{1}{2}}}{4\varepsilon_r}\right] \tag{B4.b}$$

Now, the x and y components of the journal eccentricity relative to the casing (e_x, e_y)

are evaluated from the vector sum of the journal and the ring eccentricities.

$$e_x = e_j \sin(\varphi_j) + e_r \sin(\varphi_r) \tag{B5.a}$$

$$e_y = -e_j \cos(\varphi_j) - e_r \cos(\varphi_r) \tag{B5.b}$$

where e_j and e_r are the dimensional relative journal and ring eccentricities, respectively;

$e_j = \varepsilon_j c_i$, $e_r = \varepsilon_r c_o$.

$\mathbf{X_{BS}}$ is linearized along the axial direction to add vectorially with $\mathbf{X_{RS}}$ to produce the

rotor static displacement, $\mathbf{X_S}$, i.e. $\mathbf{X_S}=\mathbf{X_{RS}}+\mathbf{X_{BS}}$. Note that the vector of generalized

displacements is $\mathbf{X}=\begin{bmatrix}\mathbf{x_1}\\\mathbf{x_2}\\\mathbf{x_n}\end{bmatrix}$, $\mathbf{x}=\begin{bmatrix}x & y & \theta_x & \theta_y\end{bmatrix}^T$, which including both physical

translations (x,y) and rotations (θ_x, θ_y) at each station.

Figure B2 shows the rotor static displacement ($\mathbf{X_S}$) for TC rotor-bearing system at

rotor speed of 100 krpm. The result shows that the rotor static displacement at the TB is

larger than the one at the CB, as the rotor center of mass is close to the TB. The result also

shows that the rotor elastic deflection is relatively not important as the static load due to the rotor weight is small in this application. The static displacement vector is used as the initial condition (IC) for subsequent transient analysis response cases, i.e. set

$$\left[\mathbf{X}, \dot{\mathbf{X}}\right]_{(t=0)} = \left[\mathbf{X}_o, \dot{\mathbf{X}}_o\right] \leftarrow \left[\mathbf{X}_S, \mathbf{0}\right].$$
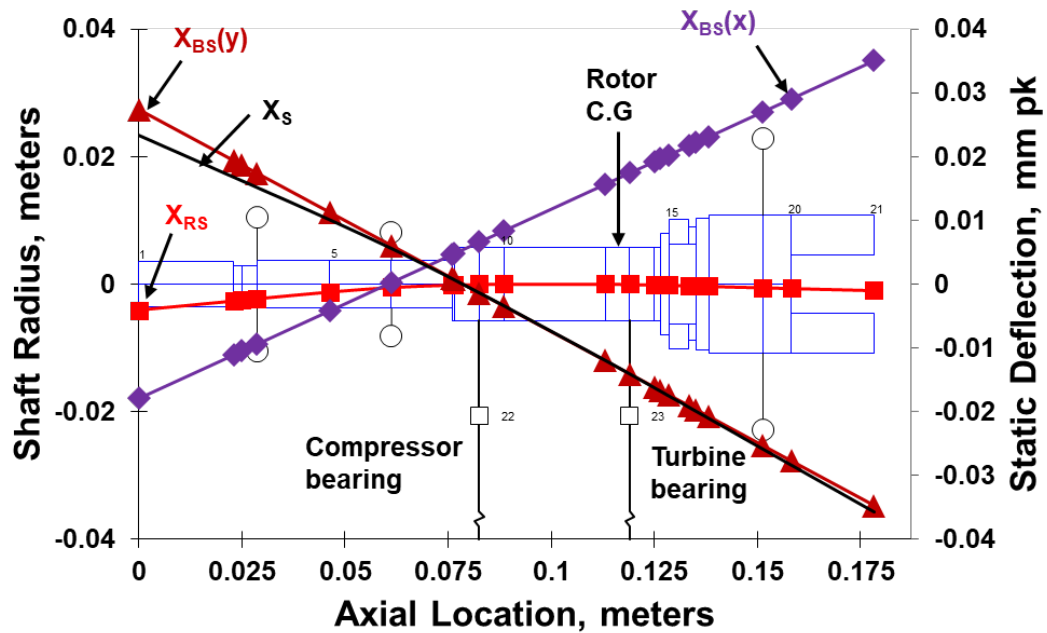

Figure B2. Rotor static deflection ($X_S= X_{RS}+X_{BS}$) for TC rotor-bearing system to setup initial condition of nonlinear transient prediction as the rotor static equilibrium position. Example at rotor speed = 100 krpm.